~ rossum /tex/thesis

Hadron Production in Two-Photon Collisions at LEP

Productie van hadronen in twee-fotonbotsingen bij LEP

(met een samenvatting in het Nederlands)

Proefschrift

TER VERKRIJGING VAN DE GRAAD VAN DOCTOR AAN
DE UNIVERSITEIT UTRECHT OP GEZAG VAN DE RECTOR
MAGNIFICUS, PROF. DR. H.O. VOORMA, INGEVOLGE
HET BESLUIT VAN HET COLLEGE VAN DECANEN
IN HET OPENBAAR TE VERDEDIGEN OP VRIJDAG
6 MAART 1998 DES MORGENS TE 10.30 UUR

DOOR

Wilhelmus Lambertus van Rossum

GEBOREN OP 8 NOVEMBER 1968 TE HOUTEN

promotores: Prof. Dr. Ir F.C. Erné
Prof. Dr. A. Buijs
Faculteit der Natuur- en Sterrenkunde, Universiteit Utrecht
copromotor: Dr. G.J. Bobbink
Nationaal Instituut voor Kernfysica en Hoge-Energiefysica

The work described in this thesis is part of the research programme of "het Nationaal Instituut voor Kernfysica en Hoge-Energiefysica (NIKHEF)" Amsterdam, The Netherlands. The author was financially supported by the Utrecht University and the Netherlands organisation "Fundamenteel Onderzoek der Materie (FOM)", which is part of the "Nederlandse Organisatie voor Wetenschappelijk Onderzoek (NWO)".

CIP-GEGEVENS KONINKLIJKE BIBLIOTHEEK, DEN HAAG

van Rossum, Wilhelmus Lambertus

HADRON PRODUCTION IN TWO-PHOTON COLLISIONS AT LEP
Wilhelmus Lambertus van Rossum - Utrecht: Universiteit Utrecht,
Faculteit der Natuur- en Sterrenkunde
Thesis University Utrecht - with summary in Dutch
ISBN xx-xxx-xxxx-x

Contents

Introduction **1**

1 Theoretical and experimental overview **3**
1.1 Kinematics . . . 3
1.2 General expression for $\sigma(e^+e^- \to e^+e^- X)$ . . . 5
1.3 Equivalent Photon Approximation . . . 7
1.4 The hadronic two-photon cross section . . . 9
1.4.1 Vector-meson Dominance Model . . . 10
1.4.2 Direct cross section . . . 14
1.4.3 Anomalous cross sections . . . 14
1.5 Monte Carlo generators . . . 15
1.5.1 PHOJET . . . 15
1.5.2 PYTHIA . . . 17
1.6 Summary of previous experimental results . . . 18

2 The L3 Detector **23**
2.1 Introduction . . . 23
2.2 The L3 detector . . . 24
2.2.1 Silicon microvertex detector . . . 24
2.2.2 Central tracking chamber . . . 25
2.2.3 Electro-magnetic calorimeter . . . 26
2.2.4 Hadron calorimeter . . . 27
2.2.5 Active lead ring . . . 29
2.2.6 Luminosity monitor . . . 29
2.2.7 Muon chambers . . . 29
2.3 Triggers . . . 31
2.3.1 Level 1 trigger . . . 31
2.3.2 Level 2 and 3 triggers . . . 33
2.4 Event reconstruction . . . 33
2.4.1 Primitive clusters . . . 34
2.4.2 Smallest resolvable clusters . . . 34
2.4.3 Visible mass . . . 34
2.5 Event simulation . . . 36
2.5.1 Detector noise . . . 37

3 Untagged data **39**
3.1 Data taken around the Z pole . . . 39
3.1.1 Data selection . . . 39
3.1.2 Data integrity . . . 48
3.2 Data taken around 133 GeV . . . 49
3.2.1 Data selection . . . 49
3.2.2 Data integrity . . . 52
3.3 Cross section calculation . . . 52
3.4 Cross section fits . . . 56
3.5 Summary and conclusions . . . 59

4 Tagged data **61**
4.1 Selection of the tags . . . 61
4.2 Selection of the hadronic events . . . 63
4.3 Data integrity . . . 64
4.4 Results . . . 65
4.4.1 Mass dependence . . . 67
4.4.2 Q^2 dependence . . . 67
4.5 Summary and conclusions . . . 70

A Unfolding **73**
A.1 Introduction . . . 73
A.2 Unfolding based on Singular Value Decomposition . . . 75
A.3 Unfolding based on Bayes' Theorem . . . 78
A.4 Checking the methods . . . 81
A.5 Comparison of the two procedures . . . 82
A.6 Conclusions . . . 85

B Modifications of the PYTHIA generator **89**
B.1 Luminosity function . . . 89
B.2 Q^2 dependence . . . 90

References **93**

Summary **97**

Samenvatting **99**

Curriculum Vitae **101**

Dankwoord **103**

Introduction

In the 19th century, light waves were found to be a solution of the Maxwell equations. Within this theory, the waves move with the speed of light and two waves pass each other unhinderedly, as Huygens already predicted in the 18th century.

At the beginning of the 20th century, the idea evolved that light should be described by light particles instead of waves. This is nicely described by D. Griffiths [1]:

> In 1900, Planck attempted to explain the blackbody spectrum for the electromagnetic radiation emitted by a hot object. Statistical mechanics led to the "Ultraviolet catastrophe" when applied to electromagnetic fields, predicting that the total power radiated should be infinite. Planck found that he could fit the experimental curve if he assumed that electromagnetic radiation is quantised, coming in packages of energy
>
> $$E = h\nu,$$
>
> with ν the frequency of the radiation and h a constant fitted to the data. Planck assumed that the quantisation was due to a peculiarity in the emission process.
>
> In 1905 Einstein argued that the quantisation was a feature of the field itself, and not the emission process. Einstein adapted Planck's idea to explain the photo-electric effect:
>
> $$E \leq h\nu - w.$$
>
> Here, w is the work function of the material. The electron may lose energy before reaching the surface, hence the $\leq$ sign. This means that the maximum energy for an electron is independent of the intensity of the light (the number of emitted electrons does increase with increasing intensity) but depends on the frequency of the light. In 1916 Millikan completed his study on the photoelectric effect and reported that "Einstein's photoelectric equation ... appears in every case to predict exactly the observed results... Yet the semicorpuscular theory by which Einstein arrived at this equation seems at present wholly untenable".

Not until 1923 was the idea of a light quantum accepted. In 1923 Compton found that the light scattered from a particle at rest is shifted in wavelength:

$$\lambda = \lambda' + \frac{h}{mc}(1 - \cos\theta),$$

with λ the incident wavelength, λ' the scattered wavelength, θ the scattering angle of the light and m the mass of the scattered particle. One can obtain this equation by assuming that the light quantum is a massless particle. In 1926 the chemist Lewis suggested to call this quantum a photon.

The successor of Maxwell's theory is called Quantum Electro Dynamics (QED). In this theory the photon is the mediator of the electromagnetic field and is described as the particle found by Compton.

In QED two photons can scatter from each other, in contrast to the classical electrodynamics were two waves would pass each other unhinderedly. In a two-photon collision with small-momentum transfer the main contribution to the total cross section comes from the coupling to vector mesons. From the decay of vector mesons it is evident that the photon couples to these mesons. Both photons couple to a vector meson and these two mesons interact. When the momentum transfer of the two photons is increased, perturbatively-calculable processes (with the help of QED for the lowest-order Feynman diagrams and Quantum Chromo-Dynamics for higher-order diagrams) become more important. This means that in two-photon physics both the soft processes from vector-meson collisions and hard processes from the perturbative-calculable diagrams can be investigated.

The total hadronic two-photon cross section is the subject of this thesis. It has been measured as a function of the mass of the two-photon system and as a function of the virtuality of the two photons. In the following the outline of this thesis is given.

In chapter 1 the theory of two-photon physics is discussed together with the equations needed to calculate the hadronic cross sections. Two different Monte-Carlo generators are discussed and previous results are summarised.

The L3 detector is described in chapter 2, together with the triggers and the reconstruction of the events.

In chapter 3 the untagged data and total cross sections are presented for data obtained around the Z pole (91 GeV) and at energies around 133 GeV. First the selection criteria are discussed. Then the data integrity is tested and the data is unfolded (relating the visible mass distribution to the true mass distribution). The results are shown together with the systematical errors. Finally comparisons are made in order to check the theoretical predictions.

In chapter 4 the tagged data taken around the Z pole is discussed. Again the selection criteria are explained first before the results are given for the cross section as a function of the virtual masses of the photons and as a function of the mass of the two-photon system. Different models are fitted to obtain the best description of the cross section as a function of the virtuality of the photon.

The first appendix explains the problems involved with the unfolding of the data. In the second appendix the modifications made to the PYTHIA generator are given.

1

Theoretical and experimental overview

In this chapter the theoretical equations needed in this thesis are given. Two different Monte-Carlo generators (PYTHIA and PHOJET) are discussed and some previous results are summarised at the end of this chapter.

1.1 Kinematics

Two-photon scattering at LEP can be observed in the reaction:

$$e^+e^- \to e^+e^- X,$$

in which the two incoming leptons both emit a virtual photon. In figure 1.1 a schematic view of this process is shown. The incoming leptons have momenta p_1 and p_2, while the outgoing leptons have momenta p_1' and p_2'. The final state produced by the two colliding photons is indicated by X (in this thesis only the hadronic final states are investigated).

The kinematics of the colliding photons is completely determined by the four-momenta of the incoming and outgoing electron and positron. For unpolarised beams with an energy E, five variables are needed to determine the two-photon system:

- The energy of the scattered leptons: E_1', E_2'.
- The scattering angles w.r.t. the direction of the incoming leptons: θ_1, θ_2.
- The angle between the two lepton scattering planes: ϕ.

The squared mass of each of the two photons is ($i = 1, 2$):

$$q_i^2 = -Q_i^2 = (p_i - p_i')^2 = 2m_e^2 - 2EE_i'\left(1 - \sqrt{1-(m_e/E)^2}\sqrt{1-(m_e/E_i')^2}\cos\theta_i\right),$$

and the mass, $W_{\gamma\gamma}$ of the total two-photon system is given by:

$$W_{\gamma\gamma}^2 = (q_1 + q_2)^2.$$

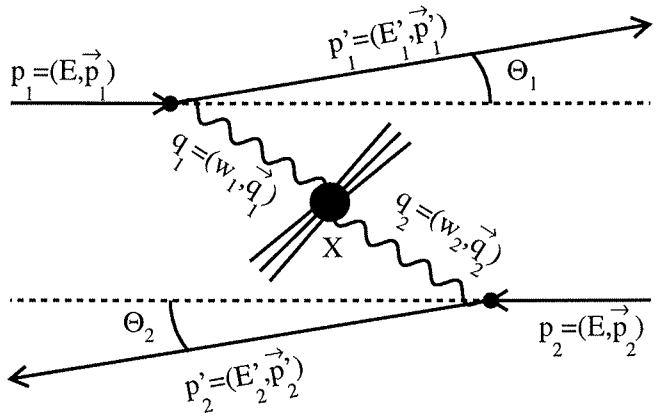

Figure 1.1: *Schematic view and kinematics of the process* $e^+e^- \to e^+e^-X$. *The final state X is produced by the two-photon collision in the centre of the figure.*

The fraction of the energy of the incoming particle which is carried by the photon is given by x_i:

$$x_i = Q_i^2/2q_1 \cdot q_2. \tag{1.1}$$

The scattering angles of the final state electron and positron are distributed according to a bremsstrahlungs spectrum. So in general they stay close to the beam and remain inside the beam pipe. The transverse momenta, momenta perpendicular to the direction of the beam particles, of these scattered particles remain small and the hadronic final state therefore has a small transverse momentum as well. In the longitudinal direction (along the direction of the beam particles) the momentum difference between the two photons will, in general, be large. Therefore the hadronic particles are boosted in the longitudinal direction. Owing to this boost these particles remain closer to the beam pipe than in the absence of this boost and are mainly detected in the forward calorimeters.

If the scattered electron and positron escape down the beam pipe, the mass of the final state X can be measured by detecting the particles produced in the hadronic final state. In this case no information can be obtained about the other variables. If one scattered lepton is detected, i.e. the angle of the scattered electron or positron is large enough for it to be detected, the mass of the photon emitted by the detected lepton can be measured. These events are called single-tagged events. In double-tagged events both the scattered electron and positron are detected and all five variables are known. The two-photon system can be fully determined in this case. The mass of the final state X can then be obtained directly from the measurement of the scattered particles, a so-called missing-mass measurement.

1.2 General expression for $\sigma(e^+e^- \to e^+e^- X)$

In this section the notation is followed as given by Budnev *et al.* [2] and Kolanoski [3]. The general matrix element for the process, $e^+e^- \to e^+e^- X$, can be calculated by Feynman rules:

$$\mathcal{M}_{e^+e^- \to e^+e^- X} = \frac{e^2}{q_1^2 q_2^2} \bar{u}(p_1')\gamma_\mu u(p_1) M^{\mu\nu} \bar{v}(p_2')\gamma^\nu v(p_2). \tag{1.2}$$

Here, $u(p)$ and $v(p)$ are the Dirac spinors with p corresponding to the properties of the particle (four momentum and spin). The tensor $M^{\mu\nu}$ corresponds to the hadronic two-photon reaction:

$$\gamma(q_1) + \gamma(q_2) \to X.$$

Here, q corresponds to the properties of the photon. The total cross section can be expressed in terms of $\mathcal{M}$ as follows:

$$d\sigma_{e^+e^- \to e^+e^- X} = \sum |\mathcal{M}|^2 (2\pi)^4 \frac{\delta^4(q_1 + q_2 - k)}{4\sqrt{X_{e^+e^-}}} \frac{d^3\vec{p_1'}}{(2\pi)^3 2E_1'} \frac{d^3\vec{p_2'}}{(2\pi)^3 2E_2'} d\Gamma. \tag{1.3}$$

Here, the summation is performed over the spin of the outgoing electron and positron while averaging over the spins of the initial electron and positron. The flux of the initial state particles $\sqrt{X_{e^+e^-}}$ is given by $X_{e^+e^-} = (p_1 p_2)^2 - m_1^2 m_2^2$. The phase space $d\Gamma$ of the final state X, consisting of i particles with four momenta $(E_i, \vec{k_i})$ is given by

$$d\Gamma = \sum_{\text{all spin states}} \prod_i \frac{d^3\vec{k_i}}{(2\pi)^3 2E_i}.$$

At the two QED vertices the summation over the outgoing spins and averaging over the incoming spins can be performed. This gives a density matrix for the virtual photon:

$$\begin{aligned} \rho_i^{\mu\nu} &= \frac{1}{2(-q_i^2)} \sum_{s,s'} [\bar{u}(p_i')\gamma^\mu u(p_i)][\bar{u}(p_i')\gamma^\nu u(p_i)], \\ &= \frac{1}{2(-q_i^2)} [q_i^2 g^{\mu\nu} + 2(p_i^\mu p_i'^\nu + p_i^\nu p_i'^\mu)]. \end{aligned} \tag{1.4}$$

With the help of the above equations the differential cross section can be written as:

$$d\sigma_{e^+e^- \to e^+e^- X} = \frac{\alpha^2}{4q_1^2 q_2^2} \frac{\delta^4(q_1 + q_2 - k)}{\sqrt{X_{e^+e^-}}} \rho_1^{\mu\mu'} \rho_2^{\nu\nu'} M_{\mu\nu} M^*_{\mu'\nu'} \frac{d^3\vec{p_1'}}{E_1'} \frac{d^3\vec{p_2'}}{E_2'} d\Gamma. \tag{1.5}$$

When integrating over the hadronic final states the following expression will appear in the total cross section equation:

$$W^{\mu\nu\mu'\nu'} = \frac{1}{2} \int M_{\mu\nu} M^*_{\mu'\nu'} (2\pi)^4 \delta(q_1 + q_2 - k) d\Gamma. \tag{1.6}$$

This tensor has in its most general form 256 different elements. Because photons only couple to conserved currents not all four values for each index are independent:

$$\begin{aligned} q_1^\mu W^{\mu\nu\mu'\nu'} &= 0, \qquad q_1^{\mu'} W^{\mu\nu\mu'\nu'} = 0, \\ q_2^\nu W^{\mu\nu\mu'\nu'} &= 0, \qquad q_2^{\nu'} W^{\mu\nu\mu'\nu'} = 0. \end{aligned} \tag{1.7}$$

To take this into account the photons are transformed into their helicity basis. In this new basis the hadronic tensor will be written as $A^{mnm'n'}$. The indices now run over the three possible values for the helicity $(+1, 0, -1)$. This tensor has at the most 81 independent elements. Because of conservation of angular momentum $(m - n = m' - n')$ only 19 entries are not equal to 0. Parity invariance gives $A^{mnm'n'} = A^{-m-n-m'-n'}$ and time reversal invariance gives $A^{mnm'n'} = A^{m'n'mn}$. These last two requirements lead to eight independent elements.

The eight independent elements are related to the cross sections and interference terms of the process $\gamma\gamma \to X$.

$$\begin{aligned} \sigma_{TT} &= \frac{1}{4\sqrt{X}}(A^{++++} + A^{+-+-}), & \sigma_{SS} &= \frac{1}{2\sqrt{X}}(A^{0000}), \\ \sigma_{TS} &= \frac{1}{2\sqrt{X}}(A^{+0+0}), & \sigma_{ST} &= \frac{1}{2\sqrt{X}}(A^{0+0+}), \\ \tau_{TT} &= \frac{1}{2\sqrt{X}}(A^{++--}), & \tau_{TS} &= \frac{1}{4\sqrt{X}}(A^{++00} + A^{0+-0}), \\ \tau_{TT}^a &= \frac{1}{4\sqrt{X}}(A^{++++} - A^{+-+-}), & \tau_{TS}^a &= \frac{1}{4\sqrt{X}}(A^{++00} - A^{0+-0}). \end{aligned} \tag{1.8}$$

Here, $\sqrt{X}$ is the two-photon flux factor:

$$X = (q_1 q_2)^2 - q_1^2 q_2^2 = \frac{1}{4}[W^4 - 2W^2(q_1^2 + q_2^2) + (q_1^2 - q_2^2)^2]. \tag{1.9}$$

The cross sections σ_{TT}, σ_{ST}, σ_{TS}, σ_{SS} and the interference terms $\tau_{TT}^{(a)}$ and $\tau_{TS}^{(a)}$ are real scalar functions of the scalars q_1^2, q_2^2 and W^2, with S representing a scalar photon (helicity 0) and T a transverse photon (helicity ± 1).

Implementation of all this gives an expression of the differential cross section in terms of the photon scattering cross sections:

$$\begin{aligned} d\sigma_{e^+e^- \to e^+e^- X} = \; & \frac{\alpha^2}{16\pi^4 q_1^2 q_2^2}\sqrt{\frac{X}{X_{e^+e^-}}}[4\rho_1^{++}\rho_2^{++}\sigma_{TT} + 2\rho_1^{++}\rho_2^{00}\sigma_{TS} + \\ & 2\rho_1^{00}\rho_2^{++}\sigma_{ST} + \rho_1^{00}\rho_2^{00}\sigma_{SS} - 8|\rho_1^{+0}\rho_2^{+0}|\tau_{TS}\cos\tilde{\phi} + \\ & 2|\rho_1^{+-}\rho_2^{+-}|\tau_{TT}\cos 2\tilde{\phi} + A\tau_{TT}^a + B\tau_{TS}^a]\frac{d^3\vec{p_1'}}{E_1'}\frac{d^3\vec{p_2'}}{E_2'}. \end{aligned} \tag{1.10}$$

Here, $\tilde{\phi}$ is the angle between the scattering planes of the colliding particles in the two-photon center-of-mass system. All expressions in equation 1.10 are functions of the measurable quantities p_i and p_i'. The expressions for the density matrices are given here explicitly [2]:

$$\rho_1^{++} = \rho_1^{--} = \frac{(2p_1q_2 - q_1q_2)^2}{2X} + \frac{1}{2} + \frac{2m_e^2}{q_1^2}, \tag{1.11}$$

$$\rho_1^{00} = \frac{(2p_1q_2 - q_1q_2)^2}{X} - 1, \tag{1.12}$$

$$8|\rho_1^{+0}\rho_2^{+0}|\cos\tilde{\phi} = \frac{4(2p_1q_2 - q_1q_2)(2p_2q_1 - q_1q_2)C}{X\sqrt{q_1^2q_2^2}},$$

$$2|\rho_1^{+-}\rho_2^{+-}|\cos 2\tilde{\phi} = C^2/q_1^2q_2^2 - 2(\rho_1^{++} - 1)(\rho_2^{++} - 1).$$

$$\rho_2^{++} = \rho_1^{++}(1 \leftrightarrow 2) \quad , \quad \rho_2^{00} = \rho_1^{00}(1 \leftrightarrow 2),$$

Here, $C = -(2p_1 - q_1)(2p_2 - q_2) + X^{-1}(q_1q_2)(2p_1q_2 - q_1q_2)(2p_2q_1 - q_1q_2)$. For unpolarised beams $A = B = 0$.

The interference terms vanish if expression 1.10 is integrated over $\tilde{\phi}$. After this integration the only unknown quantities in this equation are the two-photon cross sections σ_{ij}, with $i, j = S, T$. All the other terms are indicated as the two-photon luminosity functions, $\mathcal{L}_{\gamma\gamma}^{ij}$. The cross section is often rewritten as:

$$\sigma_{e^+e^-\to e^+e^-X} = \sum_{i,j=S,T} \frac{d^5\mathcal{L}_{\gamma\gamma}^{ij}}{d\omega_1 d\omega_2 d\theta_1 d\theta_2 d\phi}\sigma_{ij}. \tag{1.13}$$

When the virtualities of the photons are small, only the transverse-transverse cross section contributes to equation 1.10. This results from the transformation of the linear-polarised states to the helicity states, see [2]. When $Q_i^2 \to 0$ the four cross sections behave like:

$$\sigma_{TT}(W^2, Q_1^2, Q_2^2) \to \sigma_{\gamma\gamma}(W^2), \quad \sigma_{TS} \propto Q_2^2, \quad \sigma_{ST} \propto Q_1^2, \quad \sigma_{SS} \propto Q_1^2Q_2^2. \tag{1.14}$$

1.3 Equivalent Photon Approximation

Owing to the bremsstrahlungs spectrum of the scattering angles the largest contribution to the luminosity functions results from small angles. Small angles mean that the virtualities of the photons, Q_i^2, remain small as well. From equation 1.14 it is clear that only the transverse-transverse cross section gives a considerable contribution.

For small scattering angles ϕ coincides with $\tilde{\phi}$ and equation 1.10 can be integrated over ϕ. The density matrices can be simplified if $Q_i^2 << W^2$ with the help of the following approximations:

$$2p_1q_2 = 4Ew_2, \quad q_1q_2 = \frac{1}{2}W^2, \quad X = \frac{1}{4}W^4, \quad W^2 = 4w_1w_2. \tag{1.15}$$

Here, w_i is the energy of the photon $(E_i - E_i')$. Substitution into the transverse-transverse density matrix yields:

$$\rho_i^{++} = \frac{2E(E-w_i)}{w_i^2} + 1 - \frac{2m_e^2}{Q_i^2}. \tag{1.16}$$

The phase-space volume element of the scattered particles can be written as:

$$\frac{d^3p_1'}{E_1}\frac{d^3p_2'}{E_2} = \frac{\pi s}{2[(p_1p_2)^2 - m_1^2m_2^2]} dQ_1^2 dQ_2^2 dw_1 dw_2 d\phi. \tag{1.17}$$

Implemention of 1.14, 1.16 and 1.17 into 1.10 gives, after integration over ϕ:

$$d\sigma = \sigma_{\gamma\gamma} dn_1 dn_2. \tag{1.18}$$

Here, dn_i is called the number of equivalent photons or the photon spectrum and is given by:

$$dn_i = \frac{\alpha}{\pi}\frac{dw_i}{w_i}\frac{dQ_i^2}{Q_i^2}\left[\left(1 - \frac{w_i}{E} + \frac{w_i^2}{2E^2}\right) - \frac{m_e^2 w_i^2}{E^2 Q_i^2}\right]. \tag{1.19}$$

For the cross section calculations, the luminosity function has to be integrated over that part of phase space which contributes to a given mass W. In the Equivalent Photon Approximation the integrated luminosity is calculated as ($W^2 = \tau s$):

$$\mathcal{L}_{\mathrm{EPA}}(\tau) = \frac{1}{\tau}\int N(x_1)N(x_2 = \tau/x_1)\frac{dx_1}{x_1}.$$

Here, $x_i = w_i/E$, $\tau = x_1 x_2$ and n_i is integrated over Q^2 to give $N(x_i)$:

$$N(x_i) = \frac{\alpha}{2\pi}\left\{[1 + (1-x_i)^2]\ln\frac{Q_{i\ \mathrm{max}}^2}{Q_{i\ \mathrm{min}}^2} - 2m_e^2 x_i^2\left[\frac{1}{Q_{i\ \mathrm{min}}^2} - \frac{1}{Q_{i\ \mathrm{max}}^2}\right]\right\}.$$

The $Q_{i\ \mathrm{min}}^2$ and $Q_{i\ \mathrm{max}}^2$ depend on the experimental conditions (untagged, single or double tag).

In this thesis a slightly different approach is applied. The integral over the luminosity function is done numerically with the help of an improved equivalent-photon approximation, as given by G. Schuler [53]. The improved EPA can be written as:

$$\begin{aligned}
x_1\tau\frac{d\mathcal{L}}{dx_1} &= \int dQ_1^2 \int dQ_2^2 \sum_{a,b=T,S} f_a(x_1,Q_1^2) f_b(x_2,Q_2^2)\frac{\sigma_{ab}(W,Q_1^2,Q_2^2)}{\sigma_{\gamma\gamma}(W)}, \\
f_T(x,Q^2) &= \frac{\alpha}{2\pi}\left\{\frac{1+(1-x)^2}{Q^2} - \frac{2m_e^2x^2}{Q^4}\right\}, \\
f_S(x,Q^2) &= \frac{\alpha}{\pi}\frac{1-x}{Q^2}, \\
Q_{i\ \mathrm{min,max}}^2 &= \frac{m_e^2x_i^2}{1-x_i} + 4E^2(1-x_i)\sin^2\frac{1}{2}\theta_{i\ \mathrm{min,max}}.
\end{aligned} \tag{1.20}$$

The equation for f_S is obtained from ρ^{00} in the same way as f_T was obtained from ρ^{++} (exactly the same approximations have been applied as for equation 1.19).

If one assumes factorisation of the two-photon cross sections:

$$\sigma_{ab} = F_a(Q_1^2)F_b(Q_2^2)\sigma_{\gamma\gamma}(W),$$

the integral gives a luminosity function with the form factors $F(Q^2)$ included.

In the EPA the two photons are thus described as being produced independently (rho_i only depends on x_i and Q_i^2). In the following section the two-photon cross section is discussed and this independency will be exploited to describe the different contributions to the total hadronic two-photon cross section.

1.4 The hadronic two-photon cross section

In this thesis the cross section is measured for large two-photon masses. This means that the region of interest corresponds to masses above the resonances (larger than about 2 GeV). The lowest order diagram for hadron production in two-photon collisions is shown in 1.2 a. The diagrams 1.2 b, c and d are in principal higher-order diagrams of 1.2 a.

The behaviour of the two photons can be characterised in the following way when the EPA picture is applied. The two photons are produced independently and each couples to a quark-antiquark pair. When the transverse energy of a pair is low (the mass of the pair is then small as well) the quark-antiquark pair will in general form a vector meson before the interaction with the other photon or quark pair takes place. When the transverse energy is large enough this will not happen and the quarks can interact individually.

The scattering takes place between (anti)quarks from the two different photons. When the scattering is hard enough (the transferred momentum between the scattered particles is large), an exchanged gluon would be able to distinguish the quark from the antiquark of one photon or both photons, and the process is called single or double resolved, respectively. The phase space of each photon is thus divided in three parts:

- The mass of the quark-antiquark pair is small and the photon couples to a vector meson.
- The mass of the quark-antiquark pair is large and the scattering is hard enough to distinguish the quark-antiquark pair, the photon is called anomalous.
- The mass of the quark-antiquark pair is large but the scattering is not hard enough, the photon is called direct or bare.

These three descriptions for the photon are valid for both photons. Hence six different types of interaction can be defined:

- Vector-meson vector-meson interaction, this is called the vector-meson dominance model, see 1.2 b.
- Vector-meson anomalous interaction, this a double resolved process, see figure 1.2 c.
- Vector-meson direct interaction, this is a single resolved process, see figure 1.2 d.

- Anomalous anomalous interaction, again a double resolved process, see figure 1.2 c.
- Anomalous direct interaction, again a single resolved process, see figure 1.2 d.
- Direct direct interaction, this is the Quark Parton Model or direct contribution, see figure 1.2 a.

The different diagrams must thus be regarded as representations for different parts of phase space. In the following sections the cross sections for the different contributions are given.

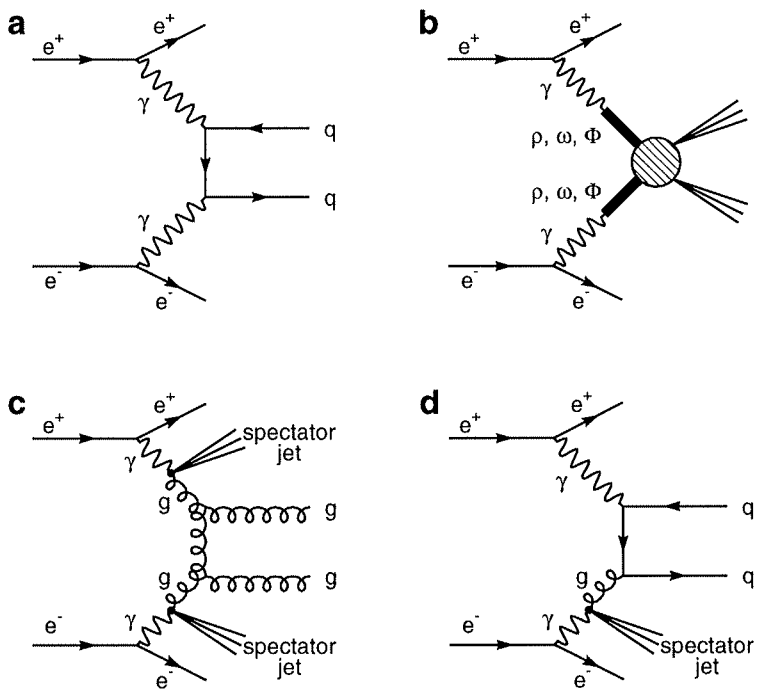

Figure 1.2: *The different contributions to the total hadronic two-photon cross section: (a) the direct or QPM contribution and (b) the Vector-meson Dominance Model contribution. In the bottom plots two examples of the anomalous contribution are shown: (c) double resolved and (d) single resolved.*

1.4.1 Vector-meson Dominance Model

The main contribution for the total cross section results from figure 1.2 b. Each photon couples to a vector meson with the same quantum numbers as the photon. The two vector

mesons scatter, producing the final state hadrons. The probability for a photon to couple to a vector meson is given by $(4\alpha\pi/\gamma_V^2)$. This gives:

$$\sigma_{\gamma\gamma\to X}^{VDM} = \sum_{V,V'} \frac{4\alpha\pi}{\gamma_V^2}\frac{4\alpha\pi}{\gamma_{V'}^2}\sigma(VV' \to X). \tag{1.21}$$

The VDM cross section is factorised in a mass dependent part and two Q^2 dependent parts, separate for both photons. When for the meson-meson cross sections the Donnachie-Landshoff parametrisation [11] is used, the mass dependence of the VDM contribution can be calculated as shown by Schuler and Sjöstrand [12, 13]. They obtained:

$$\sigma_{\gamma\gamma\to X}^{VDM} \approx 133\left(\frac{s}{s_0}\right)^{\epsilon} + 170\left(\frac{s}{s_0}\right)^{\eta} \text{ nb}. \tag{1.22}$$

Here, $\epsilon = 0.0808$, $\eta = 0.4525$ and $s_0 = 1$ GeV^2. The Q_i^2 dependence of the VDM is given by the form factors of the vector mesons. A modification of this dependence is the generalised vector-meson dominance model (GVDM [14]). The factorisation is different for each helicity cross section:

$$\sigma_{ij}^{GVDM}(W, Q_1^2, Q_2^2) = \sigma_{\gamma\gamma}(W)F_i(Q_1^2)F_j(Q_2^2). \tag{1.23}$$

Here $i, j = S, T$ and

$$\begin{aligned} F_T(Q^2) &= \sum_{V=\rho,\omega,\phi} r_V \left(\frac{m_V^2}{Q^2+m_V^2}\right)^2 + r_C\frac{m_0^2}{Q^2+m_0^2}, \\ F_S(Q^2) &= \sum_{V=\rho,\omega,\phi} r_V \left(\frac{m_V^2}{Q^2+m_V^2}\right)^2 \frac{Q^2}{4m_V^2}, \end{aligned} \tag{1.24}$$

with $m_0 = 1.4$ GeV. The r_V are given by the ratio of the total cross section of helicity 1 vector mesons and photons on a proton target:

$$r_V = \frac{4\alpha\pi}{\gamma_V^2}\frac{\sigma_{Vp}^{\lambda=\pm1}}{\sigma_{\gamma p}}, \tag{1.25}$$

with $r_\rho = 0.65$, $r_\omega = 0.08$, $r_\phi = 0.05$ and $r_C = 1 - \sum r_V$. The TPC/2γ collaboration used a slightly different parametrisation. The sum of r_V was renormalised to 1 and the term involving m_0, the continuum term, was omitted (VDM form factors).

Also the simple ρ form factor can be described in terms of the GVDM. The weights for the other vector mesons and the continuum term are put to zero. Thus $r_\rho = 1$, $r_\omega = 0$, $r_\phi = 0$ and $r_C = 0$.

The interaction between two hadrons is dominated by soft interactions. This implies that the transferred energy is small and parametrisations are applied to describe the different subprocesses, such as elastic, single-, double- and non-diffractive interaction. These interactions between two vector mesons normally produce hadronic final-state particles with directions close to the direction of the initial vector mesons. The hadronic final state is thus strongly forward peaked.

Total hadronic cross-section estimations

In 1971 J.L. Rosner [4] was the first to utilise the coupling of the photon to the vector mesons to estimate the total two-photon cross section for real photons with Regge theory [5].

This theory gives a general description of the interaction between two hadrons at high-energy and small-momentum transfer via an exchange mechanism. The exchanged object is described in a reggeised fashion, which means that it is given a continuously varying spin. This "particle", a Reggeon, corresponds to a family of particles which all have the same quantum numbers except for their values of the spin. When the squared values of the masses of these particles are plotted versus their spin, they lay on a straight line $\alpha(t)$, a Regge trajectory.

The single-Reggeon amplitude for the scattering between two hadrons, h and h' can be written as

$$A(s,t) = g^0_{\mathbb{R}h} g^0_{\mathbb{R}h'} \eta(\alpha(t)) \left(\frac{s}{s_0}\right)^{\alpha(t)} \exp(b^0 t).$$

Here, s is the center-of-mass energy squared, t is the momentum transfer, $g^0_{\mathbb{R}h}$ denotes the momentum-transfer-independent part of the Reggeon-hadron coupling constant and $s_0 = 1$ GeV^2. The corresponding Regge trajectory is given by:

$$\alpha(t) = \alpha(0) + \alpha'(0)t.$$

The signature function η is given by:

$$\eta(\alpha(t)) = -\{1 + \sigma \exp(-i\pi\alpha(t))\}/\sin \pi\alpha(t).$$

where $\sigma = \pm 1$ is the signature of the trajectory ($+1$ for trajectories with even-spin particles and -1 for trajectories with odd-spin particles). The exponent $b^0 = \frac{1}{2}b^0_h + \frac{1}{2}b^0_{h'}$ results from the coupling constants

$$g_{\mathbb{R}h}(t) = g^0_{\mathbb{R}h} \exp(\frac{1}{2} b^0_h t).$$

The optical theorem relates the elastic scattering amplitude to the total cross section in the following way:

$$\sigma^{\text{tot}} = \frac{1}{s}\text{Im}\{< i|A|i >\} = \frac{1}{s}\text{Im}\{A^{\text{el}}(s, t = 0)\}.$$

Within the Regge model the total cross section for the interaction between two hadrons is a sum of two terms describing the exchange of the elusive Pomeron, $\mathbb{P}$, (this trajectory has no particles associated with it) and the ρ, A_2-Regge trajectory, $\mathbb{R}$, (the signature of the ρ trajectory is opposite to the A_2 trajectory, the identity between two trajectories with opposite signature is called 'exchange degeneracy'):

$$\sigma^{TOT}_{hh' \to X}(s) = \sigma^{\mathbb{P}}_{hh' \to X}(s) + \sigma^{\mathbb{R}}_{hh' \to X}(s). \tag{1.26}$$

Within the Regge model the cross section for each of these two terms is given by:

$$\sigma^{\mathbb{R}}_{hh'\to X}(s) = g^0_{\mathbb{R}h} g^0_{\mathbb{R}h'} \left(\frac{s}{s_0}\right)^{\Delta\mathbb{R}}, \qquad \sigma^{\mathbb{P}}_{hh'\to X}(s) = g^0_{\mathbb{P}h} g^0_{\mathbb{P}h'} \left(\frac{s}{s_0}\right)^{\Delta\mathbb{P}}. \tag{1.27}$$

Here, $g^0_{\mathbb{R}h}$ and $g^0_{\mathbb{P}h}$ are the couplings terms, $\Delta\mathbb{R} = \alpha^{\mathbb{R}}(0) - 1$ with $\alpha^{\mathbb{R}}(0) \approx 0.5$ and $\Delta\mathbb{P} = \alpha^{\mathbb{P}}(0) - 1$ with $\alpha^{\mathbb{P}}(0) \approx 1$.

For the calculation of the total two-photon cross section the measurements of hh and γh interactions were taken. For the Pomeron term (high-energy behaviour) Rosner used γN and NN scattering data:

$$\sigma^{\mathbb{P}}_{\gamma\gamma\to X} = \frac{[\sigma^{TOT}_{\gamma N}(s\to\infty)]^2}{\sigma^{TOT}_{NN}(s\to\infty)} \approx 240 \text{ nb}. \tag{1.28}$$

For the low-energy behaviour, the Regge trajectory exchange, $p\bar{p}$, $\bar{p}n$, γp and γn interactions were taken:

$$\sigma^{\mathbb{R}}_{\gamma\gamma\to X} = 270 \left(\frac{s}{s_0}\right)^{-0.5} \text{ nb, with s in GeV}^2. \tag{1.29}$$

The Rosner result can thus be written as:

$$\sigma^{TOT}_{\gamma\gamma\to X} = 240 + 270 \left(\frac{s}{s_0}\right)^{-0.5} = 240 \text{ nb} + \frac{270 \text{ nb}\cdot\text{GeV}}{W}. \tag{1.30}$$

This form for the cross section has also been used by other authors [6–10].

In 1992 P.V. Landshoff and A. Donnachie [11] fitted the cross section for nine different hadron-hadron interactions ($p\bar{p}$,pp,π^+p,π^-p, K$^+$p,K$^-$p,γp,$p\bar{n}$ and pn) with the following parametrisation:

$$\sigma^{TOT}_{hh'\to X} = X\left(\frac{s}{s_0}\right)^{\epsilon} + Y\left(\frac{s}{s_0}\right)^{\eta}. \tag{1.31}$$

They assumed universality for the exponents $\epsilon = \alpha^{\mathbb{P}}(0) - 1$ and $\eta = \alpha^{\mathbb{R}}(0) - 1$. The value for these two exponents were taken from a fit of the pp and $p\bar{p}$ data, requiring the same value for X (assuming that the Pomeron couples in the same way to the particle as to the antiparticle), ϵ and η. This gave:

$$\epsilon = 0.0808, \quad \eta = -0.4525. \tag{1.32}$$

In 1994 G.Schuler and T.Sjöstrand [12, 13] utilised the parametrisation of Landshoff and Donnachie, together with the factorisation of the Regge model.

$$X_{\gamma\gamma} = \frac{(X_{\gamma p})^2}{X_{pp}}, \quad Y_{\gamma\gamma} = \frac{(Y_{\gamma p})^2}{Y_{pp}}. \tag{1.33}$$

Their result was:

$$\sigma^{TOT}_{\gamma\gamma\to X} = 211\left(\frac{s}{s_0}\right)^{\epsilon} + 297\left(\frac{s}{s_0}\right)^{\eta} \text{ nb}. \tag{1.34}$$

If $Y_{p\bar{p}}$ is taken the Regge factor would be 169, if one uses $\frac{1}{2}(Y_{pp} + Y_{p\bar{p}})$ the result would be 215. These differences do not affect the high-energy behaviour of the total cross section, which is described by the Pomeron term.

Rosner, and later Schuler and Sjöstrand, thus assumed that the two-photon cross section behaves like a hadron-hadron cross section. These total cross-section predictions are thus VDM based predictions. The difference between equation 1.34 and 1.22 shows that the other contributions to the total two-photon cross section are needed.

1.4.2 Direct cross section

This contribution describes the process in which the two photons couple directly to a quark-antiquark pair, see figure 1.2 a.

The cross sections for this contribution can be calculated with the help of Feynman diagrams and can be found in different text books, e.g. [3]. The Q^2 dependence can be found in [2]. As an example the σ_{TT} and σ_{ST} will be given here in the case that $Q_2^2 \approx 0$:

$$\begin{aligned}\sigma_{TT} &= \frac{2N_c e_q^4 \pi\alpha^2 W^4}{(W^2+Q_1^2)^3}\left\{\left(3-\beta^4+2\frac{Q_1^4}{W^4}\right)\ln\frac{1+\beta}{1-\beta}+\right.\\ &\qquad\left.2\beta\left(\beta^2-2+2\frac{Q_1^2}{W^2}-\frac{Q_1^4}{W^4}\right)\right\}, \qquad (1.35)\\ \sigma_{ST} &= \frac{8N_c e_q^4 \pi\alpha^2 W^2 Q_1^2}{(W^2+Q_1^2)^3}\left\{(1-\beta^2)\ln\frac{1+\beta}{1-\beta}-2\beta\right\}. \qquad (1.36)\end{aligned}$$

Here, e_q is the charge of the quark, $N_c = 3$ the colour factor and β is the velocity of the quark in the two-photon center-of-mass system. As can be seen in equation 1.36 the σ_{ST} is proportional to Q^2 for small values of Q^2 and vanishes for real photons. Also the angular distribution can be calculated. In a lowest-order calculation and for real photons the scattering angle θ of the quarks with respect to the photon direction in the two-photon center-of-mass system is given by [3, 15]:

$$\frac{d\sigma_{\gamma\gamma\to q\bar{q}}}{d\Omega} = e_q^4\frac{N_c\alpha^2\beta}{W^2}\frac{2\beta^2\sin^2\theta-\beta^4\sin^4\theta+1-\beta^4}{(1-\beta^2\cos^2\theta)^2}. \qquad (1.37)$$

In the mass region of interest, $m_q << W$ with m_q the mass of the quark, β approaches one and the angular distribution becomes forward peaked. But at large angles the direct cross section becomes more important with respect to the VDM cross section, which is even more strongly forward peaked than the direct cross section.

1.4.3 Anomalous cross sections

Here the cross sections of the four other contributions are given. In these contributions the transverse energy in the scattering process is large. This implies that the exchanged gluon can resolve the constituents of one or both photons. In the anomalous processes the constituent of one photon can either interact directly with the other photon (single

resolved, see 1.2 d) or with a constituent of the second photon (double resolved, see 1.2 c). The anomalous cross sections are calculated in the "hard scattering expansion":

$$\sigma_{\gamma\gamma\to X}^{\text{double resolved}} = \sum_{ijk} \int dx_1 \int dx_2 f_i^\gamma(x_1, P^2) f_j^\gamma(x_2, P^2) \sigma_{ij\to k}(\hat{s}), \tag{1.38}$$

$$\sigma_{\gamma\gamma\to X}^{\text{single resolved}} = \sum_{ik} \int dx_1 f_i^\gamma(x_1, P^2) \sigma_{i\gamma\to k}(\hat{s}). \tag{1.39}$$

Here, $f^\gamma(x_i, P^2)$ are the particle density functions (pdf) of the photon. They describe the probability to find the constituent carrying an energy xE_γ. The subdivision of the single and double resolved processes into an anomalous and a VDM part is done with the help of different pdf's for the two parts. Also pdf's with a parametrisation for the total resolved photon exist. These make thus no subdivision in anomalous and VDM parts. The scale at which these pdf's are calculated is given by P^2. This scale depends on the hard process itself. The summation over i and j runs over all constituents of the photon, thus over all (anti-)quarks and the gluon. The summation over k runs over all final states which can be produced by the initial state ij or $i\gamma$. Normally the lowest-order Feynman diagrams are considered for the cross sections $\sigma_{ij\to k}$ and $\sigma_{i\gamma\to k}$, calculated at an energy $\hat{s} = x_1 x_2 s$. Recall that here $s = W^2$ and $x_2 = 1$ for single resolved processes.

The input pdf's thus play an important role in the calculation of these cross sections. They can be calculated from the lowest-order diagram. Witten [17] showed that substantial strong-coupling corrections are needed, even at lowest order. Later other authors calculated the pdf's and found similar results.

When the next-to-leading order contributions were calculated , large corrections were found. This means that no indication for the convergence of the pdf's was found. This seems to indicate that in this case, like in the deep-inelastic lepton-hadron scattering, the pdf's must be measured at a certain value of Q^2 and can not be derived from calculations alone. The Q^2 evolution can then be calculated with the Altarelli-Parisi equations [16].

Many parametrisations exist for the pdf's of the photon, e.g. Duke and Owens (DO) [18], Levy, Abromowicz and Charchula (LAC) [19,20], Drees and Grassi (DG) [21], Glück, Reya and Vogt (GRV) [22] and Schuler and Sjöstrand (SaS) [23,24].

1.5 Monte Carlo generators

In order to compare the abovementioned models with the data, Monte Carlo samples must be generated. The events in each sample can be passed through the detector simulation and the event variables for the data and the MC samples can then be compared. Here two different MC generators will be described. Both generators only have interactions between real photons.

1.5.1 PHOJET

The generator PHOJET applies the Dual-Parton Model [25,26] to describe the interaction. In this generator the physical photon is considered to be a superposition of a bare photon

and virtual hadronic states. The hadronic state is split into two generic states. The low mass state, $|q\bar{q}>$ corresponds to a superposition of the vector meson states ρ, ω and ϕ and a $\pi^+\pi^-$ background. The state $|q\bar{q}^*>$ is an approximation for hadronic states with higher masses. The wave function of the physical photon is given by:

$$|\gamma>=\sqrt{Z_3}|\gamma_{\text{bare}}>+\frac{e}{f_{q\bar{q}}}|q\bar{q}>+\frac{e}{f_{q\bar{q}^*}}|q\bar{q}^*>.$$

Here, $\frac{e}{f_{q\bar{q}}}$ and $\frac{e}{f_{q\bar{q}^*}}$ are the probabilities for the photon to be in the given state, and unitarity gives $Z_3 = 1 - \frac{e^2}{f^2_{q\bar{q}}} - \frac{e^2}{f^2_{q\bar{q}^*}}$. Normally the value for Z_3 is close to unity ($Z_3 \approx 1$).

The interactions are described in terms of Reggeon and Pomeron exchanges. For soft interactions, photon-hadron duality is assumed. The Pomeron exchange is artificially subdivided into processes involving only soft subprocesses and all the other processes with at least one large momentum transfer (hard subprocesses). The soft and hard subprocesses are separated by applying a transverse-momentum cutoff $p_\perp^{\text{cutoff}}$ to the partons. On Born-graph level, the different photon-photon cross sections read:

- soft resolved processes:

$$\sigma^{\text{tot}}_{\mathbb{P}}(s) = \left(\frac{e^2}{f^2_{q\bar{q}}}\right) g^0_{\mathbb{P},q\bar{q}} g^0_{\mathbb{P},q\bar{q}} \left(\frac{s}{s_0}\right)^{\Delta\mathbb{P}}.$$

Here, $\Delta\mathbb{P} = \alpha_{\mathbb{P}}(0) - 1$, $\alpha_{\mathbb{P}}(0)$ is the Pomeron intercept and $g^0_{\mathbb{P},q\bar{q}}$ the coupling of the Pomeron to the hadronic fluctuation. Similar expressions for the Reggeon exchange exist.

- hard resolved processes:

$$\sigma^{\text{hard}}_{\text{res.}}(s, p_\perp^{\text{cutoff}}) = \int dx_1 dx_2 d\hat{t} \sum_{ijk} f_i^\gamma(x_1,\mu^2) f_j^\gamma(x_2,\mu^2) \frac{d\sigma^{\text{QCD}}_{ij\to k}(\hat{s},\hat{t})}{d\hat{t}} \Theta(p_\perp - p_\perp^{\text{cutoff}}).$$

- single direct processes:

$$\sigma_{\text{s-dir}}(s, p_\perp^{\text{cutoff}}) = \int dx d\hat{t} \sum_{ik} f_i^\gamma(x,\mu^2) \frac{d\sigma^{\text{QCD}}_{\gamma i\to k}(\hat{s},\hat{t})}{d\hat{t}} \Theta(p_\perp - p_\perp^{\text{cutoff}}).$$

- double direct process:

$$\sigma_{\text{d-dir}}(s, p_\perp^{\text{cutoff}}) = \int d\hat{t} \sum_{k} \frac{d\sigma_{\gamma\gamma\to k\bar{k}}(\hat{s},\hat{t})}{d\hat{t}} \Theta(p_\perp - p_\perp^{\text{cutoff}}).$$

The same equations are also valid for the high mass state $|q\bar{q}^*>$. The pdf's applied are the leading order GRV parton distributions [22] and they are sampled at $\mu^2 = p_\perp^2$.

The probabilities to find a photon in one of the generic states, the coupling constants to the reggeon and Pomeron and the effective reggeon and Pomeron intercepts can not be determined by basic principles. These quantities are treated as free parameters. It

was shown in [27] that it is possible to fix the free parameters by a global fit to the proton-proton and proton-photon cross sections and elastic slope parameters.

For hard scattering processes, the complete parton kinematics and flavours/colours are sampled according to the Parton Model. For soft processes, the partonic interpretation of the Dual-Parton Model is applied: photons and mesons are split into a quark-antiquark pair. The longitudinal momentum fraction of the soft partons are given by Regge asymptotics [28]: $\rho(x) \sim \frac{1}{\sqrt{x(1-x)}}$. The transverse momenta of the soft partons are sampled from an exponential distribution (with an energy-dependent slope) in order to have a smooth transition between transverse momentum distributions of the soft constituents and the hard scattered partons.

The fragmentation of the sampled partonic final states is performed by forming colour neutral strings between the partons according to the colour flow. These strings are fragmented with the help of the LUND fragmentation code JETSET 7.3.

1.5.2 PYTHIA

The PYTHIA generator [29] is a general purpose generator. The photon-photon interactions are described in [12, 13]. The hadronic fluctuations of the photon are split in a low-virtuality and a high-virtuality part. The former part can be approximated by a sum over low-mass vector-meson states. The high-virtuality part is calculated with the help of perturbative QCD. The photon wave function can be written as

$$|\gamma >= c_{\text{bare}}|\gamma_{\text{bare}} > + \sum_{V=\rho,\omega,\phi,J/\psi} c_V|V > + \sum_{q=u,d,s,c,b} c_q|q\bar{q} > + \sum_{l=e,\mu,\tau} c_l|l^+l^- > .$$

The high- and low-virtuality parts are separated by a cutoff parameter, k_0. The coefficients c_f (f=quark or lepton) depend on the scale μ applied to probe the photon:

$$c_f|f\bar{f} >= \frac{\alpha}{2\pi} 2e_f^2 \int_{k_0^2}^{\mu^2} \frac{dk^2}{k^2}|f\bar{f}; k^2 > .$$

Here, k is the virtuality or transverse momentum scale of the fluctuation. The low-virtuality $q\bar{q}$ fluctuations are below k_0. In conventional notation $c_V^2 = \frac{4\pi\alpha}{f_V^2}$, with $f_V^2/4\pi$ determined from data [30]. c_{bare} is given by unitarity: $c_{\text{bare}}^2 \equiv Z_3 = 1 - \sum c_V^2 - \sum c_q^2 - \sum c_l^2$. Usually the probing scale μ is taken to be the transverse momentum of a $2 \to 2$ parton-level process.

In PYTHIA six different types of events contribute to the hadronic cross section (the leptonic part of the photon is neglected). A photon can be a VMD type, anomalous type or a direct photon depending on the virtuality of the $q\bar{q}$ fluctuation and the transverse momentum of the interaction (see figure 1.3).

If the virtuality of the fluctuation is smaller than k_0 for both photons, the process is a VMD×VMD interaction. This is a scaled down version of $\rho^0\rho^0$ and other vector-meson processes [31, 32]:

$$\sigma_{\text{VMD}\times\text{VMD}}^{\gamma\gamma} = \sum_{V_1} \frac{4\pi\alpha}{f_{V_1}^2} \sum_{V_2} \frac{4\pi\alpha}{f_{V_2}^2} \sigma_{\text{tot}}^{V_1V_2}.$$

These VMD events are further subdivided in elastic, single-, double- and non-diffractive events. The non-diffractive part is split into a hard and a soft part. These two parts are separated by a transverse momentum cutoff:

$$p_{\perp\min}^{VMD} \approx \left(1.30 + 0.15\frac{\ln(\sqrt{s}/200\ \text{GeV})}{\ln(900/200)}\right)\ \text{GeV}.$$

For the high-$p_\perp$ events the hard scattering expansion can be applied for this contribution. The cross sections used have been calculated and parametrised and were presented in [32] and [31]. The pdf used for the calculation of the high-$p_\perp$ part is taken from [23]. In this parametrisation separate parts for a parton in a vector meson (VMD pdf) and for a parton in a high-virtuality fluctuation (anomalous pdf) exist.

When the virtuality of one photon becomes larger than k_0 the VMD picture is not valid any more. The photon is then considered to be either a direct (bare) or an anomalous photon. When the transverse momenta of the scattered quarks becomes larger than the virtuality of the photon, a gluon which could be transferred will be capable of distinguishing the two quarks. The photon is called anomalous. If the transferred energy is too small, the gluon can not distinguish the two quarks and the object seen would be colourless, the photon is a direct or bare photon.

This gives three possibilities for one photon and thus six different types of interactions. The cross section for the processes involving one or two non-VMD photons are calculated in the hard scattering expansion. The pdf's applied are different for a VMD photon or anomalous photon [23].

Also the anomalous processes have a minimum transverse momentum, $p_{\perp\min}^{\text{anom}}$, which is parametrised as:

$$p_{\perp\min}^{\text{anom}}(s) \approx \left(0.6 + 0.25\ln^2(1+\sqrt{s}/10\ \text{GeV})\right)\ \text{GeV}.$$

This leaves a gap in the phase space of the photon (the area with the question mark in figure 1.3). This is done in order to make the cross section for the sum of the six interaction types behave like the Pomeron-style cross section of equation 1.34.

1.6 Summary of previous experimental results

The results obtained with the three different approaches mentioned before (untagged, single and double tagged) are summarised here.

Double-tagged experiments

The main advantage of double-tagged events is that the mass of the two-photon hadronic state can be derived directly from the detected energies and angles of the positron and electron. Also information about the interference terms can be obtained by investigating the angle between the two scattering planes. Experimentally the advantage is that these events can be triggered with dedicated triggers. This ensures high trigger efficiency and therefore small uncertainties due to the trigger. A major disadvantage is that the number of events is reduced significantly due to the luminosity function which decreases sharply

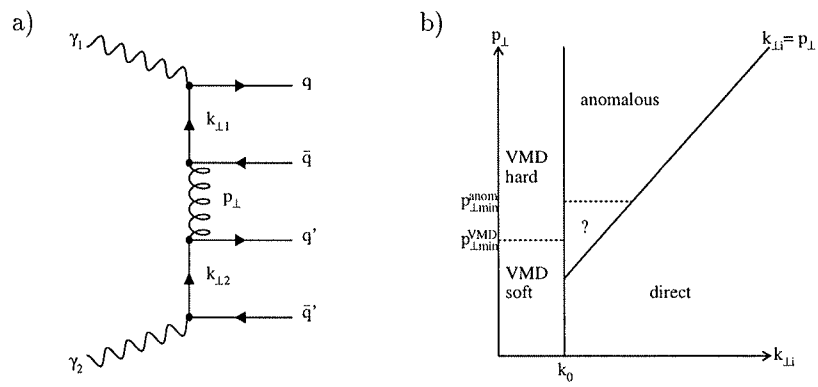

Figure 1.3: *The hard interaction between two real photons: (a) a Feynman diagram for a hard process and (b) a two-dimensional phase-space graph for the two scales of one photon, with the subdivision into the different types for the photon (VMD, anomalous or direct).*

with increasing values for Q^2. A second disadvantage is the need for extrapolation of the measured cross section to the total cross section at $Q_1^2 = Q_2^2 = 0$.

In 1985 the TPC/2γ collaboration published their result for the total cross section obtained with double-tagged events [33]. This data was taken at SLAC with the PEP facility. The electron-positron center-of-mass energy was 29 GeV. The tags were measured in an angular range from 22 to 90 mrad. This resulted in a Q^2 range from 0.1 to 1.6 GeV^2, with an average of 0.3 GeV^2. They found that their Q^2 dependence was well described by the GVDM model. The total cross section was extrapolated from the result at $< Q^2 >= 0.3$ GeV^2 to $< Q^2 >= 0.$ GeV^2 with this GVDM model. The mass dependence was measured between 2 and 20 GeV. (the triangles in figure 1.4).

In 1984-1985 the MD-1 collaboration collected double-tagged data with the VEPP-4 collider at Novosibirsk. The e^+e^- centre-of-mass energy was between 7.7 and 9.7 GeV. Their results were published in 1991 [34]. The MD-1 detector has a magnetic field transverse to the orbit plane of the colliding beams. Due to this field the tagging can be performed for small scattering angles, a minimum angle of 0.5 mrad was applied in the analysis which resulted in an average virtuality of 0.005 GeV^2. They reported the mass dependence between 1.25 and 4.25 GeV (the open crosses in figure 1.4). They concluded that the measurement was in agreement with the Rosner prediction.

Single-tagged experiments

In the single-tag approach the number of events is larger than for the double-tagged approach but lower than for the untagged analysis. The two-photon events can still be easily recognised by the tag and dedicated triggers can thus be applied. The electron or positron which is not detected is measured over a Q^2 range from 0 to a certain maximum

$Q^2_{\text{max}} \approx E^2_{\text{beam}}\theta^2_{\text{max}}$. The detector setup gives the value for θ_{max}. Due to the sharply decreasing luminosity function the average value of Q^2 for the undetected particle will be small. The main disadvantage of this method (also for the untagged approach) is that the mass of the hadronic system is not precisely determined. This is due to the diffractive nature of the VDM-type events. A significant fraction of the energy of these events is lost or not well reconstructed due to showers along the direction of the initial beams. In order to relate the measured mass distribution to the true mass distribution a technique called unfolding is applied. The unfolding procedures introduce extra uncertainties and thus increase the systematical uncertainty; also the true mass bins will be correlated and these correlations give extra complications for performing fits or presenting the data.

In 1984 the PLUTO collaboration presented their single tagged analysis [35, 36]. The data was taken at DESY with the PETRA collider. The tags were detected in three different taggers (Small Angular Tagger, Large Angular Tagger and the EndCap). The Q^2 values ranged from 0.1 to 130 GeV^2. The masses ranged from 1.5 to 10 GeV. They found that the best description of the data was an incoherent sum of the direct (QPM) contribution plus a VDM cross section which was a fitted constant scaled with the GVDM form factor (see figure 1.5). They applied the GVDM form factors to extrapolate their tagged cross section to the total cross section (the squares in figure 1.4).

In 1990 the TPC/2γ showed single-tagged measurements of the total cross section [37]. The virtuality of the tag was measured over a range in Q^2 from 0.2 to 60 GeV^2 with both NaI and lead-scintillator shower counters for the low-Q^2 data (up to 6.8 GeV^2) and a pole-tip calorimeter for the high-Q^2 data (starting from 10 GeV^2). The mass was measured over a range from 2 to 10 GeV. They found that the Q^2 dependence of the data (see figure 1.5) was best described by a QPM contribution plus a VDM term. The VDM term was fitted with the GVDM form factors with the continuum term omitted and the weight factors, r_V renormalised to one. For the extrapolation of the low-Q^2 data to $Q^2 = 0$ the GVDM form factor was appled, in order to enable a comparison between their results (the diamonds in figure 1.4), the PLUTO single-tagged and the TPC/2γ double-tagged results.

Untagged experiments

The largest number of events is obtained when untagged data is selected. Again due to the sharply decreasing luminosity function the average value for Q^2 will be small, and therefore the extrapolation towards $Q^2 = 0$ will be small. The problems concerning the visible and true mass are relevant here as well as for the single-tagged data. Another disadvantage is that the events have no clear signature (tag) which distinguishes a two-photon event from an annihilation event. The selection criteria in the untagged case are thus more strict than in the single and double tagged approach, and the triggers have to be more general which results in larger uncertainties in the calculation of the trigger efficiencies.

In 1986 the PLUTO collaboration presented their untagged results obtained in 1981/82 [38]. The average value for Q^2 was 0.008 GeV^2. The mass ranged from 2 to 10 GeV (the circles in figure 1.4). Their result was in agreement with their single-tag analysis with the GVDM extrapolation, although the rise at small W was not clear.

The CELLO collaboration presented their untagged data in 1991 [39]. This experiment was also performed at DESY at the PETRA facility.

Both the untagged and single-tag data were presented. From their analysis of jet properties they concluded that for the description of the untagged data, next to a QPM and a GVDM contribution, a third model was needed to account for the excess of events with high-transverse-energy jets, $p_t^{\rm jet} > 2$ GeV. Due to this third component the visible mass distribution was not unfolded. A description for this component is needed as an input in the unfolding procedures. The low-p_t jets and the tagged events were well represented by an incoherent sum of GVDM and QPM.

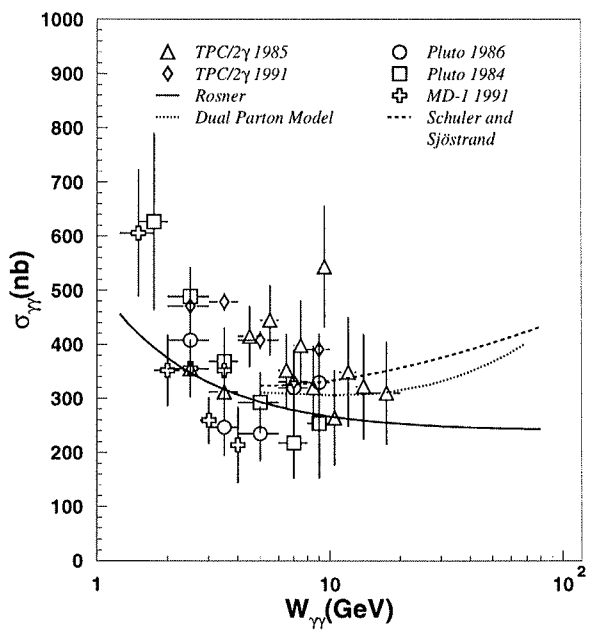

Figure 1.4: *The results for the mass dependence of the total cross section from the measurements discussed in the text.*

Summarising

The cross section as a function of the mass, shown in figure 1.4, is compatible with a flat distribution for large masses. Only the rise for very small masses is clearly visible. The prediction made by Rosner describes the cross section reasonably. The other two models give a better description of the cross section behaviour. Both these models were obtained by considering the results for the γp and pp(p$\bar{\rm p}$) total cross sections.

The uncertainties for the cross sections are large for all results. This is due to the fact that the interactions are not fully understood, which gives large systematical uncertainties (the main contribution results from the differences in modelling the final state). The unfolding needed for untagged and single-tagged data, introduces additional uncertainties. Most of the results for the total cross section come from extrapolating single- and double-tagged results, this again introduces extra uncertainties. The PLUTO 1986 is the only

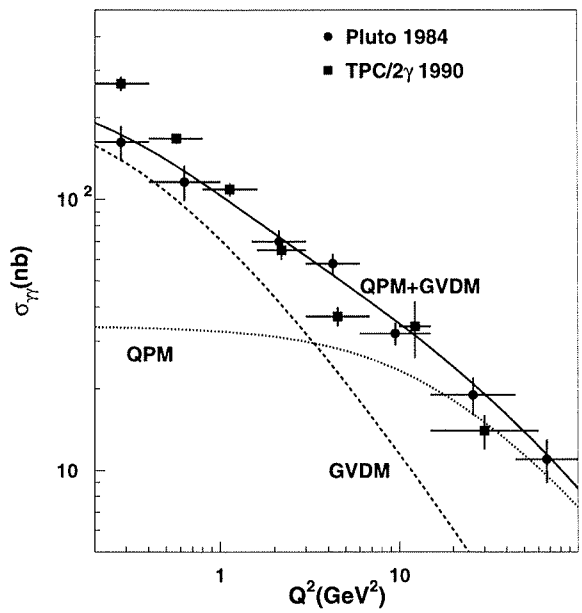

Figure 1.5: *The results for the Q^2 dependence of the total cross section from two single-tag measurements (within the same mass range between 3 and 10 GeV) discussed in the text. The GVDM form factor is multiplied with a factor determined by PLUTO, $\sigma_{\gamma\gamma} = 232 \pm 15$ nb.*

result obtained with untagged data, they were presented at the 1986 conference in Paris but never officially published.

The MD-1 results have small extrapolations and their true masses are obtained directly from the final-state electron and positron, so no unfolding was needed. In order to estimate the selection efficiency the final state still needed to be modelled. Due to the low integrated luminosity the statistical uncertainties gave the largerst contribution to the total uncertainties (they remained larger than the systematical uncertainties).

The cross section as a function of the virtuality of the photon is better understood. By integrating over all masses, no unfolding is needed, which reduces the total uncertainty. The best description is obtained by a sum of the QPM and a GVDM contribution. The results obtained by TPC/2γ and PLUTO agree for large values of the virtuality but disagree for small values.

2

The L3 Detector

In this chapter the experimental set-up will be explained. First the accelerator is introduced. Then the L3 detector will be discussed together with the triggers. At the end the reconstruction of the two-photon visible mass is explained and some remarks concerning the treatment of the MC samples are given.

2.1 Introduction

The L3 detector is one of the four experiments located at the Large Electron Positron collider (LEP) at CERN. The LEP accelerator is located at the Swiss French border near Geneva (see figure 2.1). The accelerator is built in a tunnel 50 to 170 m below the surface. The shape of the tunnel is a rounded octant, consisting of eight straight sections of 490 m and eight bending sections of 2840 m. Each bending section consists out of 3304 dipole magnets to keep the electron and positron beams inside the vacuum tube. The energy loss due to synchrotron radiation is compensated by acceleration cavities in two of the eight straight sections. In four other straight sections the four large experiments are situated: L3, OPAL, ALEPH and DELPHI.

The electron and positron beams are accelerated by four other accelerators before they are injected into the LEP storage ring. The beams are created in the LEP Injector Linacs, this facility delivers 12-ns pulses at an energy of 600 MeV. The Electron Positron Accumulator accumulates these pulses into bunches. The Proton Synchrotron (PS) accelerates the bunches up to 3.5 GeV. The Super Proton Synchrotron (SPS) injects the bunches into the LEP ring with an energy of 20 GeV. The acceleration cavities bring the energy of the bunches up to the desired value.

In the first years of running, the LEP center-of-mass energy was about 91 GeV, the mass of the Z boson. In order to investigate the properties of this boson the c.m. energy was varied with a few GeV. The cross section for the Z production varies strongly for these different c.m. energies while the cross section for the two-photon processes only varies slowly in this energy range.

In 1995 the c.m. energy was raised to about 133 GeV. This was the first step towards the second phase of the LEP facility which is to investigate W^+W^- pair production. At

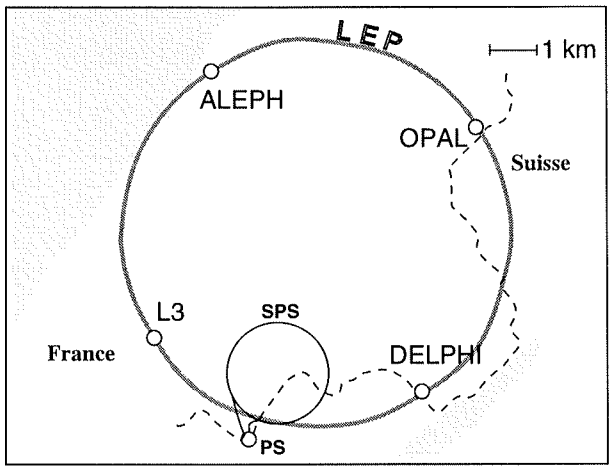

Figure 2.1: *The LEP ring and the four experiments*

these energies the cross section for the production of the Z becomes small while the cross sections for the two-photon processes increase w.r.t. the cross sections around 91 GeV.

2.2 The L3 detector

The L3 detector has been widely discussed. For a complete description of the detector see [40]. The different upgrades are discussed in [41–43]. A summary of the detector is given in this chapter.

In figure 2.2 a perspective view is shown of the L3 experiment. The coordinate system as applied in this thesis is as follows. The center of the detector, the interaction point, is the center of the coordinate system. The positive z-axis is in the direction of the beam pipe, pointing in the same direction as the electron beam. The positive y-axis points upwards and the positive x-axis is then defined for a right-handed system. The x-axis points to the middle of the LEP ring. The polar angle θ is taken with respect to the positive z-axis. The azimuthal angle ϕ is taken in the plane perpendicular to the z-axis with respect to the positive x-axis turning counterclockwise.

In the following subsections a short description of all the subdetectors is given.

2.2.1 Silicon microvertex detector

The innermost part of the L3 detector is the silicon microvertex detector (SMD). The SMD consists of two concentrical layers of silicon detectors, placed at 6 and 8 cm from the interaction region. The polar-angle coverage runs from 22° to 158°. Each layer provides a two-dimensional position measurement (through a double-sided readout of the strips), with a precision of 8 and 12 μm in the direction perpendicular and parallel to the beam

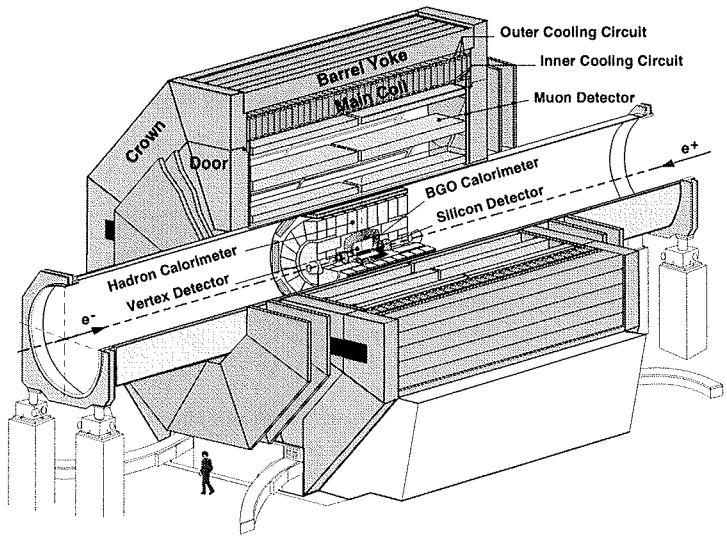

Figure 2.2: *The L3 experiment, the large scale of the experiment is illustrated by the figure on the foreground.*

direction, respectively. A front view of the layers is shown in figure 2.3 together with the track reconstruction.

2.2.2 Central tracking chamber

The next inner part of the L3 detector is the tracker, the Time Expansion Chamber (TEC). This tracker consists of an inner tube with a radius of 9 cm and an outer tube with a radius of 46 cm. Its sensitive length along the beam pipe is 98 cm. The detector is divided into two chambers. In the ϕ direction the inner chamber is divided into 12 sectors, each sector contains 8 anode wires. The outer chamber is divided into 24 sectors which contain 54 anode wires each, in figure 2.4 one inner sector and a piece of two outer sectors with 8 sense wires is shown.

When a charged particle passes through the TEC, electrons are generated through ionisation of the gas. These electrons drift towards the plane of the anode wires in a homogeneous field of 0.9 kV/cm. The anode wires themselves are kept at a nominal voltage of 2.9 kV.

Close to the anode plane is a plane of grid wires which are held on ground level. These ensure on the one hand the homogeneity of the drift region and on the other hand a high gas amplification in the region between the grid plane and the anode plane (see figure 2.4).

A wire is hit when a group of electron signals are above a certain threshold. After conversion of the measured drift time into a drift distance, a left and right ambiguity still remains with respect to the anode plane. This ambiguity can usually be resolved by combining hits from other anode wires into a track. Also, 14 groups of 5 grid wires are

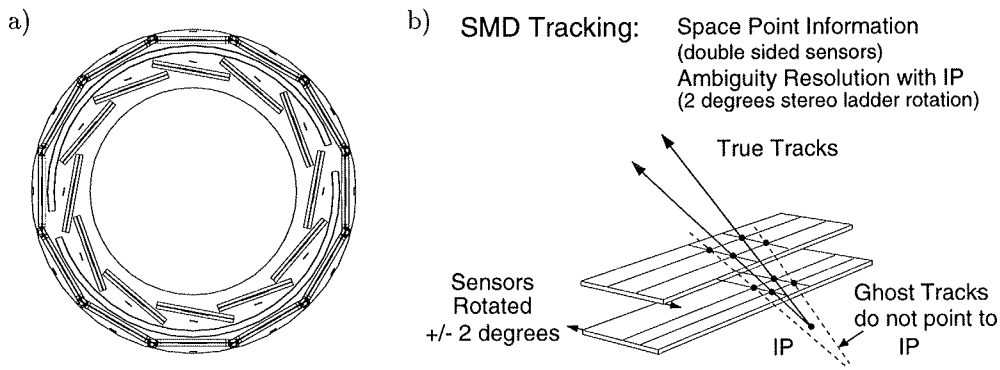

Figure 2.3: *The SMD: (a) front view of the SMD, which shows the stacking of the two layers and (b) the track reconstruction with the help of the two layers.*

read out in each grid plane of each outer sector.

Each inner sector has 2, and each outer sector has 9 charged division wires. These wires are read out at both ends of the detector. The pulse heights at each end yield information about the z-coordinate of the hit. Because this information is rather poor, the z-coordinate of the track is also measured with z-chambers. These consist of two cylindrical proportional chambers, each with two layers of cathode strip readout. Both chambers contain one layer of z measuring strips and one layer of strips which have an angle of 70.1° with respect to the beam pipe. The polar angle of the z-chambers ranges from $45° < \theta < 135°$.

2.2.3 Electro-magnetic calorimeter

The electromagnetic calorimeter (ECAL) is made out of Bismuth Germanate, $Bi_4Ge_3O_{12}$ (BGO), crystals. These crystals are used as showering and detection media. The total energy of electrons, positrons and photons is absorbed in this medium. The radiation length for this material is very short ($X_0 = 1.12$ cm). Owing to this short radiation length the calorimeter is very compact. The crystals are 24 cm long, the front face is 2×2 cm^2 and the end face is 3×3 cm^2. Each crystal is mounted in a carbon-fiber support structure, this reduces the amount of stress on the crystals, this stress can destroy the properties of the crystals.

The calorimeter consists out of four parts. The barrel part is made out of two cylindrical half-barrels, each holding 24 rings of 160 crystals. The two endcaps have 1536 crystals divided into 16 sections in the azimuthal angle ϕ. The two barrel parts have an polar angle coverage from 42° to 138°. The two endcaps extend this coverage from 12° to 35° and from 145° to 168°, this detector is denoted BGO in figure 2.5.

The crystals are positioned in such a way that they point to the interaction point in θ and that they are tilted 6° in ϕ, this to reduce the possibility for a particle not to be detected by the calorimeter.

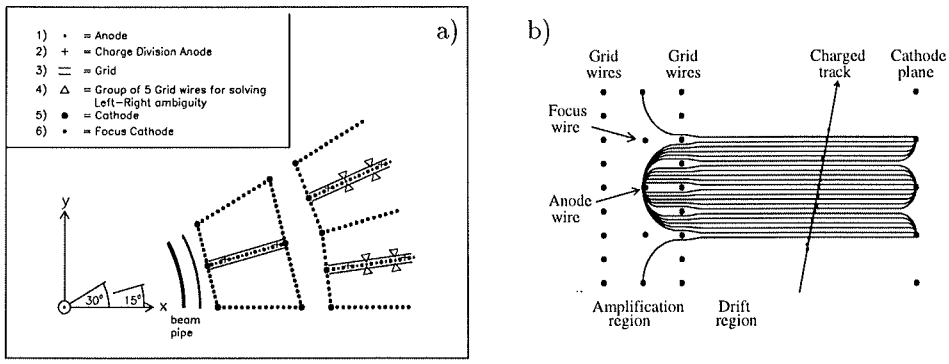

Figure 2.4: *The TEC: (a) a schematic view of the inner part of the TEC, showing one inner sector and the inner part of two outer sectors, also different kinds of sense wires are indicated and (b) an illustration of the field lines in the TEC, if the anode wire is an LR wire the 10 grid wires closest to the anode wire solve the left-right ambiguity of the hits.*

Before a good measurement of the energy can be performed, several factors much be taken into account. First, the amount of light produced by a crystal is temperature dependent. Therefore, every twelfth crystal is equipped with a temperature sensor which is read out every 1000 seconds. The amount of light depends on the distance between the energy deposit and the photo-diode. Also aging and radiation damage can give a variation in the amount of light produced. These effects are monitored by measuring the response of the crystals to the light produced by Xenon flash lamps. The energy measured must be corrected for the energy losses due to the finite length of the crystals and the cracks between the crystals, this depends on the impact point on the crystal. The losses are larger when this impact point is nearer to the edge of a crystal. After all the corrections are taken into account, the energy precision can be parameterised by [44]:

$$\frac{\sigma(E)}{E} = \sqrt{\left(\sqrt{\frac{2.37}{E}} + 0.38\right)^2 + 1.18^2 + \left(\frac{0.25}{E}\right)^2}\,\%. \tag{2.1}$$

The energy E is given in GeV. The first two terms are due to the intrinsic shower fluctuations and inhomogeneities in both the material and the light collection. The third term is due to the uncertainty in the leakage and calibration constants, and the last term is due to correlated noise.

2.2.4 Hadron calorimeter

The hadron calorimeter (HCAL) is placed just outside the electromagnetic calorimeter. It consists of uranium as an absorber material and wire chambers as a sampling medium.

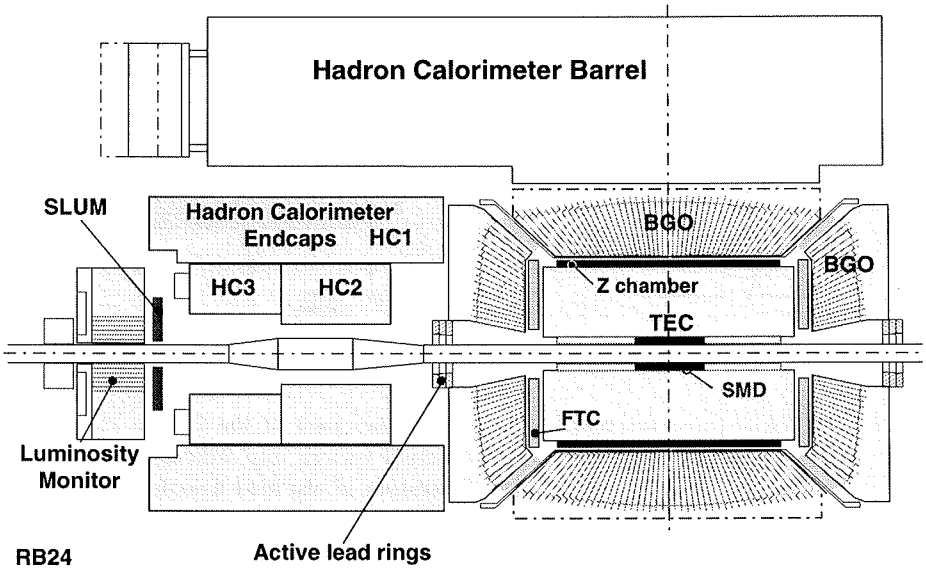

Figure 2.5: *The L3 inner detectors, all these detectors are placed inside the support tube.*

The angular coverage is 99.5 % of the full solid angle. The energy precision as measured in hadron test beams [45] is:

$$\frac{\sigma(E)}{E} = \frac{55}{\sqrt{E}} + 5\%. \tag{2.2}$$

Here, the energy, E, is again given in GeV.

The barrel region covers a polar-angle range from 35° to 145°. It consists of 9 rings each containing 16 modules. The outer radius is 1975 mm. The middle three rings have an inner radius of 885 mm, the other rings have an inner radius of 979 mm. These nine rings have a total length of 4725 mm. All modules are built up from alternating layers of 5-mm thick plates of depleted uranium and layers of proportional wire chambers. These wire chambers are alternately along the z-direction and the ϕ-direction in order to improve spatial information. A 54-mm thick stainless-steel plate shields the photodiodes of the BGO from the uranium radioactivity.

The two endcaps cover a polar-angle range from 5.5° to 35° and from 145° to 174.5°. The endcaps are divided into three rings. These rings are split into two half-rings, which allows the inner detectors to be accessed. The wires in successive layers are rotated over 22.5° with respect to one another. The readout is arranged in towers such that each tower points towards the interaction point in the θ-direction. In figure 2.5 the barrel and the three rings of the endcaps are shown.

One more nuclear absorption length for hadrons is added to the hadron calorimeter through the muon filter, eight octants situated just inside the support tube. The purpose of this muon filter is to reduce the punch-through of hadrons into the muon chambers. Each octant consists of brass absorber plates with 5 layers of proportional wire chambers.

2.2.5 Active lead ring

At 104 cm from the interaction point a third calorimeter is placed. It consists of layers of lead and layers of scintillator material (ALR). This detector started as a shield for the TEC, to protect it against beam backgrounds. To ensure that the high precision measurement of luminosity was not compromised through shadowing of the luminosity monitor by the ALR, a small gap exists between the two detectors.

2.2.6 Luminosity monitor

For the measurement of the delivered luminosity by LEP to L3 two forward calorimeters are installed at 2.8 m, at both sides of the interaction point. The polar-angle coverage ranges from 25 mrad to 69 mrad. The two calorimeters consist of BGO crystals of 26 cm length, the front face varies between 1.5×1.5 and 1.5×3 cm^2. Each calorimeter has 304 crystals in total. To protect the two calorimeters against radiation damage during the fill and acceleration of LEP the two calorimeters consist of two halves. This enables the detectors to be opened during the fill and acceleration of the beams.

The luminosity measurement is done with the help of small-angle Bhabha events, thus

$$\mathcal{L}_{\mathrm{ee}} = \int L dt = \frac{N_{Bhabha}}{\sigma_{Bhabha}}. \tag{2.3}$$

Here, $\mathcal{L}_{\mathrm{ee}}$ is the time-integrated luminosity, L the luminosity, N_{Bhabha} the number of Bhabha events and σ_{Bhabha} the theoretical cross section. Because the cross section depends strongly on the fiducial volume the definition of this volume is a crucial factor in the determination of the luminosity. To improve the definition of this fiducial volume a silicon tracker with a high precision geometry was installed in front of each calorimeter. Each tracker consists of two R-measuring layers and one ϕ-measuring layer. In figure 2.5 one side of the luminosity monitor is shown, the shape of the beam pipe is chosen such that the amount of material is minimised for electrons scattered into the luminosity monitor. On the other side this was not possible because of the access required to the SMD.

2.2.7 Muon chambers

The muon spectrometer measures the muon momenta with a three-layer configuration. For muons which have a polar angle between 44° and 136° the momenta are measured in the three layers of the barrel spectrometer. For muons with polar angles between 36° and 44° and between 136° and 142° the momenta are measured with two layers of the barrel spectrometer and with one layer of the forward-backward spectrometer. When the polar angle becomes even more forward, down to 24° or 156° the momenta are measured with the three layers of the forward-backward spectrometer. In figure 2.6 a schematic view of

the muon spectrometer is shown with the three different regions for the measurement of the muon momenta and the corresponding angles.

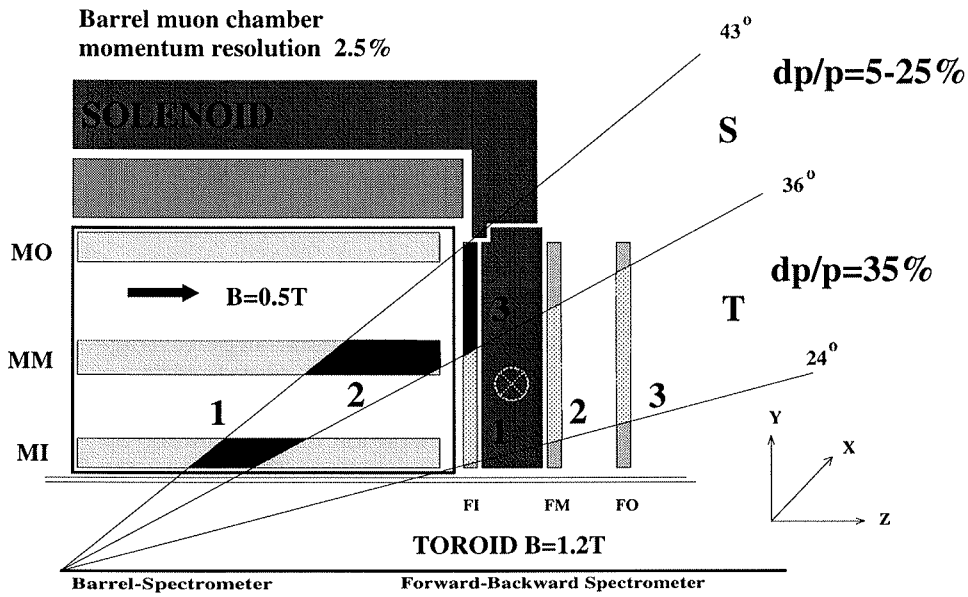

Figure 2.6: *Schematic view of the barrel and forward-backward muon spectrometers.*

Barrel spectrometer

The barrel spectrometer is situated between the support tube and the magnet coil, and is thus inside the solenoid field of 0.5 T. The spectrometer consist of two ferris wheels along the z-axis. Each ferris wheel has eight octants. These octants consist of 5 precision drift chambers, one chamber in the inner layer, two chambers in the middle layer and two chambers in the outer layer.

The P-chambers, with sense wires along the z-axis, provide measurements in the $R-\phi$ plane (p_t and ϕ of the track). The inner and outer chambers have 16 wires while the middle chambers have 24. Because the momentum is determined from the measurement of the sagitta, see figure 2.7, the alignment of the five chambers with respect to one another is very important. Four Rasnik systems and a laser beacon system are used for this purpose.

In the top and bottom covers of the outer and inner chambers also wires normal to the beam exist, the Z-chambers. They give information about the polar angle of the track.

The precision of the momentum of tracks with three segments in the barrel is 2.5 %,

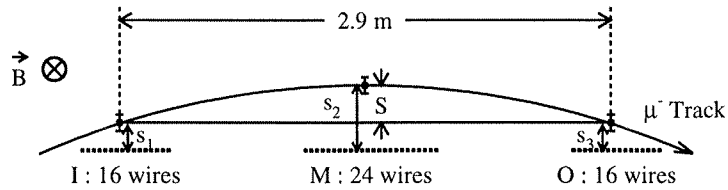

Figure 2.7: *The measurement of the sagitta, the uncertainty on the sagitta is more sensitive to the uncertainty in point s_2 than to the uncertainties in point s_1 or s_3.*

when only the two inner layers are used the precision diminishes to about 20 %. But when the information from the two inner barrel layers is combined with the information of the inner forward chamber the precision can improve to about 5 % for tracks with a polar angle around 43° and then diminishes again to 20 % for polar angles around 36°.

Forward spectrometer

The forward spectrometer is positioned on the magnet doors. One layer, the inner layer is inside the magnet, the other two layers are outside. Four octants are attached on each door, each octant consists of two half octants (called left and right). Each of these half octants is constructed from 3 precision drift chambers. For the measurement of the muon momentum the track of the muon is bent by the field inside the magnet door. This field has two components. The first component is the returning flux of the solenoid field inside the door. The second component results from the coils wrapped around the doors to set up a toroid field of 1.2 T.

For the alignment of the inner forward chamber with respect to the barrel spectrometer so-called 'proximity sensors' are used. These sensors measure the distance to reference surfaces glued on the inner forward chambers, whose positions with respect to the barrel wires have been determined. Six of these distance measurements give a full description of the position of the forward inner chamber in space. For the alignment of the three forward chambers with respect to one another two modified RASNIK systems are used.

The momentum precision of a track going through the three layers of the forward spectrometer is about 35 %, this is due to the multiple scattering of the muon in the one-meter wide iron magnet door.

2.3 Triggers

2.3.1 Level 1 trigger

The level 1 trigger is a logical OR from different subtriggers.

The barrel muon trigger: first the number of hits is counted in each chamber and compared with a preset threshold. Then a decision is made on the presence of a track

segment. Followed by a decision on the presence of a track by looking at predefined "roads". Three conditions give a trigger. The first is the di-muon trigger, when two tracks (a track has at least two segments) have an a-coplanarity of less than 90°. The second is the single muon trigger, at least one track (a track now has three P segments) is found in one octant. And the last is the small-angle muon trigger, two tracks (a track now is a segment in the inner chamber in coincidence with both layers of the inner Z-chambers) are found in two back-to-back octants.

The beam-gate trigger: every ten seconds, in coincidence with a beam crossing, one event is triggered in order to obtain an unbiased sample.

The scintillator trigger: this trigger requires 5 out of the 30 scintillators fired within 10 ns of the beam crossing, and two of the fired scintillators should be separated by more than 45° in ϕ.

The TEC trigger: the TEC trigger considers the 14 LR wires of each outer sector, the LR ambiguity of each hit is solved. Each outer sector is divided in two halves. A further division in two of each half sector is made by considering the drift time of the hits, which gives four ϕ bins for each outer sector. So in total 96 ϕ bins exist with each a maximum of 14 hits. On the 96×14 matrix a track search is performed on predefined "roads", taking into account possible inefficiencies (by looking at pairs of hits as well) and spurious tracks (taking into account the possibility of additional hits). A track has at least 12 wires hit out of the possible 14, or 6 pairs out of the possible 7 in the barrel region, with the polar angle between 42° and 138°. In this region a track with a $P_t > 600$ MeV is contained in one ϕ bin, tracks with a P_t down to 150 MeV can go through up to 3 ϕ bins. The search for small-angle tracks, with a polar angle between 25° and 155°, is done with the help of the seven innermost wires. The minimum P_t is here 100 MeV. The trigger requires two tracks with an a-coplanarity smaller than 43° (if a track is found in a certain ϕ bin the other track should lie in the bin directly opposite or in one of the eleven bins on either side of the opposite bin).

The energy trigger: the signals from the calorimeters are grouped together to obtain signals (channels) for the energy trigger,see 2.8. Thirty BGO crystals form one group. This gives 32 azimuthal and 8 polar segments, a total of 256 channels. The endcaps yield another 256 channels. The hadron calorimeter is divided into a front part (A) and a back part (B). Part A is within one interaction length and part B goes beyond. The front part has 11 θ segments and the back part has 13 segments. All HCAL segments are divided into 16 ϕ bins, this gives 384 HCAL trigger channels. Each side of the luminosity monitor is divided into 16 ϕ bins, another 16 channels. Again different algorithms are applied to give a trigger. The single photon algorithm requires a single electromagnetic cluster in the barrel BGO, by demanding that at least 80 % of the deposited energy is contained in one cluster. The lumi trigger has three different requirements. The single-tag requirement needs at least 30 GeV on one side of the lumi detector. The double tag asks for a minimum of 25 GeV on one side and a minimum of 5 GeV on the other side. The back-to-back requirement asks for at least 15 GeV on each side, and the azimuthal difference of the two clusters has to be 180° within two sectors. The single-electron algorithm requires a single-tag trigger in coincidence with a track found by the TEC-trigger hardware. The total-energy algorithm again consists of different requirements. The first one is that the total energy in the calorimeters is at least 25 GeV. The second one needs at least 15 GeV in

the BGO, and the last one requires at least 8 GeV in the barrel BGO. A cluster algorithm needs at least 6 GeV in one cluster, a cluster is defined as an energy deposit for channels in different layers (BGO, A or B) with the same θ and ϕ. When a cluster matches in ϕ with a track the energy threshold is lowered to 2.5 GeV.

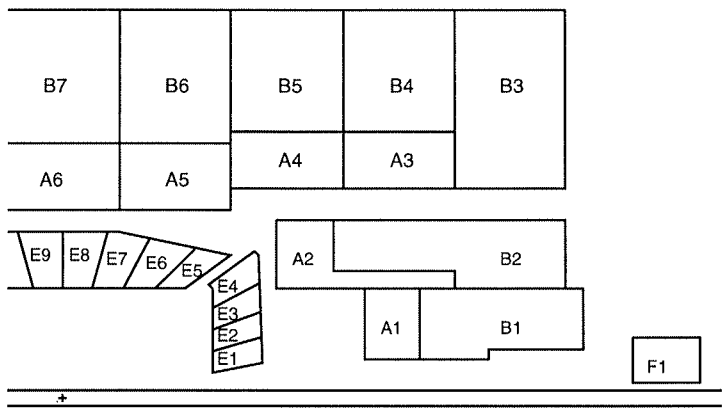

Figure 2.8: *The different trigger channels for the BGO, HCAL and Luminosity monitor.*

2.3.2 Level 2 and 3 triggers

The same information that is needed for level 1 is used for the level-2 trigger, but since more time is available more complex algorithms can be applied. The aim of this trigger is to reduce known background events (beam-gas, beam-wall and electronic noise events). Events which have more than one level-1 trigger always pass this level. Of every 10 events, one event is kept to monitor the efficiency.

The final online reduction results from the level 3 trigger. Because this trigger has even more time to analyse events the full digitisation of the event is used in addition to the level-1 and level-2 information. The final rate of events written to tape is now reduced to a few Hz.

2.4 Event reconstruction

The event reconstruction takes place in three steps. First the information in each subdetector is grouped into primitive clusters. Then these objects are used to reconstruct the particles/clusters of the event. And finally these clusters can be grouped to form jets, or as is the case here the visible mass is reconstructed.

2.4.1 Primitive clusters

The tracks in the TEC are reconstructed in two steps due to the poor z-information of the hits. In the first step the hits are grouped into tracks in the $r\phi$-plane projection of the hits. In this step the ϕ and the distance of closest approach (DCA is the minimal distance between the nominal vertex and the track in the $r\phi$ plane) are constructed. The second step attemps to reconstruct the θ for each track found in the first step with the information from the charge division wires and Z-chamber hits.

In the electromagnetic calorimeter the energy deposits of adjacent crystals are grouped into bumps, each bump corresponds to a local maximum and, in principle, to one particle. Sometimes during the clustering of adjacent crystals the cluster has to be split into two bumps when two or more particles are so close that they form one (deformed) cluster.

The reconstruction in the hadron calorimeter is more complex than for the electromagnetic calorimeter because the hits are deposited three-dimensionally. In the barrel, hits are first grouped within one module. Then groups of hits in adjoining modules are merged when they are nearby, to give the cluster. For the endcaps the grouping is done directly for the hits to give the cluster.

In the muon chambers the hits are first grouped within one P or Z chamber. These segments are matched with each other in one octant, this gives the muon-chamber tracks.

2.4.2 Smallest resolvable clusters

The objects mentioned in the previous subsection are used to obtain the smallest resolvable clusters (SRC's). This is achieved by correlating the clusters found in the electromagnetic calorimeter with the clusters in the hadron calorimeter. The energy of these clusters are scaled to account for shower fluctuations, gaps and other inefficiencies. These scaling factors are called G-factors and depend on the type of particle (electromagnetic or hadronic) and on the subregion of occurence (the detector is divided into nine such regions).

The G-factors for the data are determined by minimising the difference between the visible energy and the center-of-mass energy. For the Monte Carlo samples the minimisation is performed by comparing their deposited energies with those of the data.

The electromagnetic G-factors are determined from Bhabha events and the hadronic G-factors from di-jet hadron events.

2.4.3 Visible mass

The visible mass is reconstructed with the energy vectors of all the SRC's. Also the energy and momentum measured in the muon chambers are taken into account. The clusters in the active lead ring are not included in the reconstruction due to the changes made to the ALR between the 1994 and 1995 run. This is shown in figure 2.9. More clusters exist for the 1995 data taking than for the other years and even when the distribution is scaled down more clusters below five GeV are found in the 1995 data, and also the clusters of about 46 GeV (final state electrons and positrons) are not observed in the other years.

The energy in the luminosity monitor is taken into account by selecting the clusters which have less than 10 GeV reconstructed energy. The energy distribution for the luminosity clusters is shown in figure 2.10. The distributions agree fairly well for the lower

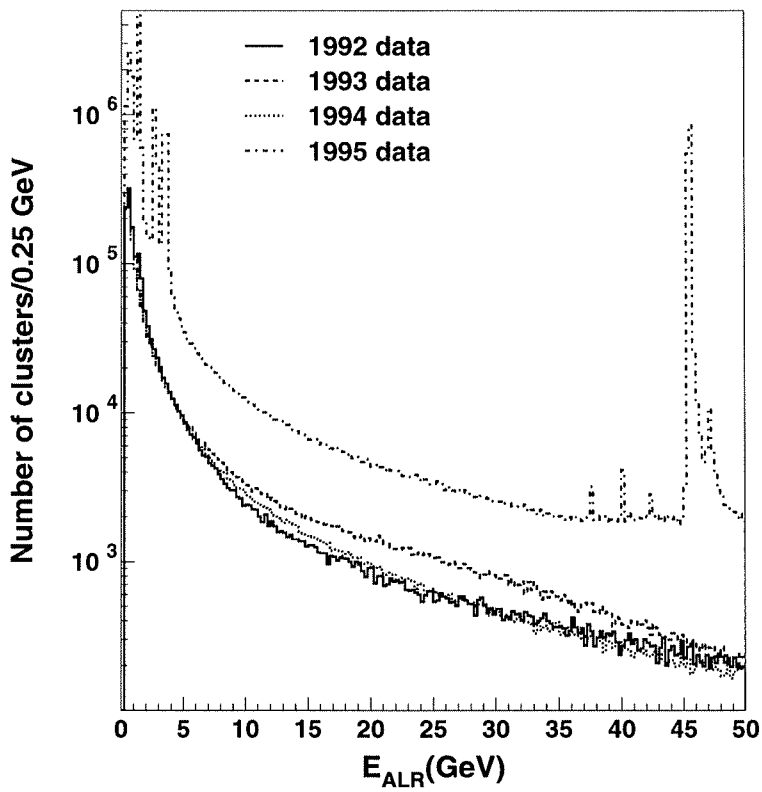

Figure 2.9: *The energy of the clusters in the active lead ring (scaled with a factor 77) for all events for the different years.*

part and the higher part of the spectrum. The clusters around 46 GeV are the tags. The clusters with energies around 35 GeV are the off-momentum electrons/positrons. These beam particles have less energy and are therefore not focussed correctly. Their trajectories are such that they can hit the luminosity monitor and thus mask a low-energy tag. For the 1992 data these off-momentum electrons/positrons have energies down to 15 GeV. The clusters with less than 10 GeV can come from low-energetic electromagnetic particles but hadronic particles can leave a low-energetic cluster even when they have high energies bacause the luminosity monitor is an electromagnetic calorimeter and will in general not absorb the full energy of a hadronic particle.

Due to the particles (like the clusters in the ALR) which are not used, and particles which do not enter the detector at all but are lost down the beam pipe, the visible mass is, in general, smaller than the true mass. The correlation between visible and true mass is too complex to give an event-by-event correction. Thus the true-mass distribution is distorted and can not be measured directly but rather needs to be reconstructed from the visible-mass distribution. This is done with the help of unfolding techniques.

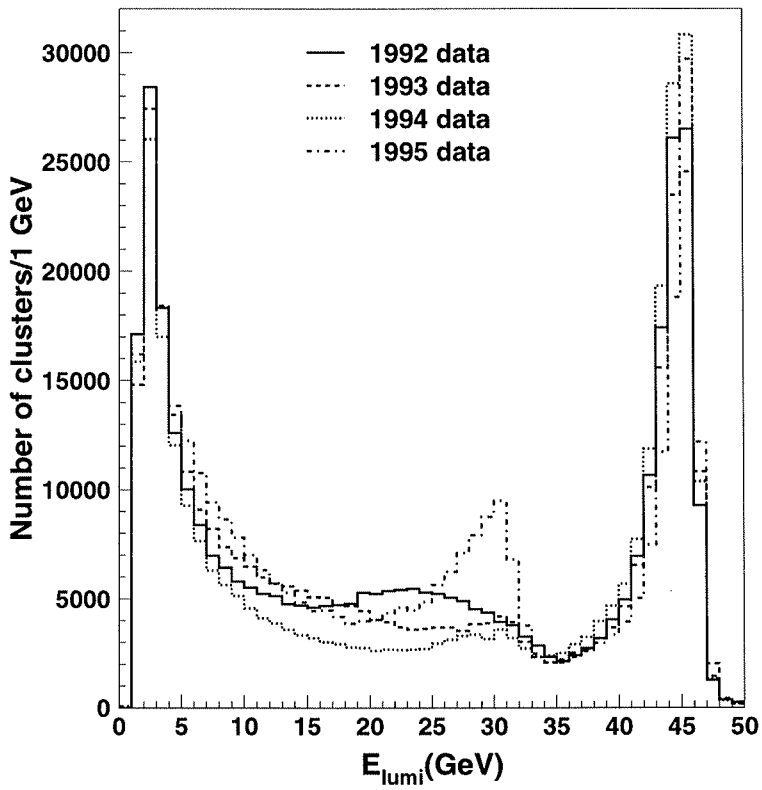

Figure 2.10: *The energy of the clusters in the luminosity monitor for all events for the different years.*

2.5 Event simulation

The MC samples need to be treated in the same manner as the data if a comparison is made between the distributions found in the data and those in the MC samples. The generators have as an output the type of the final state particles, their momenta and their positions (decay products can originate away from the vertex when the lifetime of the parent particle is long).

The detector is simulated with the GEANT package [46], version 3.15. This package allows for a detailed description of the geometry of each subdetector. Also the materials applied are taken into account, to allow for the best possible description of the interactions between the particles and the detector material.

The electro-magnetic interactions are well understood. And the electro-magnetic showers in the ECAL simulation are limited by the computing time. This implies that a cut-off on the energy of the particles is made below which the interactions of the showering particles are treated collectively. The broad range of hadronic interactions complicates the

hadronic shower simulation. Some of the cross sections are poorly known and are described with the parametrisations of the GEISHA package [47]. The parameters were tuned with the test-beam results [40].

2.5.1 Detector noise

HCAL noise at 90 GeV

The selection efficiency plays an important role in the measurement of the total cross section. This efficiency is calculated from simulated events; therefore the simulation should describe all detector effects, including noise, as well as possible to obtain a reliable efficiency. The simulated events do not have all this noise included during the simulation of the detector response. For this reason these effects are included during the analysis.

Investigation of the beam-gate events (these are events which are read-out once every 10 seconds during a beam crossing) give information about the noise in each subdetector. Most of these events will not be triggered by any of the other triggers and the probability that a genuine event is taken into account, is thus very small.

In the Hadron Calorimeter more low-energetic HCAL clusters exist in the data than in the Monte Carlo (compare the full dots with the solid line in figure 2.11). These are noise clusters originating from the decay of the uranium in the HCAL. The clusters found in the barrel in the beam-gate events (dashed line in figure 2.11) give a similar energy spectrum as the surplus of the data with respect to the simulation (open dots in figure 2.11). For 45 % of the simulated events one extra HCAL cluster is added to the event with an hadronic energy distribution and polar-angle distribution similar to the distributions of the clusters in the beam-gate events.

In the BGO the low energetic clusters have so low an energy that they are not recognised as good clusters (energy higher than 50 MeV). So these clusters are not included in the simulation.

HCAL excess in the MC at 133 GeV

A problem with the MC, made for the 133 GeV data, was encountered at the HCAL energy distribution of all clusters. Opposite to the problem for the MC sample at 90 GeV, in this MC sample too many clusters are found in the barrel with an energy higher than 1.4 GeV. About two thirds of these clusters were removed on a statistical basis. After this rejection all distributions affected were improved, not only as concerns the total hadronic energy but also the mass, the longitudinal and the transverse energy imbalance. In figure 2.12 the excess at energies higher than 1.4 GeV is plotted.

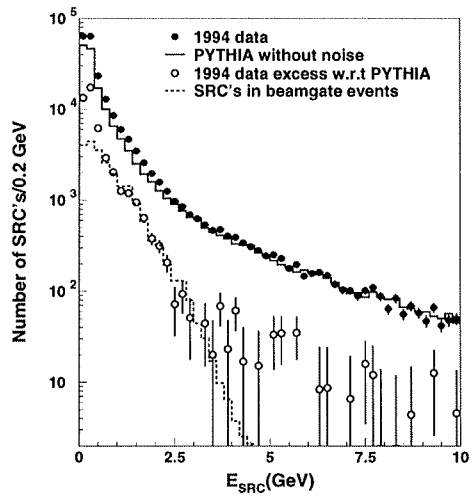

Figure 2.11: *The cluster-energy distribution, the full dots give the data, the full line gives the sum of all MC samples. The difference between data and MC is plotted with the open dots, the dashed line gives the cluster-energy distribution for the clusters in beam-gate events.*

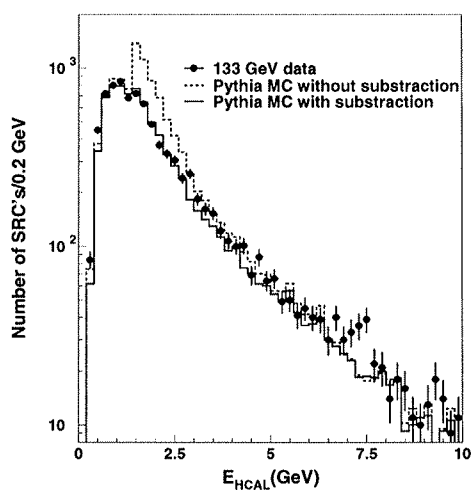

Figure 2.12: *The plot shows the large excess in the number of clusters with an HCAL energy larger than 1.4 GeV in the MC.*

3

Untagged data

In this chapter the measurement of the untagged total two-photon cross section as a function of the two-photon mass is described for two sets of LEP energies. The first set is taken around the Z pole; it has a large background from this pole but the integrated luminosity is very large, even after the selection criteria are applied a large sample is left. The second set is taken around 133 GeV. Here the background is much smaller but so is the integrated luminosity. For both samples the visible mass distributions are unfolded, correlating the visible-mass spectra to the true-mass spectra. The different contributions to the systematical uncertainties are given. The mass dependence is fitted and compared with the two models mentioned in chapter 2 and finally conclusions are drawn.

3.1 Data taken around the Z pole

The selection criteria are discussed in view of the background. After the selection the selected data sample is compared to the MC sample to check the data integrity.

3.1.1 Data selection

Untagged hadronic two-photon events have no clear signature; events from Z decay, into a quark-antiquark pair [48,49] or a $\tau^+\tau^-$ pair [50,51], or events from two-photon $\tau^+\tau^-$ pair production can pass for a hadronic two-photon event. However, the hadronic two-photon process has characteristics which distinguish it from these other processes and make a selection procedure possible. The distinction is incomplete and the remainder from the competing processes in the selected sample is treated as background. In order to estimate the background found in our sample, generated Monte-Carlo events are used for known back-ground event types. The total cross sections for the decay of the Z into a quark-antiquark pair [48,49] or a tau pair [50,51] have been measured by L3 and depend strongly on the beam energy. The the two-photon tau-pair production is a QED process and can be calculated. The cross section has been measured by L3 as well [52].

In addition so-called beam-gas events and beam-wall events occur in the sample. These types of events have not been simulated by a Monte-Carlo generator and thus must be

estimated from the data itself.

In order to reduce these background events eight variables are used to select the events:

- The normalised longitudinal energy imbalance.
- The transverse energy imbalance.
- The number of good tracks.
- The ratio of the number of good tracks to by the total number of tracks.
- The energy in the hadron calorimeter.
- The corrected missing energy.
- The event vertex.
- The TEC trigger preselection.

Longitudinal energy imbalance

One feature of the two-photon events which differentiates them from events originating from the Z decay, is the longitudinal energy imbalance. This imbalance is measured as follows:

$$E_{\text{lon.imb.}} = \sum_{i=1}^{\text{all clusters}} E_i \cos\theta_i ,$$

with E_i the energy and θ_i the polar angle of the cluster. The two colliding photons generally do not posses longitudinal momenta of the same magnitude. Thus in general the two-photon center-of-mass system will have a momentum along this direction. For the Z boson decaying into a $q\bar{q}$ pair the longitudinal energy will in general be balanced, only detector inefficiencies (and sometimes initial-state photon radiation along the beam direction) will give an energy imbalance. This may be due to the precision of the energy measurement, which gives a deviation between the energy measured on the two sides of the detector, or due to the gaps in the detector, particles escaping from detection along the beam pipe or other gaps. For the decay of the Z boson into a $\tau^+\tau^-$ pair the center-of-mass energy can have a momentum along the longitudinal direction due to the two tau-neutrinos which escape from detection and hence introduce a longitudinal energy imbalance. Monte Carlo studies showed that this effect is small compared to the large imbalances in two-photon events. This selection criterion will not affect the background arising from the two-photon tau-pair production.

Since detector inefficiencies introduce a longitudinal energy imbalance for events coming from the decay of Z bosons (these events have a large amount of energy deposited in the detector and thus can have a significant energy imbalance), not the energy imbalance itself is chosen to select events but the normalised longitudinal energy imbalance. The normalisation is done with respect to the visible energy:

$$E'_{\text{lon.imb.}} = \frac{\sum_{i=1}^{\text{all clusters}} E_i \cos\theta_i}{\sum_{i=1}^{\text{all clusters}} E_i} .$$

In figure 3.1 the normalised longitudinal energy imbalance is shown. For two-photon selection the minimum absolute value for this normalised imbalance is set at 0.45. The Monte Carlo prediction is in good agreement with the data (also the large background coming from the Z decay for low values of this imbalance is described well).

Transverse energy imbalance

The polar angle of the two colliding photons has a typical bremsstrahlung spectrum, implying that the polar angles are typically small. Furthermore, the hadronic two-photon mass is on average much smaller than the Z mass, and the dominant two-photon production mechanisms, such as VDM and QPM, favour forward hadronic production. The transverse energy imbalance is thus small for a large part of the two-photon sample. If a Z boson decays into a $q\bar{q}$ pair and due to the detector inefficiencies the longitudinal energy imbalance is large, the transverse energy imbalance is expected to be large as well. The transverse energy imbalance is calculated as follows:

$$E_{\text{tra.imb.}} = \sum_{i=1}^{\text{all clusters}} E_i \sin\theta_i .$$

In figure 3.1 also the transverse energy imbalance is plotted. The selection requirement is 4 GeV or less. The MC prediction describes the measured distribution correctly. The background from Z events is seen at large values for the transverse energy imbalance.

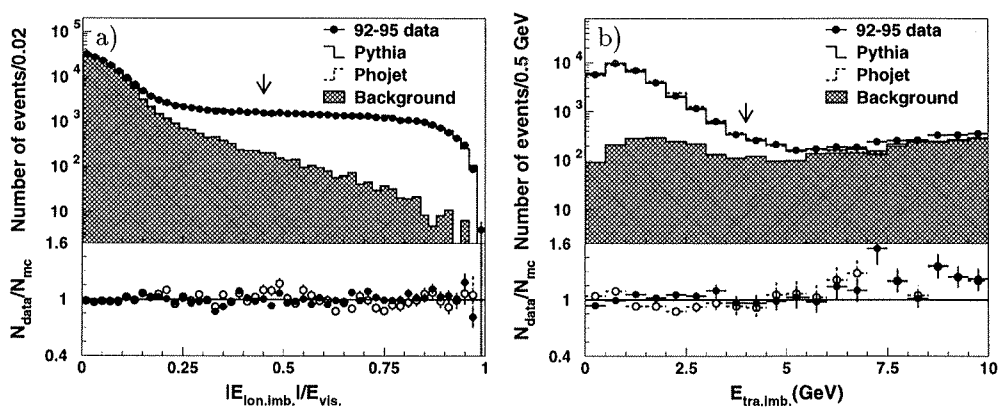

Figure 3.1: *The energy imbalance related selection variables; (a) the normalised longitudinal energy imbalance distribution and the division of the data by the sum of all Monte Carlo contributions, (b) the transverse energy imbalance distribution and the division of the data by the sum of all Monte Carlo contributions.*

Number of tracks

The previous two selection criteria mainly reduce the background coming from the decay of a Z boson into a $q\bar{q}$ pair. To reduce the fraction of events originating from the production of a $\tau^+\tau^-$ pair a minimum number of charged-particle tracks is required. As almost 80 % of the hadronic decay of a τ resides in one charged particle, more than 60 % of the tau-pair events can be removed by requiring more than two good tracks in the TEC. A good track is selected as follows:

- The transverse energy of the track, P^t_{track}, is larger than 100 MeV.
- The distance of closest approach in the x-y plane (DCA) to the nominal vertex is smaller than 10 mm.
- The number of hits, wires used for the track reconstruction, should be larger than 16.
- The number of hits used for the track divided by the span should be larger than 0.75. The span is the number of wires seen by the track from the first till the last hit.

In figure 3.2 the number of good tracks per event is plotted. At least 3 good tracks are required. This selection criterion also removes some additional backgrounds not mentioned before. These are di-muon and di-electron events (the two-track events not predicted by the Monte Carlo contribution) resulting from the decay of a Z boson, which had badly reconstructed energy or which had an extra (undetected) photon in the event. Here some differences between data and MC are visible. The number of three-track events in the MC samples deviates from the data but also the events which have a large number of good tracks are not described correctly by the PYTHIA sample, while the PHOJET sample shows nice agreement with the data.

Ratio of good over all tracks

Until now the selection criteria only reduced background coming from the decay of the Z boson and two-photon lepton-pair production. But also the beam-gas and beam-wall events have to be reduced. This is done by considering the number of good tracks divided by the number of all found tracks. A good track is defined as in the previous subsection. Especially beam-wall events have many tracks which originate from the beam wall or inner TEC wall (see figure 3.3). This implies that the DCA's of these tracks are large compared with the DCA's of tracks coming from the nominal vertex. Also a substantial number of these tracks have small momentum. Thus the number of good tracks divided by the number of all tracks will be small for these kind of events.

In figure 3.2 the ratio between the number of good tracks and the number of all tracks is plotted. The ratio for a good event must be at least 0.55. For small values of this ratio clearly more events are found in the data than in the MC, these are the beam-wall events not described by our MC samples.

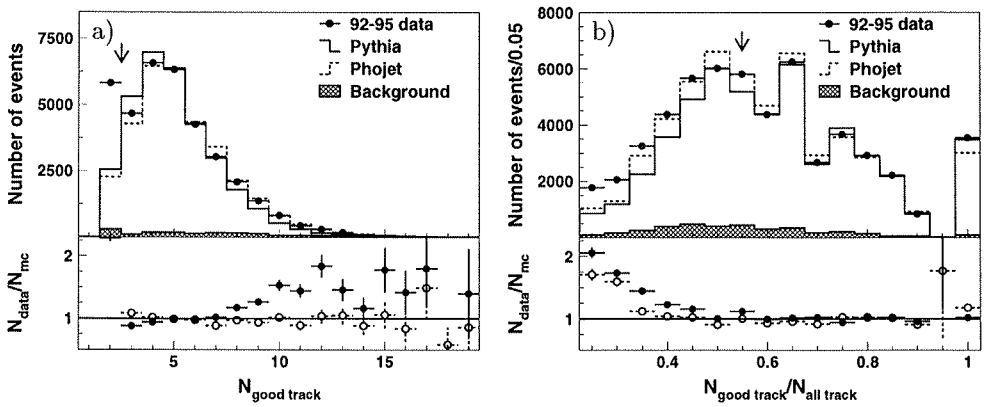

Figure 3.2: *The tracks-related selection criteria; (a) the number of good tracks found per event and the division of the data by the sum of all Monte Carlo contributions, (b) the ratio of good tracks over all found tracks and the division of the data by the sum of all Monte Carlo contributions.*

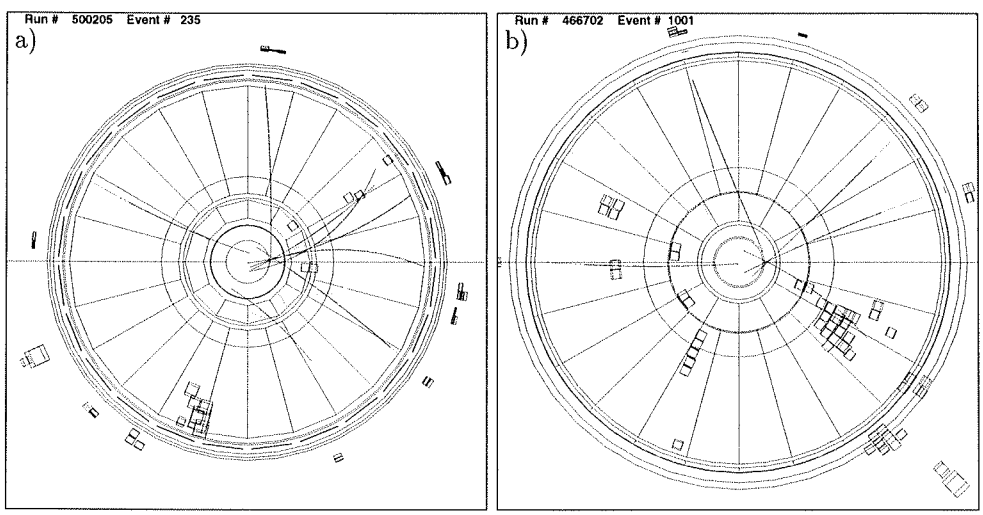

Figure 3.3: *Front view of two beam-wall events. The inner circle shows the position of the beam pipe. The lines indicate tracks found by the reconstruction software. In both events only one track passed the selection criteria for a good track.*

Hadron energy and missing energy selection

To ensure that the events found have hadronic activity, the energy deposited in the hadron calorimeter should be larger than 1.0 GeV. In figure 3.4 the hadron energy is plotted. The data contains more events with less than 1.0 GeV hadronic energy than the MC predicts. For the calculation of the systematical uncertainties this selection criterion is removed and the difference in cross section is taken into account as systematical uncertainties for this criterion.

The longitudinally corrected missing energy is calculated as follows:

$$E_{\text{missing}} = E_{\text{visible}} + |E_{\text{lon.imb.}}| - 2E_{\text{beam}}$$

The longitudinally corrected missing energy should be lower than -30 GeV. This selection criterion again removes events coming from the Z decay. If particles disappear down the beam pipe in a Z decay event, the missing energy in the longitudinal direction will be close to the total missing energy ($2E_{\text{beam}} - E_{\text{visible}}$). This selection removes events where the missing energy is close to the longitudinal energy imbalance. The distribution is shown in figure 3.4.

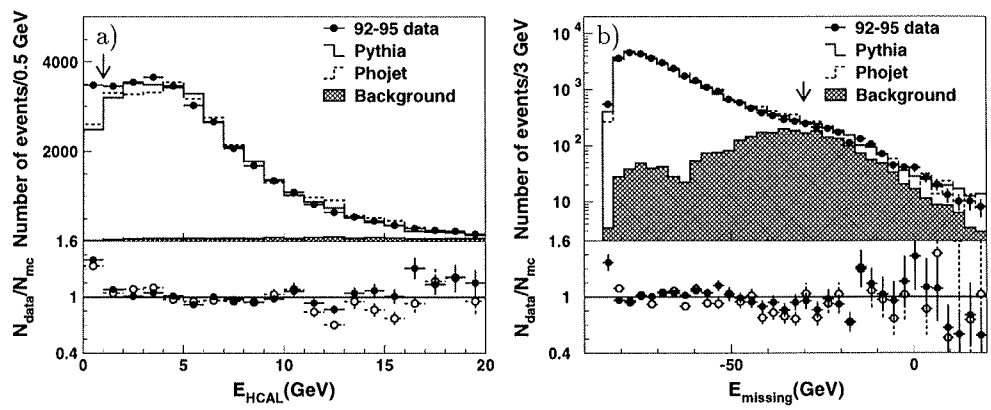

Figure 3.4: *Energy related selection criteria; (a) the energy deposited in the hadron calorimeter and the division of the data by the sum of all Monte Carlo contributions, (b) the longitudinal-corrected missing energy and the division of the data by the sum of all Monte Carlo contributions.*

Event vertex

Beam-gas events are collisions between a proton and a beam particle. When a 45 GeV beam particle collides with an almost momentumless proton the longitudinal momentum will be large and the transverse momentum will be small. If the collision takes place in the beam pipe in the L3 detector itself, it can generate more than 2 tracks which come from the center of the beam pipe and thus passes for a good two-photon event. One candidate

for a beam-gas event is shown in figure 3.5. In the front view the tracks seem to originate from the vertex, in the center of the beam pipe. But when the side view of the event is considered it is clear that the vertex position is shifted by several centimeters with respect to the nominal vertex (the dot in the center of the picture).

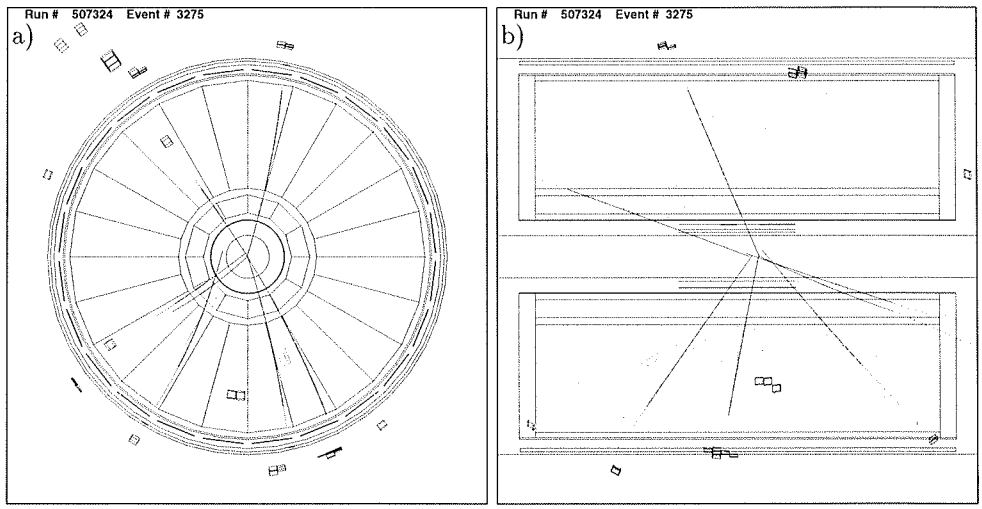

Figure 3.5: *A candidate for a beam-gas event: (a) the front view of the event and (b) a side view of the same event. The dot in the center of each figure shows the nominal vertex position.*

To reduce this background the longitudinal component of the event vertex is considered. Protons can evaporate out of the beam wall at any position along this direction. This implies that the vertex of such an event can be found all along the longitudinal axis, and thus not only around the nominal vertex. The longitudinal position of the event vertex is derived with a subroutine which uses information from most subdetectors. When the longitudinal component of the vertex is plotted (see figure 3.6) a small tail is seen (the relative hight of the tail differs per year). This tail can be used first to remove these beam-gas events and second to estimate the number of beam-gas events which are expected to be still in the sample. The line in the figure is a Gaussian fit to estimate the accuracy of the longitudinal-coordinate calculation with a flat beam-gas background (left and right hand tails are fitted independently). The standard deviation of the Gauss increases with increasin years, from 50 nb in 1992 to 80 nb in 1995.

The data starts to deviate from the Gaussian around 200 mm. Events that are more than 200 mm away from the nominal vertex are taken to be beam-gas events. The events between 200 and 350 mm are used to estimate the beam-gas background (the background is expected to be flat down to the nominal vertex). The fraction of beam-gas events expected in our sample is 1.4 %. (1.2 % for 1992, 0.9 % for 1993, 0.7 % for 1994 and 3.6 % for 1995).

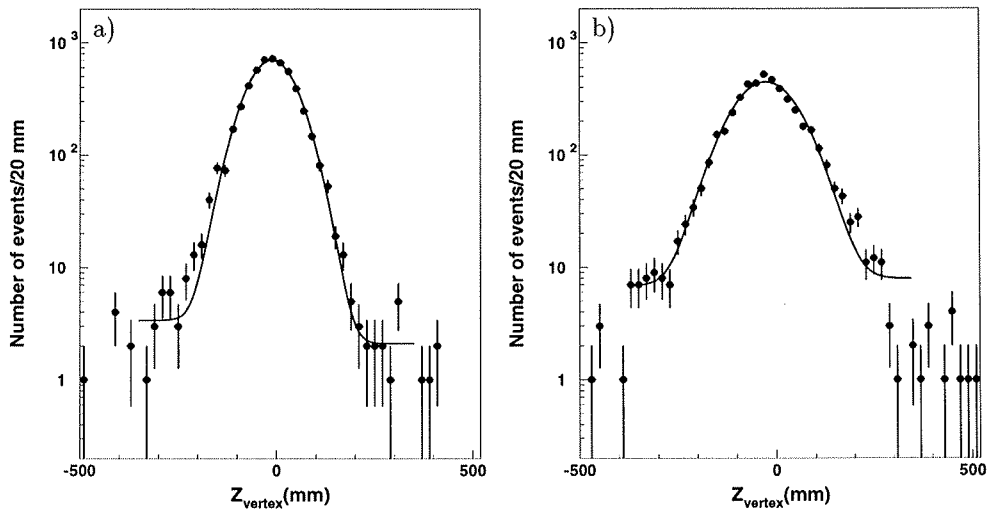

Figure 3.6: *The z-coordinate distribution: (a) 1993 data and (b) 1995 data. Events with a value larger than 200 mm from the nominal vertex are considered to be beam-gas events.*

TEC trigger selection

Events in the two-photon selection are required to be triggered by the TEC trigger. In general, the two-photon events are triggered by the TEC trigger and/or the energy trigger. When these triggers are independent, the trigger efficiencies can be calculated as a function of the visible mass from the data itself.

The trigger efficiencies are calculated from the data in the following way:

$$\begin{aligned} \epsilon^{\text{data}}_{\text{TEC trigger}} &= \frac{N_{\text{TEC+Energy trigger}}}{N_{\text{Energy trigger}}}, \\ \epsilon^{\text{data}}_{\text{Energy trigger}} &= \frac{N_{\text{TEC+Energy trigger}}}{N_{\text{TEC trigger}}}. \end{aligned} \tag{3.1}$$

Here, $N_{\text{TEC+Energy trigger}}$ is the number of events which are triggered by both the energy and the TEC trigger, $N_{\text{Energy trigger}}$ is the number of events which are triggered by the energy trigger and $N_{\text{TEC trigger}}$ is the number of events which are triggered by the TEC trigger. These efficiencies are shown in figure 3.7, the solid dots and squares.

As both triggers are inefficient for events in which most of the energy is deposited in the very forward direction it can be argued that they are not independent and that the TEC-trigger efficiency is over estimated. Alternatively the TEC-trigger efficiency can be calculated with the help of a TEC-trigger simulation. The MC is treated with a simple routine which describes the TEC-trigger track-finding efficiency for a track as a function of the polar angle and the transverse momentum. If two tracks are seen by the trigger

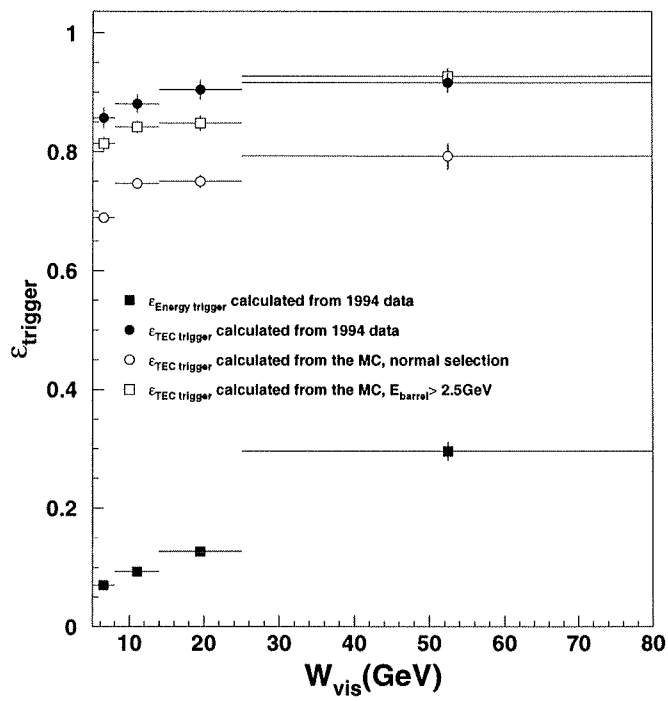

Figure 3.7: *The trigger efficiencies: the solid square is the energy trigger efficiency, the solid dot is the TEC trigger efficiency, both calculated from the data. The open dots give the trigger efficiency calculated from the PHOJET sample with the standard selection criteria. The open squares also come from the PHOJET sample but now at least 2.5 GeV reconstructed energy is required in the barrel region.*

with an a-collinearity angle smaller than $.27 \times \pi$ the MC event is triggered by the TEC. The TEC-trigger efficiency can be calculated for the MC as follows:

$$\epsilon^{\mathrm{MC}}_{\mathrm{TEC\ trigger}} = \frac{N_{\mathrm{selected\ and\ triggered}}}{N_{\mathrm{selected}}}.$$

Here, $N_{\mathrm{selected\ and\ triggered}}$ is the number of events selected and triggered by the simulation and N_{selected} is the number of events selected by the data. In figure 3.7 the open dots show this efficiency. A 15 % difference is found between this efficiency and the one obtained from the data. In order to verify that this difference relates to the assumption that the TEC trigger is indeed not independent from the energy trigger, this efficiency is calculated also for the events which have at least 2.5 GeV in the barrel region and thus with a fully efficient energy trigger, the open squares in figure 3.7. Now the efficiency for the data agrees better with the MC result. The TEC and energy trigger are thus not independent

and the TEC-trigger efficiency from the simulation is taken in the calculation of the cross sections. The systematical uncertainty due to the TEC trigger efficiency is taken to be half the difference between the results obtained with the data (solid circles in 3.7) and the simulation (open circles in 3.7).

3.1.2 Data integrity

In this section some variables are plotted in order to check wether the selected events are described correctly by the data. These variables come from two sources, the tracks and the clusters. For each track the reconstructed momentum is plotted and for each cluster the reconstructed cluster energy (see figure 3.8). A small excess in the total number of tracks exists in the data due to the excess of events with a large number of good tracks. But both distributions are described well by the MC.

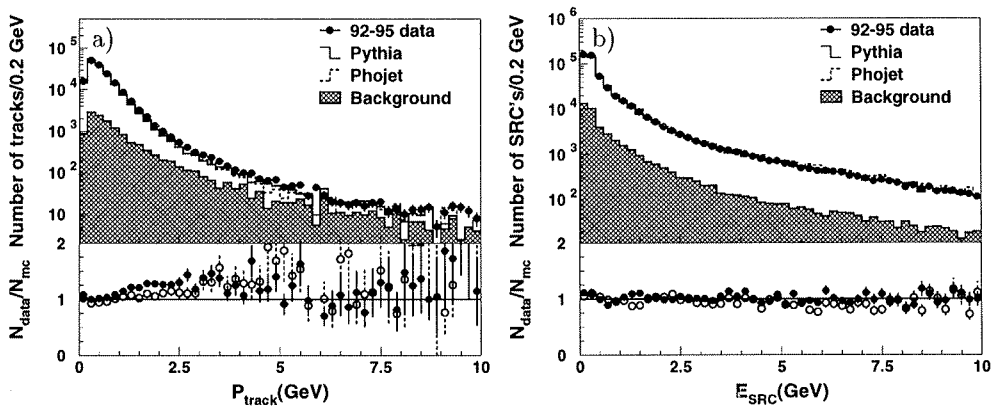

Figure 3.8: *Two tests on single variables: (a) the momentum per good track and (b) the energy per cluster.*

So far, all distributions shown are integrated over the whole mass range. To prove that the sample is described well in each mass bin, the distributions have to be split and shown for each mass bin. In figure 3.9 two selection variables are shown for four different visible mass regions. In both plots the MC agrees well with the data. Only for the longitudinal energy imbalance the lowest mass bin has a problem (PHOJET is flatter than the data).

To check that the selection efficiency is time independent, the sample is split into the four subsamples, one for each years. Ten good runs (one run is defined by the L3 DAQ system, and corresponds to a time period during which the L3 data taking was not stopped) are added to give one period. For each period the number of events selected with a visible mass between 5 and 80 GeV is divided by the integrated luminosity for these ten runs. As can be seen in figure 3.10 this cross section does not change significantly during the year (omitting the beginning of the years). But the average level for each year varies, these are the fit results shown in he different plots (A0). This variance is taken into account as a systematical uncertainty in the final result.

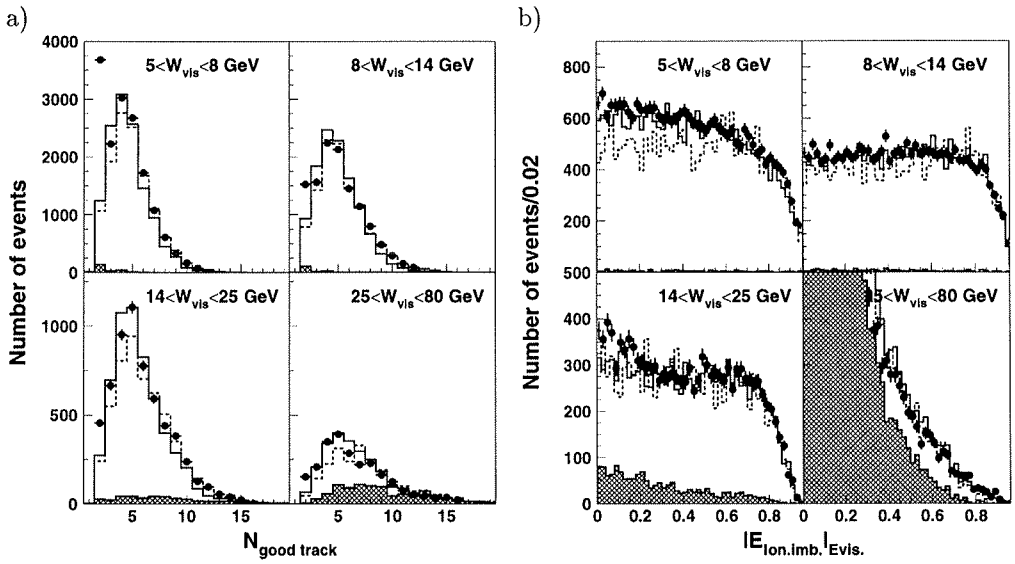

Figure 3.9: *Two examples showing the distributions of variables used to select events, split into four different mass regions: (a) the number of good tracks and (b) the normalised longitudinal-energy imbalance.*

3.2 Data taken around 133 GeV

In this section the selection of the events at 133 GeV is explained. The background coming from the Z decay is small at these energies and the selection criteria are therefore modified such that they are more loose here than for the 90 GeV data.

3.2.1 Data selection

The selection of the events is similar to the selection at 90 GeV. The selection criterion on the longitudinal energy imbalance has been removed and has been replaced by selection on the energies deposited in the BGO and the HCAL.

Selection criteria on energy

One of the backgrounds for the two-photon events is the production of a Z^0 boson (together with a photon) which decays into a quark-anti-quark pair. To reduce this background a selection is made on the energy seen in the electro-magnetic and hadron calorimeters. The energy seen in the electro-magnetic calorimeter should be less than 20 GeV, also the energy seen in the hadron calorimeter should be less than 20 GeV (see 3.11).

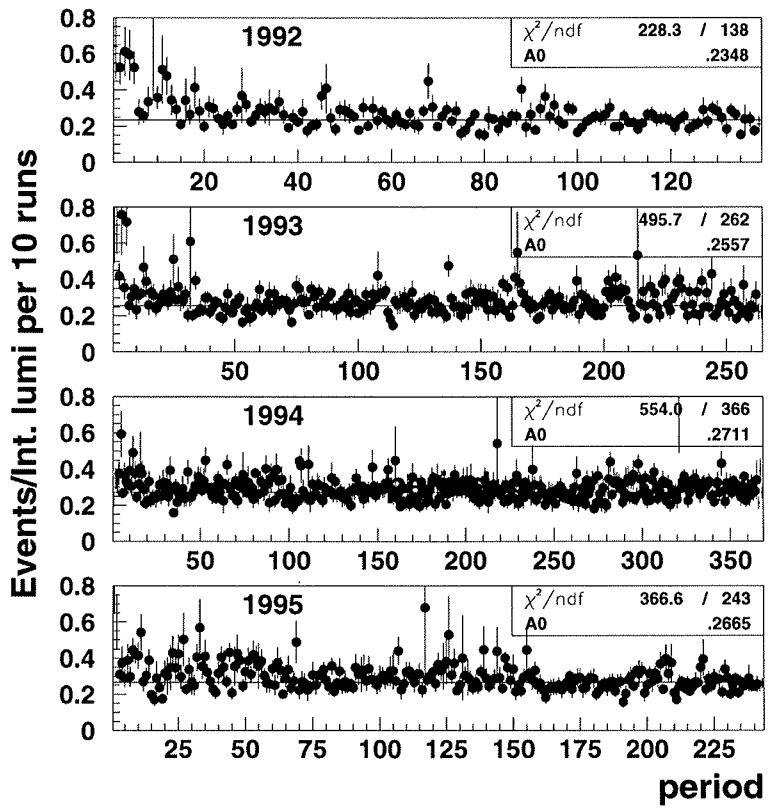

Figure 3.10: *The number of selected events divided by the integrated luminosity averaged over a period of ten runs, for the four different years.*

Number of tracks

In order to remove leptonic two-photon events ($e^+e^- \rightarrow e^+e^-l^+l^-$) a selection is made on the number of good tracks. In figure 3.12 the number of tracks per event is plotted. At least three good tracks are required. This selection criterion also removes some additional backgrounds not mentioned before. These are di-muon and di-electron events (the two-track events not predicted by the Monte Carlo) coming from the decay of a Z boson, which had badly reconstructed energy or which had an extra photon in the event.

Ratio of good over all tracks

The previous selection criterion reduced background coming from the leptonic two-photon events. But also the beam-gas and beam-wall events have to be reduced. This is done by looking at the number of good tracks divided by the number of all found tracks. In

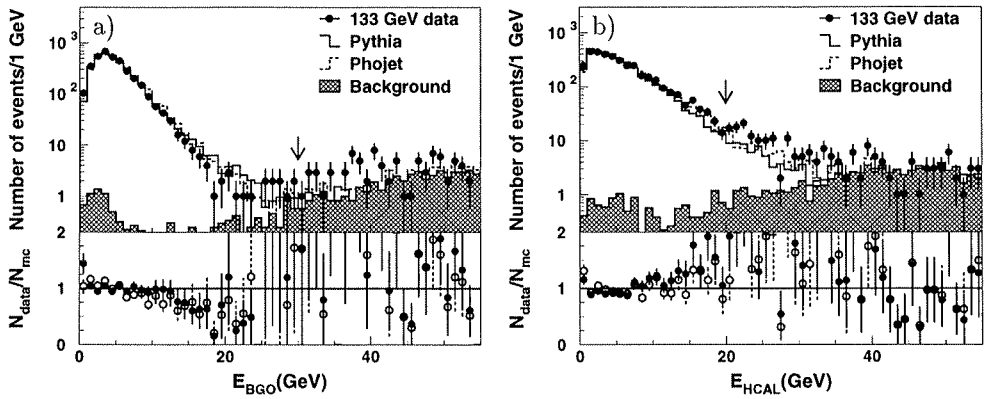

Figure 3.11: *The energy depositions: (a) the energy deposited in the BGO is plotted and (b) the deposition in the HCAL is shown.*

figure 3.12 the ratio between the number of good tracks and the number of all tracks is plotted. The ratio for a good event must be at least 0.55.

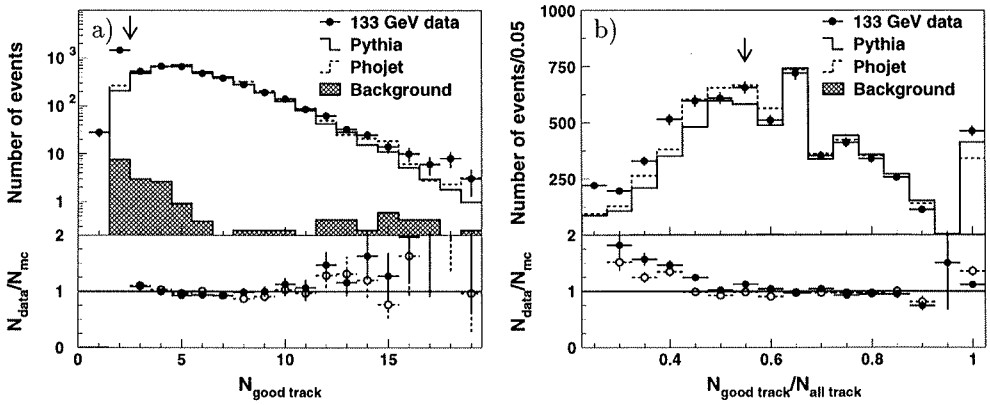

Figure 3.12: *The two track variables: (a) the total number of good tracks per event and (b) the ratio of good over all tracks.*

Miscellaneous selection criteria

To remove beam-gas events, a selection is made on the longitudinal value of the event vertex. This value should be smaller than 200 mm (see the 90 GeV data, figure 3.6). In order to obtain untagged events, no cluster in the luminosity monitor may have more than 30 GeV. To ensure hadronic activity at least 0.5 GeV of energy should be deposited in

the HCAL. And for a complete description of the data by the MC only events triggered by the TEC trigger are selected.

Because the minimum two-photon mass generated in the MC was 5 GeV, only events with a visible mass between 6.5 and 80 GeV are considered. Below this 6.5 GeV, threshold effects from the MC exist and above 80 GeV almost no two-photon events are left and the background from the Z production becomes larger for higher masses.

3.2.2 Data integrity

The data integrity is investigated by looking at the distributions coming from the tracks and the clusters. In figure 3.13 these distributions are shown. A second check is made on the selection variables. These variables are plotted for four different mass regions, this is done in order to check wether the sample is also correctly described in each bin and not only the whole integrated distributions. In figure 3.14 these selection variables are shown for the four mass regions.

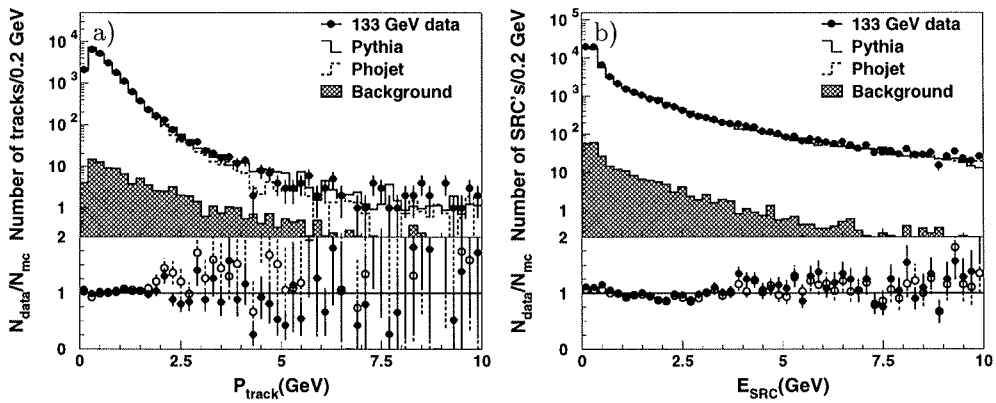

Figure 3.13: *Two individual variables: (a) the momentum per good tracks and (b) the energy per cluster.*

3.3 Cross section calculation

The visible mass of an event is calculated with the energy vectors from several subdetectors, the smallest resolvable clusters (SRC's), the muonic energy as found in the muon chambers, and the energy in the luminosity monitor. All these clusters give information about the energy which is deposited in the detector, but not about the energy which is lost down the beam pipe or in other gaps in the detector. Due to this loss the reconstructed visible mass will in most events be smaller than the true mass. The difference between the visible mass and the true mass depends on various event variables. This dependence is not known on an event-by-event basis and the true mass can thus not be derived on an event-by-event basis.

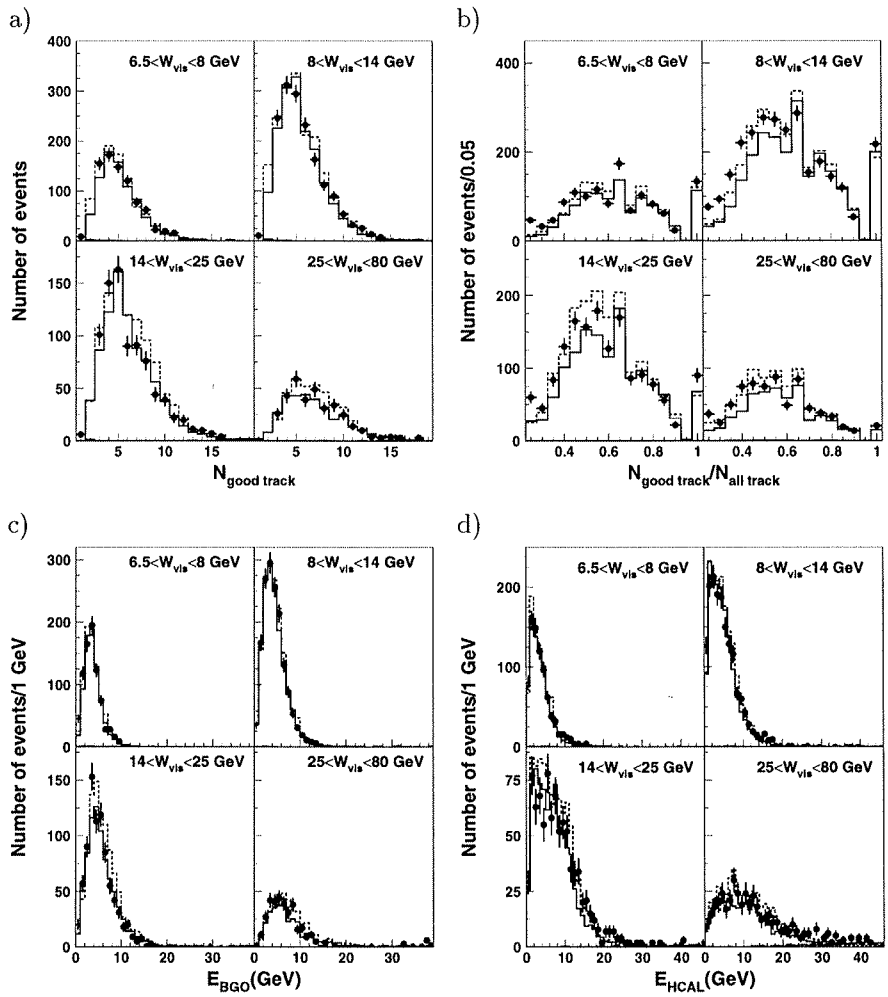

Figure 3.14: *The four variables used to select events divided into the four mass bins: (a) the number of good tracks, (b) the ratio of good over all tracks, (c) the deposited energy in the electromagnetic calorimeter and (d) in the hadron calorimeter.*

The measurement of the cross section as a function of the true mass can be compared with the models of chapter 1 and with the previous results of the other experiments. The distribution of the visible mass is only of interest when the data and MC samples are compared but are of no interest when the two-photon cross section is considered. For this reason the true mass distribution must be found. A procedure which relates a measured distribution to a true distribution is unfolding (see Appendix B).

The measured and unfolded distributions are shown in figures 3.15 and 3.16. The differences between the results and the models are small.

From the unfolded mass distribution the two-photon cross section can be derived for each bin. The cross section per bin is given by:

$$\sigma_{\gamma\gamma} = \frac{N^{\text{unfolded}}}{\mathcal{L}_{ee}\mathcal{L}_{\gamma\gamma}}. \tag{3.2}$$

Here, N^{unfolded} is the total number of events after unfolding, during the unfolding the acceptance is taken into account, $\mathcal{L}_{ee}$ is the total integrated luminosity and $\mathcal{L}_{\gamma\gamma}$ is the two-photon luminosity integrated over all unmeasured variables. The integration over the two-photon luminosity function is done with the improved EPA refeq:epa2. So the total two-photon cross section can be obtained directly from the unfolded number of events (after integration is performed over the mass range of the bin).

The cross sections are given in tables 3.1 and 3.2. These cross sections are the average of the two models used. In the tables all contributions to the total uncertainties are shown. The uncertainty due to the limited MC sample and the statistical uncertainty of the data are implemented in the uncertainty as given by the unfolding programmes, ΔUnfolding statistics. The two methods give different results for the cross section. The differences between the two models contribute to the total uncertainty, ΔUnfolding method. The cross sections are calculated for the different years separately. The variances between the results are given as ΔYears (only for the data taken around the Z pole). The next uncertainty results from the two different form factors used for the calculation of the two-photon luminosity function, the difference is given as $\Delta\mathcal{L}_{\gamma\gamma}$.

The systematical uncertainties for each selection criterion are obtained by calculating the variance of each cross section due to the variation of the criterion. This implies that one criterion is changed while the others remain unchanged. Then the distributions are unfolded and the cross sections are derived again. This is repeated for several different values for each criterion (the values behind the criterion in table 3.1). The variances of the results are taken as the uncertainties due to the selection criterion. Selection criteria which are not mentioned in the tables gave variances that were smaller than the uncertinties due to the unfolding statistics. These criteria do not contribute to the total systematical uncertainties.

For the data obtained around the Z pole there is an additional uncertainty. Since the average value of the two models is used, the systematical uncertainties from the selection criteria remain small. Especially for the number of good tracks a large systematical uncertainty is expected because this distribution is not well described by the two MC samples. But the two models yield opposite behaviours for this distribution, PYTHIA is too high for events with a small number of tracks while PHOJET is too low. For events with a large number of tracks PYTHIA is too low while PHOJET describes these events

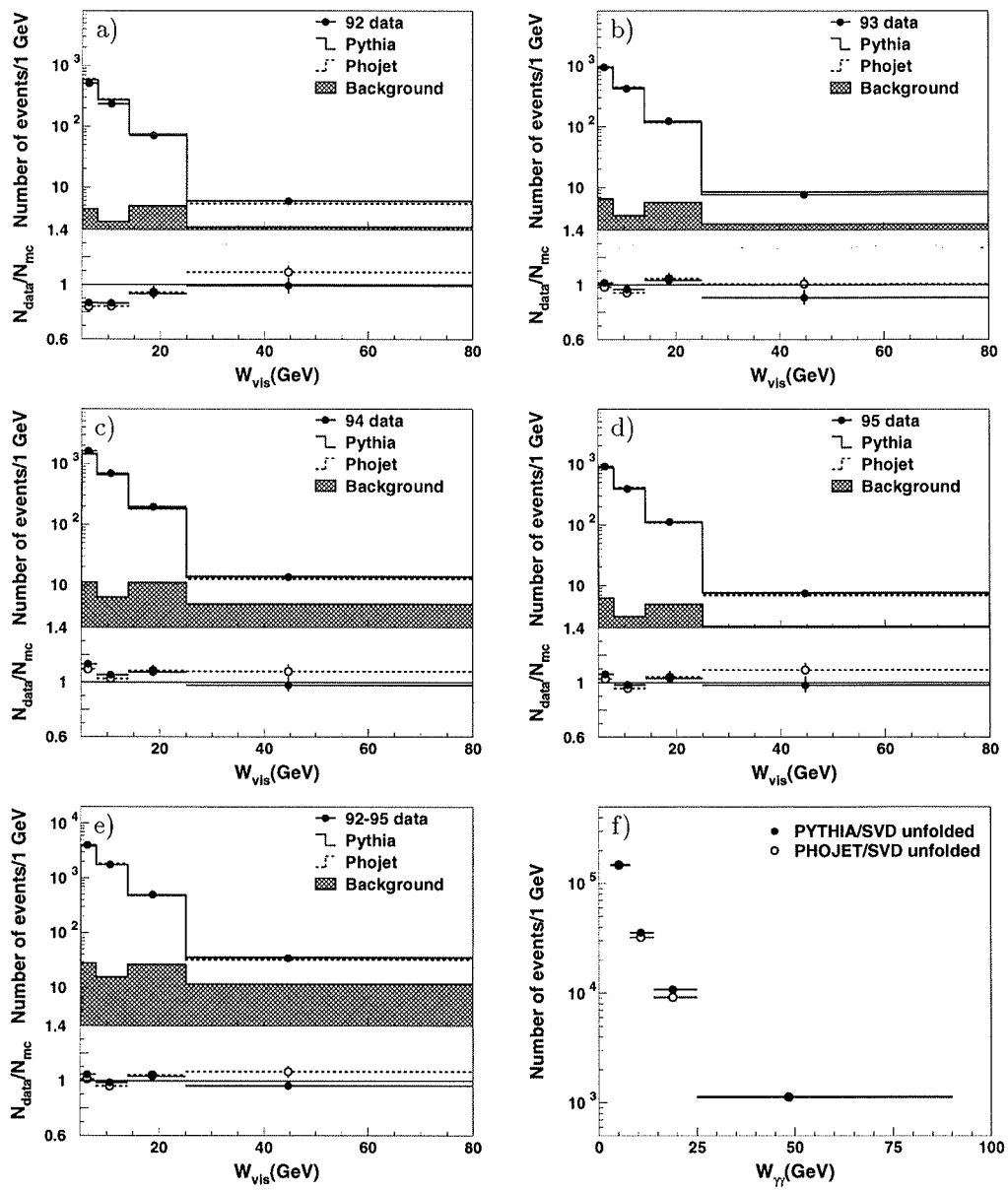

Figure 3.15: *The measured mass distributions for the data taken around the Z pole: (a) 1992 data, (b) 1993 data, (c) 1994 and (d) 1995 data, (e) the sum of all years and (f) the unfolded mass distributions for all years combined.*

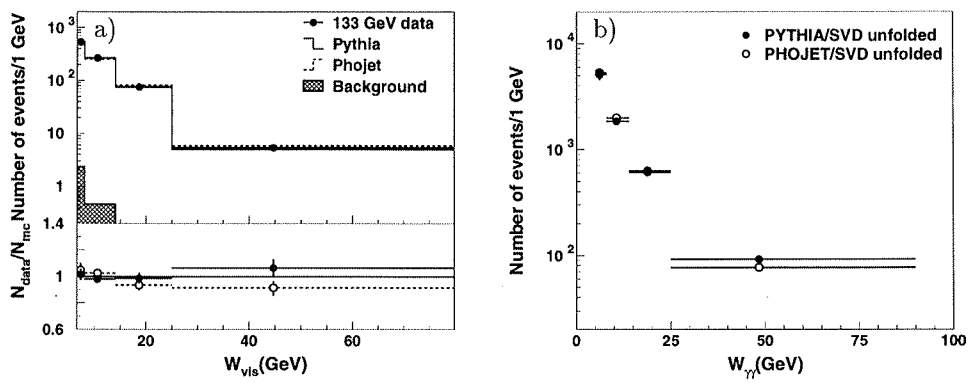

Figure 3.16: *The mass distributions for the 133 GeV data: (a) the measured mass and (b) the unfolded mass.*

satisfactorily. To estimate the influence of this difference in the two models, the difference in cross section between the two models is derived for the different minimum number of good tracks. The variance is taken as the systematical uncertainty due to this difference in the two models, ΔMC.

The largest contributions to the total uncertainties for the measurement around the Z pole comes from the difference between the four years and the difference between the two models.

3.4 Cross section fits

The cross sections found in the previous section can be compared to those results mentioned in chapter 1, see figure 3.17. As can be seen for the small masses the results found are in agreement with these previous data. Also that the bins for the largest masses, presented here, are at larger masses than the previous results.

In order to verify the Donnachie-Landshoff prediction for universal exponents, the data is fitted with equation 1.31. For the first fit the two exponents are fixed and only the X and Y values are fitted. This gives ($s = W^2$ in GeV^2)

$$\sigma_{\gamma\gamma}(s) = (198 \pm 10)\left(\frac{s}{s_0}\right)^{0.0808} + (516 \pm 38)\left(\frac{s}{s_0}\right)^{-0.4525} \text{nb},$$

with χ^2/dof=2.62. This result agrees with the prediction found by Schuler and Sjöstrand for the pomeron term, the reggeon term is larger by 6 standard deviations.

In figure 3.10 an overall normalisation problem exists between the different years. On the assumption that the overall scaling has also been a problem for the other experiments, the results of the experiments can be made more consistently by scaling them. The fitted scaling factors are presented in table 3.3.

$W_{\gamma\gamma}$ (GeV)	5-8	8-14	14-25	25-80
	σ (nb)			
$\sigma_{\gamma\gamma\to X}$	377	327	305	382
ΔUnfolding statistics (see Appendix B)	± 11	± 4	± 5	± 9
ΔUnfolding method (BAYES vs SVD)	± 46	± 2	± 12	± 12
ΔYears (see plot 3.10)	± 57	± 39	± 23	± 15
$\Delta\mathcal{L}_{\gamma\gamma}$ (GVDM vs ρ-pole)	± 11	± 10	± 9	± 11
$\Delta E_{\text{lon.imb.}}$ (0.35-0.55)	$^{+0}_{-16}$	$^{+4}_{-0}$	$^{+10}_{-0}$	$^{+0}_{-57}$
$\Delta E_{\text{tra.imb.}}$ (3-5 GeV)	$^{+0}_{-5}$	$^{+1}_{-1}$	$^{+3}_{-0}$	$^{+0}_{-29}$
$\Delta N_{\text{good track}}$ (4-6 tracks)	$^{+11}_{-0}$	$^{+28}_{-0}$	$^{+28}_{-0}$	$^{+0}_{-54}$
ΔRatio good over all tracks (0.45-0.65)	$^{+25}_{-3}$	$^{+11}_{-0}$	$^{+5}_{-5}$	$^{+29}_{-29}$
ΔE_{HCAL} (0-2 GeV)	$^{+2}_{-13}$	$^{+2}_{-2}$	$^{+4}_{-0}$	$^{+10}_{-10}$
ΔMissing energy (-40 to -20 GeV)	$^{+2}_{-8}$	$^{+2}_{-2}$	$^{+8}_{-2}$	$^{+0}_{-28}$
ΔTrigger	± 20	± 16	± 15	± 8
ΔMC (PYTHIA vs PHOJET)	± 67	± 49	± 34	± 29
Δ Total	$^{+106}_{-103}$	$^{+72}_{-65}$	$^{+56}_{-46}$	$^{+49}_{-101}$

Table 3.1: *The total cross sections for the different mass bins and their total uncertainties for the data taken around the Z pole.*

$W_{\gamma\gamma}$ (GeV)	5-8	8-14	14-25	25-80
	σ (nb)			
$\sigma_{\gamma\gamma}$	410	364	342	408
Δ Unfolding statistics	$\pm$ 28	$\pm$12	$\pm$12	$\pm$13
Δ Unfolding Method	$\pm$ 17	$\pm$10	$\pm$ 3	$\pm$21
$\Delta\mathcal{L}_{\gamma\gamma}$	$\pm$ 12	$\pm$11	$\pm$10	$\pm$12
Δ MC	$\pm$ 8	$\pm$16	$\pm$ 7	$\pm$34
Δ Number of good tracks	+114 − 10	+60 − 0	+12 −12	+ 0 −36
Δ Ratio of good over all tracks	+ 48 − 9	+ 6 − 6	+15 −30	+14 − 0
Δ E_{HCAL}	+ 19 − 0	+ 9 − 9	+ 0 −10	+14 − 5
Δ Trigger	$\pm$ 22	$\pm$18	$\pm$17	$\pm$ 9
Δ Total	+132 − 44	+68 −32	+31 −42	+49 −58

Table 3.2: *The total cross sections for the different mass bins and their total uncertainties for the data taken around 133 GeV.*

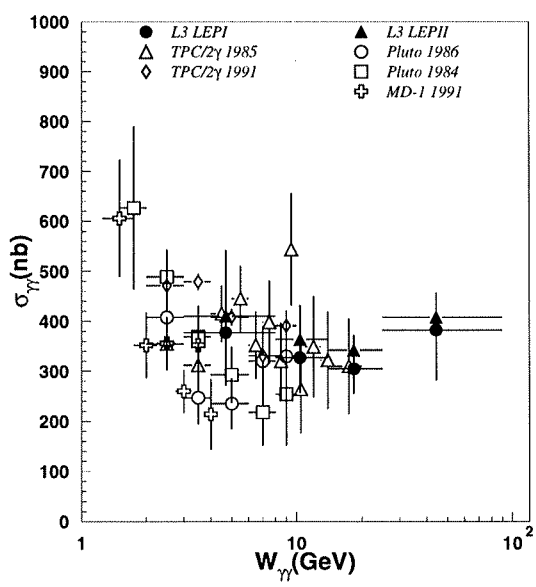

Figure 3.17: *The two-photon cross section from this thesis compared to previous results.*

Data set	scaling factor
Pluto 1984	1.11 ± 0.13
Pluto 1986	1.40 ± 0.18
TPC 1985	1.10 ± 0.12
TPC/2γ 1991	0.93 ± 0.09
MD-1 1991	1.38 ± 0.17

Table 3.3: *Scaling factors for the different experimental results.*

The result for the fit is given by:

$$\sigma_{\gamma\gamma}(s) = (195 \pm 4)\left(\frac{s}{s_0}\right)^{0.0808} + (498 \pm 18)\left(\frac{s}{s_0}\right)^{-0.4525} \text{nb},$$

with χ^2/dof=1.36. The improvement is large for the χ^2 value but does not change significantly the outcome of the fitted cross section.

To go one step further, not only X and Y are fitted but also both exponents, ϵ and η. Again if the cross sections are fitted as given or with the fitted scale factors, almost the same results are obtained:

$$\sigma_{\gamma\gamma}(s) = (19 \pm 34)\left(\frac{s}{s_0}\right)^{0.34\pm0.20} + (576 \pm 60)\left(\frac{s}{s_0}\right)^{-0.18\pm0.08} \text{nb}.$$

With χ^2/dof=1.34. The correlation between the four variables is close to 1. Thus although the result looks different from the two-variable fit, the two values for χ^2 are very close and so are the functions found (see figure 3.18).

3.5 Summary and conclusions

For the analysis of the untagged sample or total cross section measurement the aim was to obtain two-photon cross sections at masses larger than measured before. The Monte Carlo samples gave a satisfactory description of the variables used to select the events. Only the number of charged particles (tracks) showed a different behaviour both between the data and the two Monte-Carlo samples and between the two MC samples. This introduced a large systematical uncertainty.

For the selected events the reconstructed masses were smaller than the true masses, due to this fact the reconstructed mass distribution needed to be unfolded to give the true mass distribution. The unfolded distributions could be used to obtain the total cross section.

The final result showed a good agreement with previous results for masses smaller than 10 GeV. The cross sections were measured up to 90 GeV. This was possible because all information is needed during the unfolding of the measured mass distribution. The cross section was derived for four years, from 1992 to 1995. The differences between the years were around 15 percent, which is a large contribution to the total uncertainty.

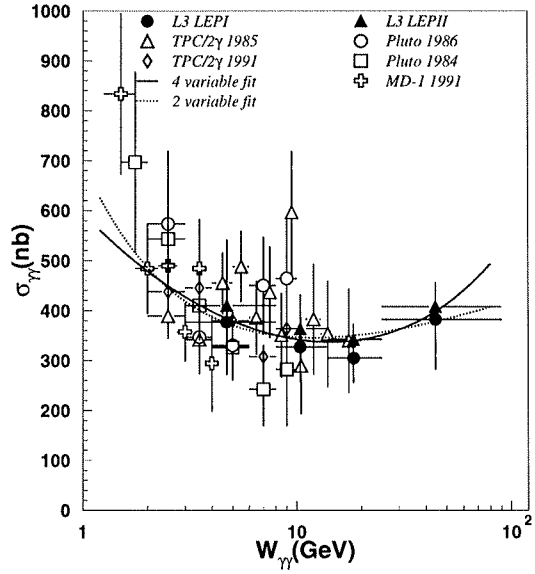

Figure 3.18: *The two-photon cross section from this thesis compared to the scaled previous results. The results for the two fits ar shown as well.*

Also the results obtained with energies around 133 GeV (1995 only) were compared with the 91-GeV data. The former results are about 10 percent higher than the latter, but that is within the uncertainties due to the differences between the years. From this the conclusion is drawn that the background coming from decay of the Z, which is large for the 90-GeV data but small for the 133-GeV data, is thus described satisfactorily and does not significantly influence the results.

The expected rise of the cross section for larger masses has not been measured. Due to the large uncertainties the cross sections found in this thesis could both be described by a flat cross section (see tables 3.1 and 3.2) as well as by a cross section with the expected rise. A fit of the exponent that describes this rise gave a value four times as large as expected but due to the large correlation with the other parameters the fitted function is almost the same as a function with the rise fixed to the predicted value. A measurement with larger masses is needed to obtain a conclusive result concerning the rise.

4

Tagged data

In this chapter the tagged events are investigated. In these events a final-state positron or electron is detected in the luminosity monitor. This electron or positron is called the tag. The presence of a tag is a clear indication that the event under consideration is a two-photon event. The selection of the hadron final state is less strict in the presence of a tag than for the untagged sample. The extra information on Q^2 gives a means to check the form factors applied in the previous chapter.

For the measurement of the tagged cross section the two MC programmes needed to be extended to describe virtual photon-photon interactions. The PHOJET generator multiplies the cross section, calculated with the assumption that the two photons are real, with the GVDM form factors to obtain the cross section for virtual photons. In the PYTHIA generator the direct cross section is multiplied with a form factor which simulates the tagged cross section for the direct cross section (see Appendix B). The other samples (VMD and anomalous) are multiplied with the GVDM form factors.

4.1 Selection of the tags

If the scattering angle of a final state electron or positron is between 26 to 65 mrad, it can be measured in the luminosity monitor. In order to select a luminosity cluster as a tag, the cluster must be a well-reconstructed electromagnetic cluster. By considering the uncertainty in the reconstructed energy, a selection can be performed. If this uncertainty is larger than 10 % the cluster is not considered to be electromagnetic.

In order to remove so-called "off-momentum" electrons, which have an average energy of 25 GeV, the minimum deposited energy of the cluster should be larger than 35 GeV. This also ensures that the level-0 energy trigger fires. This trigger forms, together with the TEC trigger, the single-electron trigger. The single-electron trigger fires when the level-0 energy trigger has fired and the TEC trigger has found at least one track. The energies and angles of the tags selected are shown in figure 4.1.

For the MC sample the generated value for Q^2 can be compared with the reconstructed

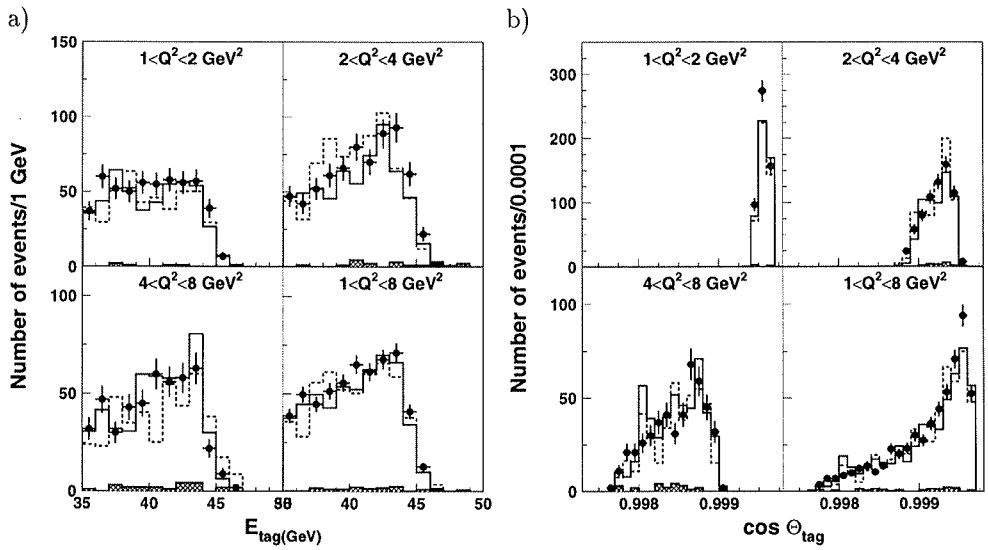

Figure 4.1: *The energies and angles of the selected tags. The dots represent the data, the hatched area is the background. The solid line represents PYTHIA and the dashed line PHOJET.*

value. The relative deviation is defined as:

$$\sigma = \frac{Q^2_{\text{rec}} - Q^2_{\text{gen}}}{Q^2_{\text{gen}}},$$

with Q^2_{gen} the generated value for Q^2 and Q^2_{rec} the reconstructed value. The results from a Gaussian fit for the distributions of this deviation of the Q^2 measurement are given in table 4.1 for the three Q^2 ranges. From this it is clear that the Q^2 values are reconstructed adequately and that no unfolding needs to be done for this variable.

Q^2	mean(%)	width(%)
1-2	2.7	2.4
2-4	1.1	2.1
4-8	0.4	2.2

Table 4.1: *The precision of the Q^2 measurement for the different bins.*

4.2 Selection of the hadronic events

After the tag has been identified the events of interest have to be selected. These events must have some sort of hadronic activity. The selection criteria applied for this are almost identical to the ones used for the untagged sample. Here the main selection criteria are also the number of good tracks and ratio of good over all tracks. Due to the tag the background from the annihilation events is much smaller. The selection criterion on the longitudinal energy imbalance can be skipped. But the events still need to be reconstructed well, thus the transverse energy imbalance must be small.

The hadronic events are selected by requiring that at least three charged particles were found, thus three good tracks. The selection of a good track is identical to the selection applied for the untagged sample. The selected events are shown in figure 4.2 for the lowest mass bin.

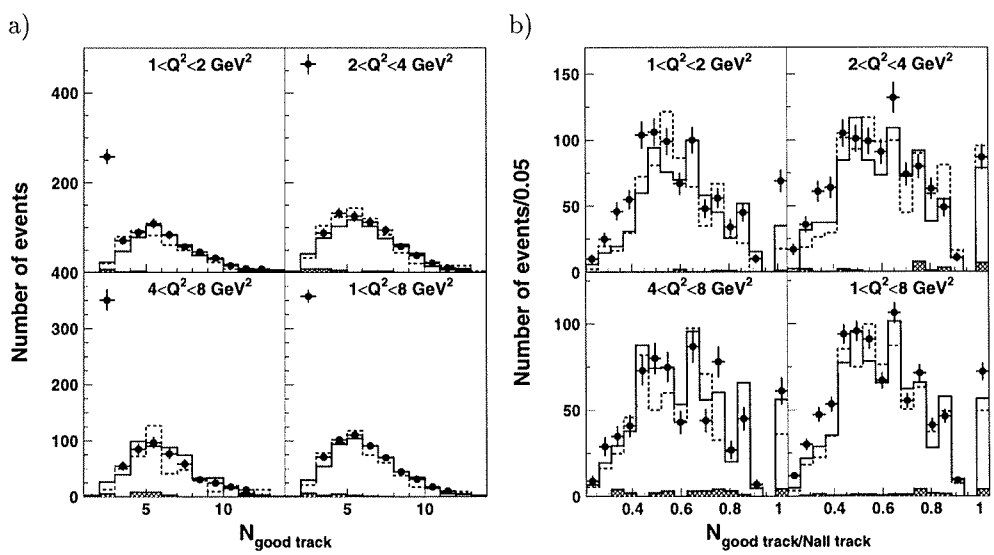

Figure 4.2: *The tracks-based selection criteria for the three Q^2 bins and the sum of the three bins: (a) the number of good tracks and (b) the ratio of good over all tracks. The dots represent the data, the hatched area is the background. The solid line represents PYTHIA and the dashed line PHOJET.*

Again a selection is made on the number of good tracks divided by the total number of found tracks, this ratio should be larger than 0.5. The excess which is seen in all Q^2 bins (see figure 4.2), results mainly from events with small masses. This selection criterion removes events with a too large fraction of badly reconstructed tracks in the data (beam-wall type of events).

The events need to be reconstructed well as was also the case for the selection of untagged events. This is obtained by requiring that the transverse energy imbalance (with the tag included) should be smaller than 4 GeV. The distributions for this imbalance are

shown in figure 4.3. Also shown in this figure are the distributions for the reconstructed azimuthal angle for the hadronic activity minus the azimuthal angle of the tag. For a good reconstructed event the difference between these two angles should be π. Only events in which the transverse energy of the hadronic final state is larger than 1 GeV are taken into account, this to ensure a good azimuthal-angle reconstruction. For these events the difference between the two azimuthal angles should be smaller than $\pi/3$.

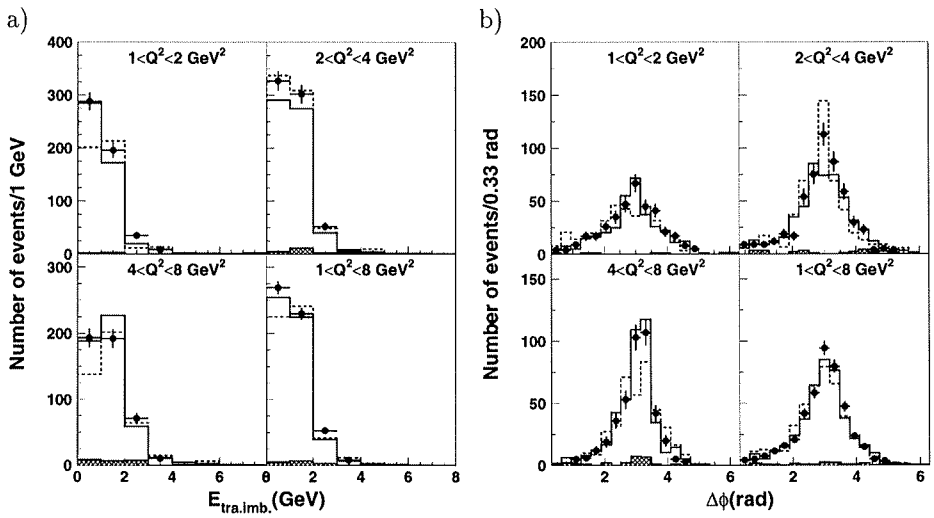

Figure 4.3: *The energy-based selection criteria: (a) the transverse energy imbalance and (b) the azimuthal angle of the hadronic activity minus the azimuthal angle of the tag (modulo 2 π). The dots represent the data, the hatched area is the background. The solid line represents PYTHIA and the dashed line PHOJET.*

4.3 Data integrity

After all selection criteria have been applied, the selected events are checked wether they are good two-photon events and wether still some background from annihilation events is left. This is done by considering the longitudinal energy imbalance. This is shown in figure 4.4. The absence of a peak near zero is an indication that no annihilation events are left in the sample.

The visible mass is derived in the same way as for the untagged events, excluding the tag itself. In figure 4.5 the visible mass is shown. A good agreement exists between PYTHIA and the data. For the second mass bin PHOJET seems to predict too few events for all values of Q^2.

The problems encountered at the untagged sample concerning the true mass distribution are valid here as well. Again the mass has to be taken from the measurement of

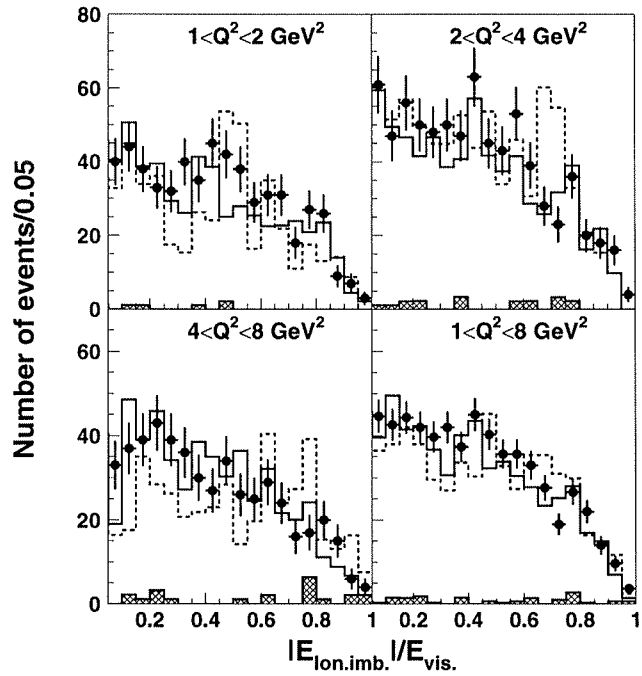

Figure 4.4: *The longitudinal energy imbalance normalised to the visible energy for the three Q^2 bins seperately and for the sum of the three bins. The dots represent the data, the hatched area is the background. The solid line represents PYTHIA and the dashed line PHOJET.*

the hadronic final state and the reconstructed mass will thus be different from the true mass. Due to the transverse boost of the hadronic system, in order to compensate for the transverse momentum of the tag, the reconstructed mass is expected to be closer to the true mass than was the case for the untagged events. But the reconstructed mass distribution is still quite different from the true mass distribution. The unfolding procedures applied for the untagged events have to be used here as well. The reconstructed value for Q^2 is correct within a few percent, the unfolding can thus be performed separately for the different Q^2 bins.

4.4 Results

The true mass distributions are again converted into cross sections with equation 3.2 and the two-photon luminosity function is calculated with the numerical integration method 1.20. Since here the form factors are being measured, the integration is done only over the luminosity function. On the assumption that $\mathcal{L}_{TS} \approx \mathcal{L}_{TT}$, only the transverse-transverse part needs to be integrated over. The measured cross section is thus a sum

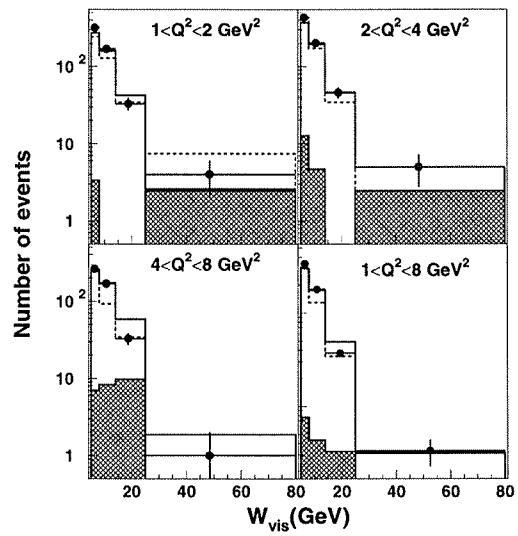

Figure 4.5: *The visible mass for the four Q^2 bins. The dots represent the data, the hatched area is the background. The solid line represents PYTHIA and the dashed line PHOJET.*

of the transverse-transverse and the transverse-scalar part:

$$\sigma_{\text{tag}} = \sigma_{TT} + \epsilon\sigma_{TS}.$$

Here, $\epsilon = \mathcal{L}_{TT}/\mathcal{L}_{TS} \approx 1$. For small values of x (small values of Q^2 compared to W^2) this approximation can be obtained from equation 1.20. When the x^2 terms are neglected f_S become equal to f_T.

The cross sections are calculated in four mass bins and in three Q^2 bins, thus 12 bins in total. The numbers given in table 4.2 are the averages between the two models. The four mass bins, within a given Q^2 bin, have been unfolded to give the true mass distributions inside the Q^2 bin. The uncertainties given by the unfolding methods give the first uncertainties in table 4.2. The differences between the results from the two methods are always smaller than the uncertainties given by the unfolding methods (the "statistical" uncertainties) and are not considered to contribute to the systematical uncertainties.

For the systematical uncertainties resulting from the selection criteria the same procedure is followed here as for the untagged sample. The estimated systematical uncertainties for these selection criteria are calculated in the same manner as before. Thus the selection criterion is varied, which gives a variance of the cross sections. These variances are presented in table 4.2. The variances resulting from the selection criterion on the transverse energy was smaller than the statistical uncertainty and are thus not considered to contribute to the total systematical uncertainties.

The differences between the results obtained with the different MC samples are used to estimate the uncertainty from the models applied.

Because the luminosity function is calculated without any form factor, no uncertainty from this source is quoted. A second uncertainty for the untagged sample which is not mentioned here, is the difference between the different years. This is due to the fact that the number of events is too low for each year separately.

The results for the cross section are presented in two different manners. First the cross section is shown for each Q^2 bin as a function of the true mass. Second as a function of Q^2 in each mass bin.

4.4.1 Mass dependence

The unfolding is performed with both MC samples. The differences between the results are larger than the uncertainties seen after unfolding. They are averaged over the two models to give the result shown in figure 4.6.

The mass dependence is expected to show a rise for higher masses, similar to the untagged sample. If the photon behaves like a hadron, the rise of the cross section for larger masses is expected to be steeper for larger values of Q^2, like the results found by ZEUS and H1 ([54–56]). Due to the large uncertainties it is not clear from this measurement wether this is the case. All three distributions are fitted nicely with a constant cross section (χ^2/dof<1). A two-variable fit of the Donnachie-Landshoff parametrisation (taking the Reggeon exponent fixed to 0.4525 and the Pomeron exponent fixed to 0.2 as indicated by reference [55]) gives results that have Pomeron terms which are significantly larger than zero but with Reggeon contributions which are comparable with zero. The two fitted functions are plotted for the three Q^2 bins in figure4.6.

4.4.2 Q^2 dependence

The cross section can also be given as a function of Q^2. This is shown in figure 4.7. The different mass bins are the same as for the untagged sample. So it is possible to use the results from the untagged sample here as well ($< Q^2 >$=0.01).

If the cross sections are factorised, the same Q^2 behaviour must be observed in all four mass bins. Different form factors can be compared to the data, the standard GVDM, the TPC/2γ VDM and the ρ pole. Also the direct contribution can be added to the form factors.

The dependence is fitted for each mass bin with the parametrisation also applied by PLUTO:

$$\sigma(W, Q^2) = \sigma_0(W)\left(F_T(Q^2) + F_S(Q^2)\right) + \sigma_{QPM}(W, Q^2).$$

Here, σ_{QPM} is the cross section for the QPM as given for four quark flavours, the sum of equation 1.35 and 1.36, $F_{T,S}$ are the different form factors and σ_0 is determined in the fit.

The results for the six fits for each of the four mass bins is shown in table 4.3.
From this table it appears that for the three large-mass bins ($W_{\gamma\gamma} > 8$ GeV) the best description results from the sum of the QPM and the standard GVDM (lowest χ^2 values) but the standard GVDM gives a good description as well (χ^2 smaller than the degrees of freedom). For the lowest mass bin the smallest χ^2 value comes from the standard GVDM

Q^2 (GeV^2)	1-2				2-4				4-8			
$W_{\gamma\gamma}$ (GeV)	3-8	8-14	14-25	25-90	3-8	8-14	14-25	25-90	3-8	8-14	14-25	25-90
	σ (nb)											
$\sigma_{\gamma\gamma\to X}$	102	94	85	93	52	55	56	69	31	40	40	65
ΔUnfolding statistics	± 10	± 7	± 6	± 11	± 6	± 4	± 3	± 8	± 4	± 3	± 4	± 10
$\Delta N_{\text{goodtrack}}$	$^{+0}_{-31}$	$^{+0}_{-15}$	$^{+5}_{-5}$	$^{+29}_{-0}$	$^{+0}_{-5}$	$^{+0}_{-5}$	$^{+0}_{-5}$	$^{+0}_{-7}$	$^{+0}_{-12}$	$^{+0}_{-11}$	$^{+0}_{-4}$	$^{+10}_{-4}$
ΔRatio	$^{+26}_{-0}$	$^{+15}_{-0}$	$^{+0}_{-6}$	$^{+0}_{-28}$	$^{+6}_{-0}$	$^{+3}_{-0}$	$^{+0}_{-6}$	$^{+0}_{-16}$	$^{+1}_{-1}$	$^{+1}_{-1}$	$^{+1}_{-1}$	$^{+4}_{-4}$
$\Delta\delta\phi$	$^{+23}_{-0}$	$^{+17}_{-0}$	$^{+4}_{-4}$	$^{+0}_{-14}$	$^{+7}_{-0}$	$^{+6}_{-0}$	$^{+4}_{-0}$	$^{+4}_{-4}$	$^{+2}_{-0}$	$^{+3}_{-0}$	$^{+7}_{-0}$	$^{+4}_{-0}$
ΔE_{tag}	± 7	± 3	± 5	± 15	± 3	± 2	± 2	± 0	± 4	± 2	± 1	± 3
ΔMC sample	± 24	± 26	± 11	± 7	± 18	± 8	± 4	± 15	± 13	± 4	± 8	± 28
ΔTotal	$^{+44}_{-41}$	$^{+35}_{-31}$	$^{+15}_{-16}$	$^{+35}_{-37}$	$^{+21}_{-20}$	$^{+11}_{-10}$	$^{+7}_{-9}$	$^{+17}_{-25}$	$^{+14}_{-19}$	$^{+6}_{-12}$	$^{+10}_{-10}$	$^{+33}_{-31}$

Table 4.2: *The cross sections and their uncertainties.*

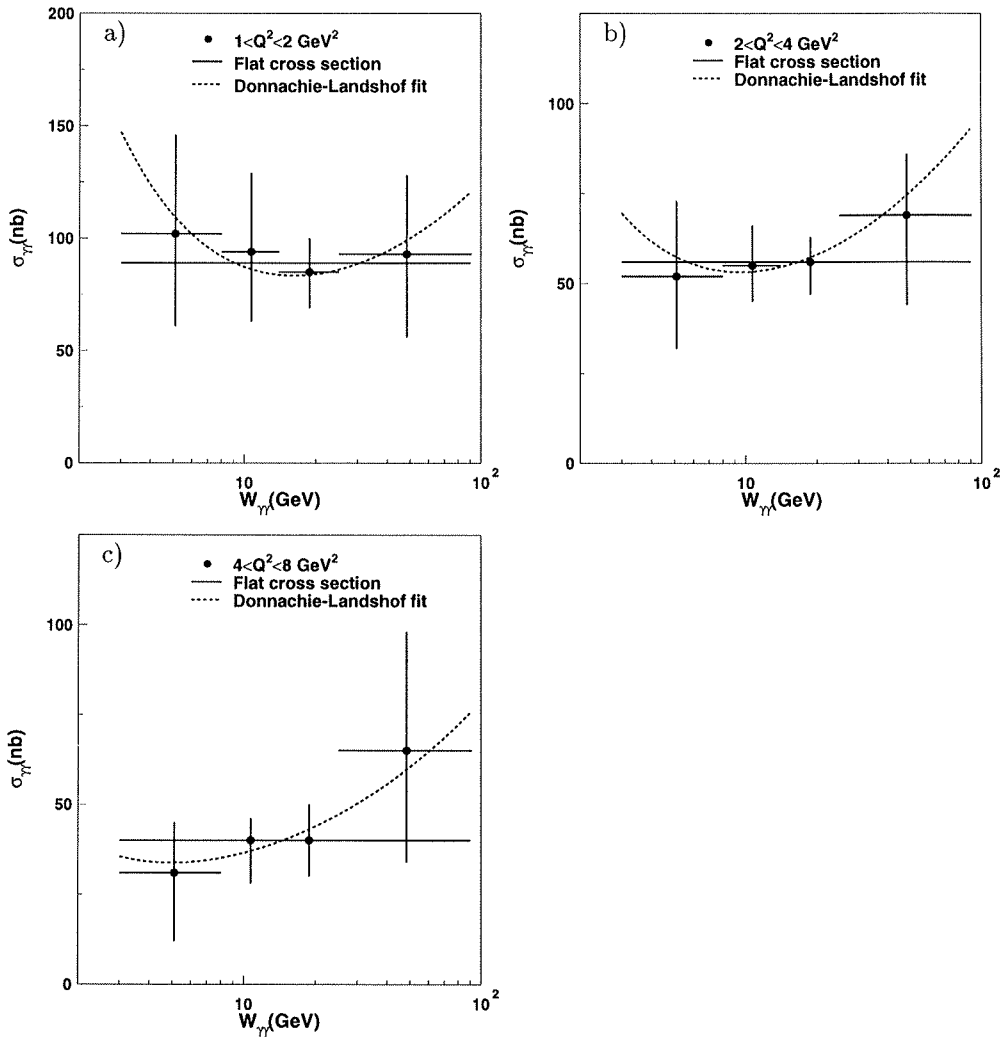

Figure 4.6: *The tagged cross sections as function of the mass: (a)* $1 < Q^2 < 2$ *GeV*^{2}*, (b)* $2 < Q^2 < 4$ *GeV*^{2} *and (c)* $4 < Q^2 < 8$ *GeV*^{2}*. The solid lines correspond to the fitted flat cross section, while the dashed line give the Donnachie-Landshoff fit.*

W (GeV)	5-8	8-14	14-25	25-90	5-8	8-14	14-25	25-90
model	χ^2				σ_0(nb)			
QPM+GVDM	3.31	0.08	0.59	0.99	223±72	316±50	329±31	409± 61
QPM+VDM	0.77	4.13	15.9	6.06	328±94	379±64	418±43	454± 72
QPM+ρ pole	0.72	4.61	17.7	6.55	333±95	380±65	421±44	455± 72
GVDM	0.12	1.05	1.67	1.08	378±47	376±50	353±31	412± 61
VDM	2.60	11.5	22.3	6.39	471±94	429±64	443±43	457± 72
ρ pole	2.96	12.4	24.5	6.90	475±95	430±65	446±44	458± 72

Table 4.3: *The results from the six different models fitted to the results in the four different mass bins.The value for χ^2 has not been divided by the degrees of freedom (3).*

without the QPM added to it. But all the models give values for χ^2/dof smaller than or equal to one. None of the models can thus be excluded for the smallest-mass bin.

The smallest-mass bin can be compared to the results given in chapter 1. As can be seen in figure 4.8 they agree nicely with both measurements.

4.5 Summary and conclusions

For the measurement of the tagged cross section the two MC programmes needed to be extended to describe virtual photon-photon interactions. After the modifications the event variables are described satisfactoriliy for this analysis.

The results were shown in two different manners. First the cross section was shown as a function of the mass. The tagged cross section is expected to rise for large masses, and this rise is expected to be steeper with increasing virtuality. The cross sections found can be fitted with a flat cross section as function of the mass. A small rise seems to be visible but due to the large uncertainties this rise could not be fitted. So the data is not good enough to distinguish wether the cross section is described better with a flat cross section or with a rise for large masses.

Second the cross section was shown as a function of the virtuality Q^2. In this manner the form factors could be tested. Six different functions were fitted to the tagged data. For the bin with the smallest masses all functions gave an adequate description of the cross section. For the bins with larger masses only two form factors gave satisfactory results (χ^2 values) for the fit. This was the description of the GVDM form factors multiplied with a determined factor or the description with the QPM summed to the GVDM term.

From the first description it is concluded that the cross section factorises, the cross section can be described by a mass-dependent part times a Q^2-dependent part.

For the near future the results coming from LEP 2 must give evidence wether the expected rise is in the two-photon cross section as predicted by the two generators or that the cross section remains flat for masses above 20 GeV.

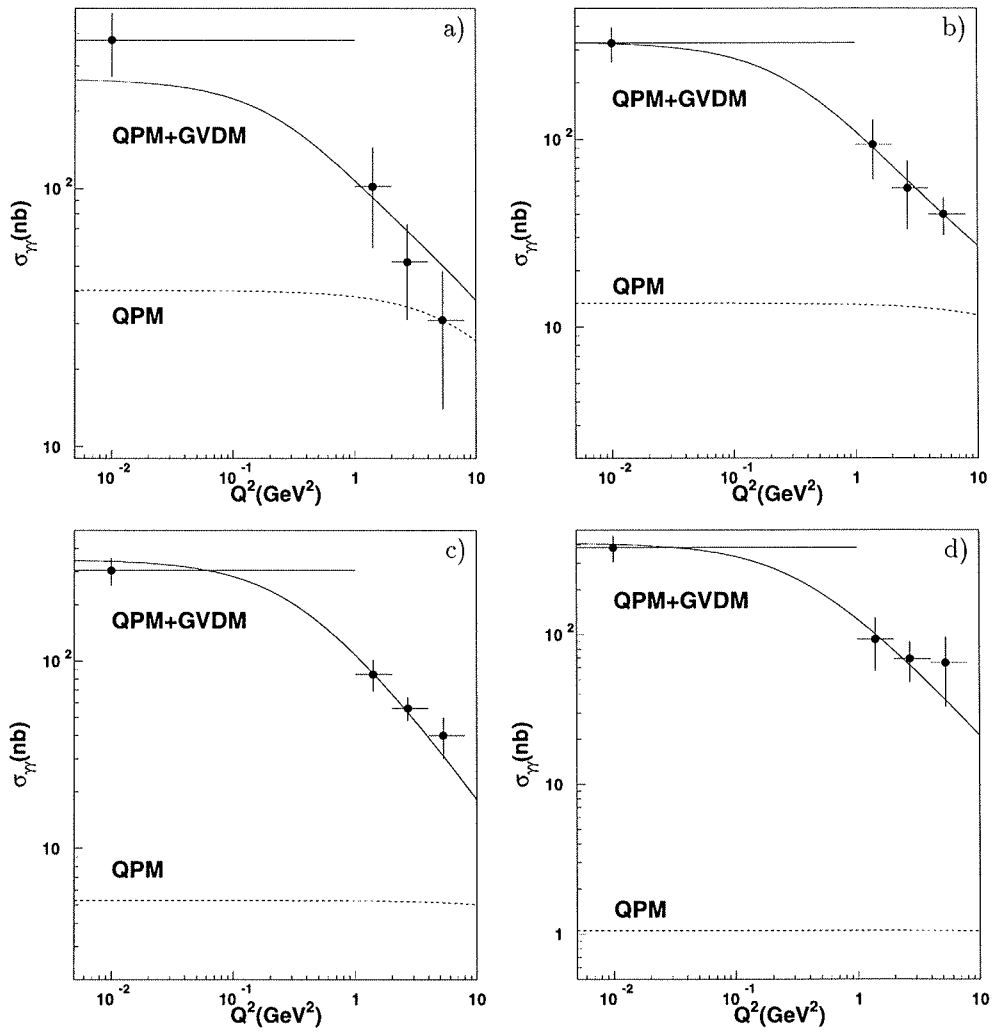

Figure 4.7: *The tagged cross sections as a function of Q^2: (a) $3 < W_{\gamma\gamma} < 8$ GeV, (b) $8 < W_{\gamma\gamma} < 14$ GeV, (c) $14 < W_{\gamma\gamma} < 25$ GeV and (d) $25 < W_{\gamma\gamma} < 90$ GeV. The solid line corresponds QPM plus the GVDM form factor times the determined cross section for the corresponding mass bin. The QPM model is drawn with the dashed line.*

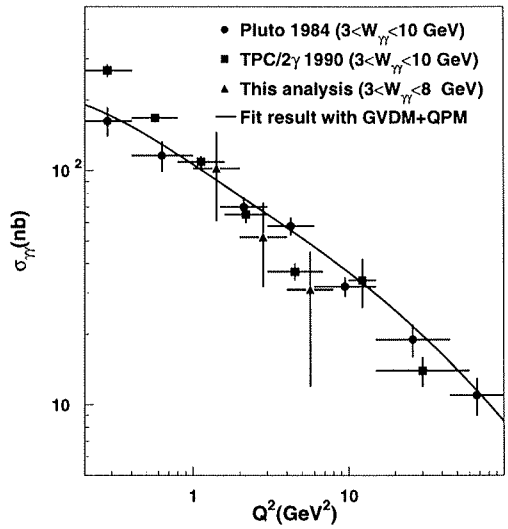

Figure 4.8: *The comparison between the results obtained in this analysis and the previous results mentioned in chapter 1.*

Appendix A

Unfolding

First the problem, how to derive the true distribution from a measured distribution, is illustrated with the help of a simple example. Then two different unfolding procedures are discussed and finally these two procedures are compared and the validity of the results is evaluated.

A.1 Introduction

The problem is to derive the true distribution from a measured distribution. If a quantity is measured uncertainties are always introduced; these uncertainties are combinations of uncertainties in the measured values and inefficiencies of the apparatus. In this thesis the mass of a two-photon event has both sources of uncertainties. First the measured particles have an uncertainty in the measurement of the energy and angle. Second, some particles escape detection along the beam-pipe and other areas where detection material is lacking. These inefficiencies lower the value of the visible mass with respect to the true mass. Due to these two contributions the true value of the mass can not be determined from the measured value on an event-by-event basis.

For an MC sample the true and measured values for a certain variable are known. This implies that a matrix can be constructed which relates the measured distribution to the generated distribution. If x^{gen} denotes the generated distribution and x_{MC}^{meas} the simulated measured distribution,

$$x_{MC}^{\text{meas}} = Ax^{\text{gen}}. \tag{A.1}$$

Here, A is the matrix which relates the two distributions. The elements are normally calculated by an MC sample and are given by:

$$A_{ij} = \frac{N_{ij}}{N_j}. \tag{A.2}$$

Here, N_j is the total number of events generated in bin j and N_{ij} is the number of events measured in bin i and generated in bin j. This yields a matrix with only positive numbers

or zero. This means that column j gives the response of the experiment to the events generated in this bin. Notice that all $A_{ij} \geq 0$.

The problem of calculating the true distribution from the measured distribution now seems very simple. Equation A.1 suggests that the inverse matrix must be multiplied with the measured distribution, thus:

$$x^{\text{unf}} = A^{-1} x^{\text{meas}}. \tag{A.3}$$

Here, x^{unf} is the unfolded data and x^{meas} the measured distribution in the data. However, the inverse matrix may not exist and if it exists the inverse matrix will have negative values which can lead to negative (unphysical) values for the unfolded distribution.

To illustrate this a two-by-two matrix is taken as an example (this example is taken from [59]):

$$A = \frac{1}{2} \begin{pmatrix} 1+\epsilon & 1-\epsilon \\ 1-\epsilon & 1+\epsilon \end{pmatrix}. \tag{A.4}$$

Here, ϵ indicates how well both bins are separated by the experiment, if $\epsilon = 1$ the response is perfect, if $\epsilon = 0$ the two bins can not be separated. The inverse matrix is given by ($\epsilon \neq 0$):

$$A^{-1} = \frac{1}{2\epsilon} \begin{pmatrix} 1+\epsilon & -1+\epsilon \\ -1+\epsilon & 1+\epsilon \end{pmatrix}. \tag{A.5}$$

With the help of equation A.3 and this inverse matrix the measured distribution can be unfolded:

$$x^{\text{unf}} = \frac{1}{2\epsilon} \begin{pmatrix} 1+\epsilon & -1+\epsilon \\ -1+\epsilon & 1+\epsilon \end{pmatrix} \begin{pmatrix} x_1^{\text{meas}} \\ x_2^{\text{meas}} \end{pmatrix}. \tag{A.6}$$

Equation A.6 gives the exact solution. If ϵ is small and the uncertainties in x^{meas} are large, $|x_1^{\text{meas}} - x_2^{\text{meas}}| < \sqrt{(\Delta x_1^{\text{meas}})^2 + (\Delta x_2^{\text{meas}})^2}$, this solution becomes meaningless. To see this, the solution A.6 is rewritten as:

$$x^{\text{unf}} = \frac{x_1^{\text{meas}} - x_2^{\text{meas}}}{2\epsilon} \begin{pmatrix} 1 \\ -1 \end{pmatrix} + \frac{x_1^{\text{meas}} + x_2^{\text{meas}}}{2} \begin{pmatrix} 1 \\ 1 \end{pmatrix}. \tag{A.7}$$

If the uncertainties are too large, the first term becomes a random number. But if this term dominates, due to a small value for ϵ, one of the two unfolded values becomes negative. This behaviour is also observed if the matrix and distributions have more dimensions. The unfolded distribution starts oscillating, which means that for subsequent bins the values are alternatingly large positive or large negative numbers.

Several important features are illustrated by this two-dimensional example. First that the result depends on the uncertainties, for large uncertainties the first term in equation A.7 can become a random number, and so the total outcome. A second feature which was illustrated, is that the result can become unphysical if the binning is chosen too optimistically. If the events in the example are split into two bins that are indistinguishable for the detector (ϵ is small) then the result is dominated by the first term of equation A.7. If the measurement is not precise enough this first dominant term becomes unphysical,

and so does the final result. This is also true for more bins. If binning is chosen in such a way that the detector can not distinguish them, the result will become unphysical (will start oscillating).

To solve this problem of oscillating unfolded distributions, a procedure called "regularised unfolding" can be applied. Unfolding methods have been widely discussed in [58]. Two methods recently developed by A. Höcker and V. Kartvelishvili (SVD [59]) and by G.D'Agostini (BAYES [60]) are discussed in the next two paragraphs. These paragraphs paraphrase the two articles referenced.

A.2 Unfolding based on Singular Value Decomposition

In this method the folding matrix A is decomposed into two orthogonal matrices and a diagonal matrix. The elements of the diagonal matrix give information about the number of useful bins. With the help of these diagonal elements a demping procedure can be performed. This demping reduces the oscillatory behaviour of the unfolded distribution.

Definition

Singular value decomposition (SVD) of an $m \times n$ matrix A is a factorisation of the form:

$$A = USV^T. \tag{A.8}$$

Here, U is an $m \times m$ orthogonal matrix, V is an $n \times n$ orthogonal matrix and S is an $m \times n$ diagonal matrix with non-negative elements, $S_{ii} \equiv s_i \geq 0$. The quantities s_i are called singular values of A, and the columns of U and V are called the left and right singular vectors. The singular values are ranked in decreasing order ($s_j \leq s_i$ for $j > i$).

These singular values give some information about the matrix itself. If A is orthogonal all singular values are equal to one, but a degenerate matrix will have singular values which are equal to zero. If some singular values are significantly smaller than others, the matrix behaves like a degenerate matrix although it is not such a matrix.

Unfolding with SVD

Equation A.1 can be rewritten with the help of equation A.8. This gives:

$$x^{\text{meas}} = USV^T x^{\text{unf}}, \tag{A.9}$$

$$z \equiv V^T x^{\text{unf}}, \tag{A.10}$$

$$d \equiv U^T x^{\text{meas}}, \tag{A.11}$$

$$z = S^{-1} d. \tag{A.12}$$

When this is applied to the matrix A.4, as example, the singular decomposition gives:

$$U = V = \frac{1}{\sqrt{2}} \begin{pmatrix} 1 & 1 \\ 1 & -1 \end{pmatrix}, \qquad S = \begin{pmatrix} 1 & 0 \\ 0 & \epsilon \end{pmatrix}, \tag{A.13}$$

and the unfolded distribution is given by:

$$x^{\text{unf}} = Vz = VS^{-1}d = VS^{-1}U^T x^{\text{meas}} = A^{-1}x^{\text{meas}}. \tag{A.14}$$

This expression is the same as equation A.3 and SVD is thus just another way to calculate the inverse matrix of A.

Formally, SVD of the matrix A means a decomposition of x^{meas} into a series of orthogonal and normalised functions, the basis is given by the columns of U and d gives the coefficients of this decomposition. Similarly x^{unf} is also decomposed and the basis is now given by the columns of V, the vector z gives the unknown coefficients, which can be easily solved by equation A.12 (the inversion of S is done by simply inverting the singular values).

Redefining the problem

The problem of unfolding can be rewritten as a minimisation problem by:

$$\sum_i \left(\frac{\sum_j A_{ij} x_j^{\text{unf}} - x_i^{\text{meas}}}{\Delta x_i^{\text{meas}}} \right)^2 = \text{min}. \tag{A.15}$$

With the help of the covariance matrix of x^{meas}, X, this can be rewritten as:

$$(Ax^{\text{unf}} - x^{\text{meas}})^T X^{-1} (Ax^{\text{unf}} - x^{\text{meas}}) = \text{min}. \tag{A.16}$$

In order to compensate for the loss of information when A is calculated as a probability matrix, the folding matrix and the distribution to be unfolded are rescaled. This is done by equipping the matrix with the actual numbers of events generated, and at the same time dividing the distribution by the number generated in each bin. Thus:

$$A^*_{ij} = A_{ij} x_j^{\text{gen}}, \qquad w_j = x_j^{\text{unf}} / x_j^{\text{gen}}. \tag{A.17}$$

Because the MC sample is expected to predict the unfolded distribution quite well, the bin-to-bin fluctuations in w are expected to be small.

Rescaling of equations A.16 by dividing each equation by its corresponding uncertainty gives a balanced system where all equations have equal weights. SVD of the covariance matrix X gives:

$$X = QRQ^T, \qquad R_{ii} \equiv r_i^2. \tag{A.18}$$

The fact that X is a covariance matrix has been utilised here. Redefining A^* and x^{meas} gives:

$$\tilde{A}_{ij} = \frac{1}{r_i} \sum_m Q_{im} A^*_{mj}, \qquad \tilde{x}_i = \frac{1}{r_i} \sum_m Q_{im} x_m^{\text{meas}}. \tag{A.19}$$

Then finally the system of equations looks like:

$$(\tilde{A}w - \tilde{x})^T (\tilde{A}w - \tilde{x}) = \text{min}. \tag{A.20}$$

Regularisation

Equation A.20 still gives an exact solution and can have an oscillating behaviour. But now a regularisation or stabilisation term can be introduced:

$$(\tilde{A}w - \tilde{x})^T(\tilde{A}w - \tilde{x}) + \tau(Cw)^T Cw = \min. \tag{A.21}$$

Here, C is a matrix which defines an a-priori condition on the solution, and τ gives the weight of this condition. The value of τ is case dependent but the form for C can be taken from general considerations. As already mentioned, the unfolded distribution w is expected to be smooth with small bin-to-bin fluctuations. Minimisation of a curvature defined as:

$$\sum_i [(w_{i+1} - w_i) - (w_i - w_{i-1})]^2, \tag{A.22}$$

will suggest a choice for C:

$$C = \begin{pmatrix} -1+\epsilon & 1 & 0 & 0 & \cdots & \cdots \\ 1 & -2+\epsilon & 1 & 0 & \cdots & \cdots \\ 0 & 1 & -2+\epsilon & 1 & \cdots & \cdots \\ & \vdots & & & \vdots & \\ & \cdots & & 1 & -2+\epsilon & 1 \\ & \cdots & & 0 & 1 & -1+\epsilon \end{pmatrix}. \tag{A.23}$$

Here, ϵ is introduced so that the inverse of the matrix C exists, while for small ϵ the curvature calculation is hardly affected. A value of $10^{-3} - 10^{-4}$ is a good choice for most cases. Now solutions with a large curvature will be suppressed.

The linear system is given by:

$$\begin{pmatrix} \tilde{A} \\ \sqrt{\tau}C \end{pmatrix} w = \begin{pmatrix} \tilde{A}C^{-1} \\ \sqrt{\tau} \end{pmatrix} Cw = \begin{pmatrix} \tilde{x} \\ 0 \end{pmatrix}. \tag{A.24}$$

For $\tau = 0$ the solution is given by:

$$\tilde{A}C^{-1} = USV^T, \tag{A.25}$$

$$d \equiv U^T\tilde{x}, \qquad z \equiv V^T Cw, \qquad z_i = \frac{d_i}{s_i}. \tag{A.26}$$

This solution has still all problems concerning unfolding, thus small values for s_i will give large contributions to the unfolded data and can give wildly oscillating results. But the values for the unfolded distribution z_i can now be calculated for any value of τ. The introduction of a value for τ is effectively equivalent to changing d_i by a regularised distribution:

$$d_i^{(\tau)} = d_i \frac{s_i^2}{s_i^2 + \tau}, \tag{A.27}$$

$$z_i^{(\tau)} = d_i \frac{s_i}{s_i^2 + \tau}, \tag{A.28}$$

$$w^{(\tau)} = C^{-1} V z^{(\tau)}, \tag{A.29}$$

$$x^{\mathrm{unf}} = w^{(\tau)} x^{\mathrm{gen}}. \tag{A.30}$$

The last problem is to choose a value for τ. The values of d_i are the coefficients in the decomposition of the measured distribution. For smooth distributions only the first few terms (small values of i) of the decomposition are expected to be significant. The higher terms (large values of i), which have values comparable with zero (the uncertainty on all terms is one), give the contribution of quickly oscillating basis vectors. Thus terms which have $|d_i| < 1$ should be suppressed. If $|d_i| < 1$ for $i > k$ a good value for τ is given by:

$$\tau = s_k^2, \tag{A.31}$$

with the value for s taken from the singular value decomposition in equation A.25.

The covariance matrix can now be easily calculated. Recall that the uncertainty is one for all d_i. The covariance matrix X is calculated as follows:

$$Z_{ik}^{(\tau)} = \frac{s_i^2}{(s_i^2 + \tau)^2} \delta_{ik}, \tag{A.32}$$

$$W^{(\tau)} = C^{-1} V Z^{(\tau)} V^T C^{T^{-1}}, \tag{A.33}$$

$$X_{ik}^{(\tau)} = x_i^{\mathrm{gen}} W_{ik}^{(\tau)} x_k^{\mathrm{gen}}. \tag{A.34}$$

$$\tag{A.35}$$

A.3 Unfolding based on Bayes' Theorem

In this method Bayes' Theorem is utilised to unfold the measured distribution. This theorem uses the folding matrix but also the generated distribution for calculation of the total probability P_j^0 that the generated value lies in bin j:

$$P_j^0 = \frac{N_j}{\sum_{j=1}^{n_c} N_j}. \tag{A.36}$$

The unfolding procedure consists of an iterative calculation of number of unfolded events from which the total probability distribution is derived after each step. The new probability distribution is used in the following step. The regularisation is achieved by stopping the iteration befor the oscillatory behaviour becomes recognisable.

Bayes' Theorem

If n_c causes, binned into a distribution x^{gen}, and n_e effects, binned into a distribution x^{meas}, are considered, then Bayes' Theorem states:

$$S^0_{ji} = \frac{A_{ij} P^0_j}{\sum_{l=1}^{n_c} A_{il} P^0_l}. \tag{A.37}$$

Here, A_{ij} is the probability that cause j produces effect i (this is the same matrix A of the previous section) and P^0_j is the probability of cause j to occur. S^0_{ji} is the smearing matrix, the elements give the probability that effect i originates from cause j. The zero indicates that the MC input is used for the calculation of P^0 and S^0.

From equation A.37 it follows directly that:

$$\sum_{j=1}^{n_c} S^0_{ji} = 1. \tag{A.38}$$

This means that each effect seen must come from one of the causes considered. Also the initial probability for any cause to occur must be unity, or $\sum_{j=1}^{n_c} P^0_j = 1$. But for each cause there does not need to be an effect, or:

$$\epsilon_j \equiv \sum_{i=1}^{n_e} A_{ij}, \tag{A.39}$$

with $0 \leq \epsilon_j \leq 1$, ϵ_j is the efficiency of cause j to give an observed effect.

Unfolding

Unfolding of a measured distribution $\hat{n}^{\text{meas}}$ (the hat indicates that the distribution comes from the data and not the MC) can be performed with the Bayes' Theorem:

$$\hat{n}^{\text{unf}}_j = \frac{1}{\epsilon_j} \sum_{i=1}^{n_e} S^0_{ji} \hat{n}^{\text{meas}}_i. \tag{A.40}$$

The L3 Geneva "one-step" method [61] takes this distribution as the final result. It appears that there is no possibility to improve on this result. But the probabilities for the causes can now be derived from the data:

$$\hat{N}^{\text{unf}} = \sum_{j=1}^{n_c} \hat{n}^{\text{unf}}_j, \tag{A.41}$$

$$\hat{P}^{\text{unf}}_j = \frac{\hat{n}^{\text{unf}}_j}{\hat{N}^{\text{unf}}}. \tag{A.42}$$

Here, $\hat{N}^{\text{unf}}$ is the total number of unfolded events and $\hat{P}^{\text{unf}}_j$ the probability for cause j given by the data. If P^0 is not consistent with the data then P^0 and $\hat{P}^{\text{unf}}$ will not agree. From simulated data and examples one can verify that $\hat{P}^{\text{unf}}$ lies between the input distribution and the true distribution. This suggests an iterative procedure:

1. Start with an initial $\hat{n}^0$ and $\hat{P}^0$.
2. Calculate the smearing matrix from equation A.37.
3. Calculate $\hat{n}^{\text{unf}}$ and $\hat{P}^{\text{unf}}$ from equation A.40.
4. Compare $\hat{n}^0$ with $\hat{n}^{\text{unf}}$, if the differences are significantly large then replace $\hat{n}^0$ by $\hat{n}^{\text{unf}}$ and $\hat{P}^0$ by $\hat{P}^{\text{unf}}$ and go to 2, else stop the iteration.

Regularisation

If a large number of iterations is performed, the unfolded distribution starts oscillating again. The reason for this is that after an infinite number of iterations the unfolding matrix becomes in some sense the inverse matrix of the smearing matrix, with all the problems related to the inverse matrix. For this reason a regularisation is introduced.

One regularisation is to calculate the optimum number of iterations which depends on the problem involved. Another method is to smooth the result before feeding it in the next step as the initial probability $\hat{P}^0$. The best result for our sample was obtained with the first approach. So the iteration was stopped after the first few steps (when the changes were not significant). The second method still gave wildly oscillating results when the iterations were continued after they became insignificant.

Error calculation

For simplicity of the following equations in this section equation A.40 is rewritten:

$$n_i^{\text{unf}} = \sum_{j=1}^{n_e} M_{ij} n_j^{\text{meas}}. \tag{A.43}$$

with $M_{ij} = \frac{1}{\epsilon_i} S_{ij}$. The smearing matrix is calculated with the probabilities from the data (that is why there is no zero).

For the calculation of the covariance matrix two contributions are considered. The first comes from the uncertainties of the measured distribution, n_j^{meas} and the second from the MC statistics used for the calculation of the matrix M_{ij}. First the contribution from the measured distribution is calculated:

$$V_{kl}^0 = \sum_{i,j=1}^{n_e} \frac{\delta n_k^{\text{unf}}}{\delta n_i^{\text{meas}}} \frac{\delta n_l^{\text{unf}}}{\delta n_j^{\text{meas}}} Cov\{n_i^{\text{meas}}, n_j^{\text{meas}}\}, \tag{A.44}$$

$$\frac{\delta n_k^{\text{unf}}}{\delta n_i^{\text{meas}}} = M_{ki}, \tag{A.45}$$

$$Cov\{n_i^{\text{meas}}, n_j^{\text{meas}}\} = \begin{cases} n_i^{\text{meas}} \delta_{ij} & \text{(Poisson)}, \\ n_i^{\text{meas}} (1 - \frac{n_i^{\text{meas}}}{\hat{N}^{unf}}) \delta_{ij} - \frac{n_i^{\text{meas}} n_j^{\text{meas}}}{\hat{N}^{unf}} (1 - \delta_{ij}) & \text{(multi)}. \end{cases} \tag{A.46}$$

Here, equation A.46 (Poisson) is valid for Poisson distributions and equation A.46 (multi) for multinominal distributions.

For low efficiencies the bins become independent measurements and the Poisson distributions are good approximations for the measurements. For higher efficiencies the measurements are described by multinominal distributions.

Now the calculation is performed for the contribution from the matrix:

$$V^1_{kl} = \sum_{i,m=1}^{n_c} \sum_{j,n=1}^{n_e} \frac{\delta n_k^{\text{unf}}}{\delta M_{ij}} \frac{\delta n_l^{\text{unf}}}{\delta M_{mn}} Cov\{M_{ij}, M_{mn}\}, \tag{A.47}$$

$$\frac{\delta n_k^{\text{unf}}}{\delta M_{ij}} = n_j^{\text{meas}} \delta_{ik}, \tag{A.48}$$

$$Cov\{M_{ij}, M_{mn}\} = \sum_{r,t=1}^{n_e} \sum_{s,u=1}^{n_c} \frac{\delta M_{ij}}{\delta A_{rs}} \frac{\delta M_{mn}}{\delta A_{tu}} Cov\{A_{rs}, A_{tu}\}, \tag{A.49}$$

$$\frac{\delta M_{ij}}{\delta A_{rs}} = M_{ij} \left[\frac{\delta_{is}\delta_{jr}}{A_{rs}} - \frac{\delta_{is}}{\epsilon_s} - \frac{\delta_{jr} M_{sj} \epsilon_s}{A_{js}} \right], \tag{A.50}$$

$$Cov\{A_{rs}, A_{tu}\} = \begin{cases} \frac{1}{N_s} A_{rs} \delta_{rt} \delta_{su} & \text{(Poisson)}, \\ \frac{\delta_{su}}{N_s} [A_{rs}(1 - A_{rs})\delta_{rt} - A_{rs} A_{tu}(1 - \delta_{rt})] & \text{(multi)}. \end{cases} \tag{A.51}$$

Here, equation A.51 (Poisson) is valid for Poisson distributions and equation A.51 (multi) for multinominal distributions, N_s is the total number of events generated in bin s. For the Poisson assumption only the uncertainty in N_{rs} is taken into account (low efficiency thus $N_{rs} << N_s$). For the multinominal distribution no covariance between generated bins was assumed. The total covariance matrix is the sum of V^0 and V^1.

A.4 Checking the methods

Before the methods are applied to unfold the data, they are checked with the help of the example matrix A.4.

First the influence of τ on the result obtained from the SVD method is shown. The final regularised result is given as:

$$x^{\text{unf}} = \frac{\epsilon(x_1^{\text{meas}} - x_2^{\text{meas}})}{2(\epsilon^2 + \tau)} \begin{pmatrix} 1 \\ -1 \end{pmatrix} + \frac{x_1^{\text{meas}} + x_2^{\text{meas}}}{2(1 + \tau)} \begin{pmatrix} 1 \\ 1 \end{pmatrix}. \tag{A.52}$$

If $\tau = 0$ this is again the exact result. For small values of ϵ regularisation is needed. For regularisation, $\epsilon^2 << \tau << 1$, the influence of the first term is reduced with a factor τ/ϵ^2 while the second term is unchanged. For the worst case scenario, $\epsilon = 0$ no exact result exists. The first term of the regularised result vanishes and only the second term (flat distribution) remains. Thus a direct connection exists between the result and the value chosen for τ.

The BAYES method allows no direct analytical calculation of the final result. However, the result after the first step can be calculated (thus checking the L3 Geneva "one-step"

method). The smearing matrix A.37 can be calculated with matrix A.4. The efficiencies, given by equation A.39 for the two bins, are both one. The initial probabilitie distribution is given by $P_0 = \begin{pmatrix} x_1^{\text{gen}} \\ x_2^{\text{gen}} \end{pmatrix}$ with $x_1^{\text{gen}} + x_2^{\text{gen}} = 1$. The unfolded one-step result is given by A.40:

$$x^{\text{unf}} = \begin{pmatrix} \frac{(1+\epsilon)x_1^{\text{gen}}}{(1+\epsilon)x_1^{\text{gen}}+(1-\epsilon)x_2^{\text{gen}}} x_1^{\text{meas}} + \frac{(1-\epsilon)x_1^{\text{gen}}}{1-\epsilon)x_1^{\text{gen}}+(1+\epsilon)x_2^{\text{gen}}} x_2^{\text{meas}} \\ \frac{(1-\epsilon)x_2^{\text{gen}}}{(1+\epsilon)x_1^{\text{gen}}+(1-\epsilon)x_2^{\text{gen}}} x_1^{\text{meas}} + \frac{(1+\epsilon)x_2^{\text{gen}}}{1-\epsilon)x_1^{\text{gen}}+(1+\epsilon)x_2^{\text{gen}}} x_2^{\text{meas}} \end{pmatrix} \tag{A.53}$$

For results which need no regularisation, $\epsilon = 1$, this result can be rewritten and gives:

$$x^{\text{unf}} = \begin{pmatrix} x_1^{\text{meas}} \\ x_2^{\text{meas}} \end{pmatrix} \tag{A.54}$$

This means that when no unfolding is needed the BAYES method gives the expected result. In the worst case scenario $\epsilon = 0$ the result can be rewritten as:

$$x^{\text{unf}} = (x_1^{\text{meas}} + x_2^{\text{meas}}) \begin{pmatrix} x_1^{\text{gen}} \\ x_2^{\text{gen}} \end{pmatrix} \tag{A.55}$$

Now the result is nothing more than the generated input scaled with the measurement. This result thus simulates a perfect description of the data by the MC sample (the MC distribution is equal to the unfolded distribution). But in reality the detector is not capable of distinguishing the two bins and no matter which model is applied, the unfolded distribution will always resemble the MC input distribution. This creates the misleading impression that the model is correct and that the sample is thus understood! The smaller ϵ the more the unfolded distribution after one step resembles the MC sample and the larger the possibility that BAYES stops after one step.

A.5 Comparison of the two procedures

The two procedures can be compared with each other to see the influence of the unfolding on the cross section. In this section the untagged data, taken around the Z pole is emploied. In figure A.1 the results after unfolding are shown for the data with four bins. The SVD results are obtained with $\tau = s_1^2$. Comparisson of the unfolded distribution with the generated distribution yields that they are identical (in shape, not in the overall normalisation). This means that the model is scaled to give the SVD results. For comparison the theoretical predictions made by the two models are shown as well.

The BAYES results are obtained with equation A.40. So no iteration is performed. This is the unfolding technique epplied by the L3 Geneva group. It appears that these results resemble the model closely and that only the overall scale can be obtained from this one-step technique but not the shape!

To compare the results after the unfolding as applied in this thesis, the data is unfolded with the SVD method with $\tau = s_4^2$. Still some regularisation was needed for the influence of the fourth bin. The BAYES result is obtained after the iteration had stopped. The

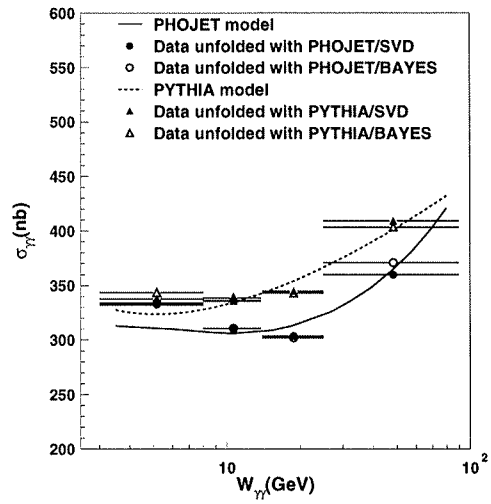

Figure A.1: *The cross section calculated with the unfolded distributions. The uncertainties are the square roots of the diagonal elements of the covariance matrix. The SVD results are obtained with* $\tau = s_1^2$ *and the BAYES results are obtained directly from A.40 without any iteration.*

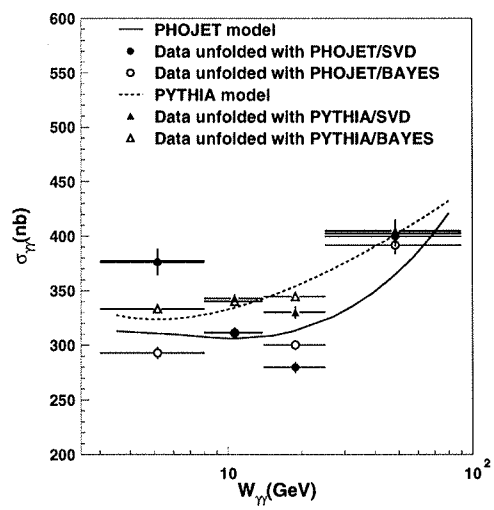

Figure A.2: *The cross section calculated with the unfolded distributions. The uncertainties the square roots of the diagonal elements of the covariance matrix. The SVD results are obtained with* $\tau = s_4^2$ *and the BAYES results are obtained after the iteration stopped.*

influence of the model applied to unfold is still large. The two unfolding techniques give results which are fairly similar except for the lowest mass bin (see figure A.2).

Due to the fact that each event measured must be assigned to a true mass bin, correlations between the different true mass bins can not be avoided. In table A.1 these correlations are given for the two different models. The correlations are substantial and have to be taken into account when fits are performed to the results. The correlation is the largest for the BAYES method.

1.00			
0.62	1.00		
-0,79	-0.13	1.00	
0.15	-0.44	-0.26	1.00

1.00			
0.95	1.00		
0.59	0.79	1.00	
0.22	0.37	0.70	1.00

Table A.1: *The correlation matrix for the unfolding procedure with SVD (left) and BAYES method (right).*

A check of the influence of the regularisation of the method can be obtained by multiplying the unfolding matrix with the regularised inverse matrix:

$$AA^{-1} \stackrel{?}{=} I. \tag{A.56}$$

For the BAYES method the inverse matrix is given by the smearing matrix S. For the SVD method the regularised inverse matrix is:

$$A^{-1}_{ij} = \sum_{kl} C^{-1}_{ik} V_{kl} \frac{s_l}{s_l^2 + \tau} U^{\mathrm{T}}_{lj} \frac{1}{\Delta x_j^{\mathrm{meas}}}.$$

The closer the regularised inverse matrix is to the true inverse matrix, the closer the result of this multiplication is to the unit matrix. In table A.2 the two results are given. The SVD method gives a result close to the unit matrix. The result of the BAYES method is not diagonal but has large off-diagonal elements. This states that this method is not really a calculation of the inverse matrix but more a reverse folding method.

0.99	0.02	-0.04	0.05
0.02	0.94	0.12	-0.13
-0.03	0.10	0.80	0.23
0.03	-0.10	0.20	0.76

0.54	0.34	0.10	0.02
0.38	0.40	0.18	0.05
0.25	0.39	0.26	0.10
0.18	0.33	0.33	0.15

Table A.2: *The folding matrix times the regularised inverse matrix, left the outcome for the SVD method and right for the BAYES method.*

Another check is to multiply the regularised inverse matrix with the unfolding matrix:

$$A^{-1}A \stackrel{?}{=} I. \tag{A.57}$$

The results diminish with respect to the previous check. The SVD method still gives a matrix with the largest elements on the diagonal but the off-diagonal elements are large compared to the previous result. Also the result for the BAYES method has worsened, and the result does not in any way resemble an unit matrix.

0.78	0.46	-0.33	0.09
0.10	0.79	0.15	-0.04
-0.04	0.09	0.93	0.02
0.02	-0.03	0.03	0.99

0.16	1.48	1.61	0.73
0.04	0.42	0.60	0.34
0.01	0.19	0.42	0.35
0.00	0.06	0.20	0.35

Table A.3: *The regularised inverse matrix times the unfolding matrix, left for the SVD method and right for the BAYES method.*

From these two checks it appears that both methods try to derive a regularised inverse matrix that minimises the changes to the measurement ($AA^{-1}x^{\text{meas}} \approx x^{\text{meas}}$) but do change the model ($A^{-1}Ax^{\text{gen}} \not\approx x^{\text{gen}}$).

The SVD method gives, in the form of the values of s_i, a clear indication of the number of independent bins that are in the sample. If instead of four bins ten bins are taken, the SVD output gives four values for s_i which are larger than one, and thus six values that are lower. This is the reason why four bins have been applied in this thesis, although more indications existed that four bins was the maximum. In order to check what happens if too many bins are taken, the data has also been analysed with ten bins. The results are shown in figures A.3 (SVD with $\tau = s_1^2$ and no iteration for BAYES) and A.4 (SVD with $\tau = s_4^2$ and BAYES result after iterations).

It now seems that more information is in the result with the ten bins than in the results with four bins. To check this, the results obtained with PYTHIA/SVD are compared with each other, see figure A.5. From this plot it appears that the result obtained with 4 bins shows the average of the results obtained with 10 bins. The dip in the middle is more pronounced in the 10-bin result than in the four-bin result. This appears to be the start of the oscillations which were supposed to be suppressed when these technicques are applied. If the regularisation of the ten bins is reduced ($\tau = s_4^2$ is replaced by $\tau = s_5^2$) the oscillatory behaviour of the result becomes more obvious. The ten bins are thus essentially four independent bins and six dependent bins which on average give the same result as obtained with four bins. The correlation between the bins is large accordingly.

A.6 Conclusions

Both methods applied to unfold the data must be treated carefully. To use them as black boxes is discouraged and careful consideration of the methods and results is needed. Too large a regularisation (SVD with a too large value for τ or BAYES with too few steps) leads to results which are more connected with the MC samples than with the data. This can result in too optimistic conclusions concerning the validity of the MC samples or the detector performance.

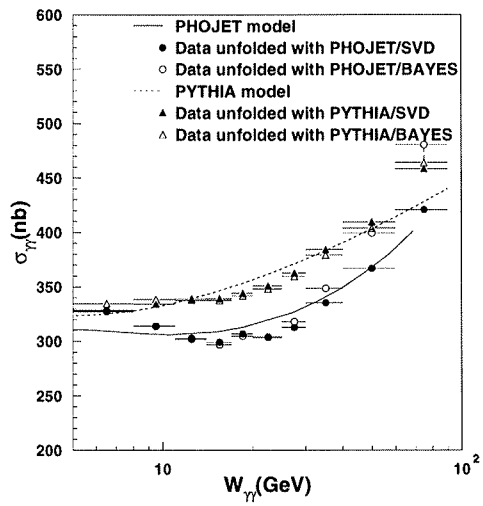

Figure A.3: *The cross section calculated with the unfolded distributions. The uncertainties are the square roots of the diagonal elements of the covariance matrix. The SVD results are obtained with* $\tau = s_1^2$ *and the BAYES results are obtained directly from A.40 without any iteration.*

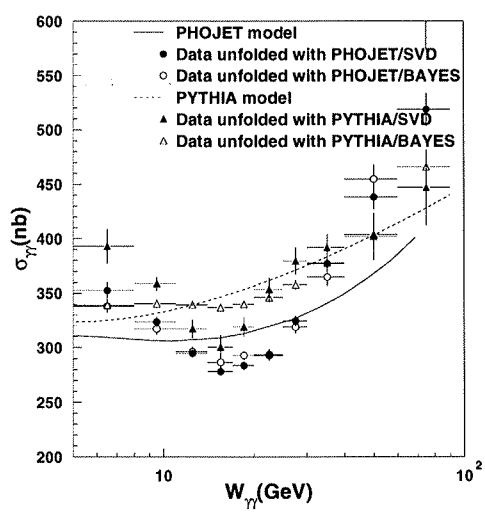

Figure A.4: *The cross section calculated with the unfolded distributions. The uncertainties are the square roots of the diagonal elements of the covariance matrix. The SVD results are obtained with* $\tau = s_4^2$ *and the BAYES results are obtained after the iteration stopped.*

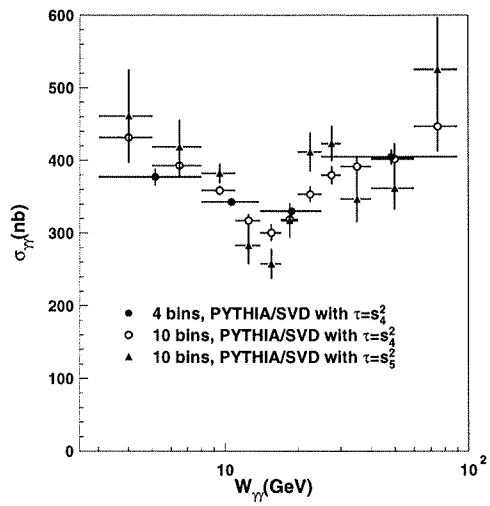

Figure A.5: *The cross section calculated with the unfolded distributions. The uncertainties are the square roots of the diagonal elements of the covariance matrix.*

Also the number of bins must be chosen with care. If too many bins are choosen, it will be impossible to distinguish them. Some of the bins will be interpolations of the other bins. The SVD technique gives information about the number of independent bins in the form of the singular values. For the BAYES method the choice must be based on the resolution or by trial and error methods.

Appendix B

Modifications of the PYTHIA generator

In the PYTHIA generator only the interaction between two real photons is implemented. In order to generate a two-photon sample which is produced by the incoming electron and positron the luminosity function had to be implemented. For the tagged sample a description for virtual photons had to be implementd as well.

B.1 Luminosity function

The luminosity function is taken from the TWOGEN generator [63]. In this generator the transverse-transverse luminosity function is sampled as follows:

$$\frac{d^6\mathcal{L}_{\gamma\gamma}^{TT}}{dw_1 dw_2 d\theta_1 d\theta_2 d\phi_1 d\phi_2} = \frac{1}{w_1 w_2} \cot\frac{1}{2}\theta_1 \cot\frac{1}{2}\theta_2 f_w. \tag{B.1}$$

Here, w_i is the energy of the photon, θ_i the scattering angle of the electron or positron, ϕ_1 the azimuthal angle between the scattering planes and ϕ_2 the azimuthal angle for the electron or positron. The weight function f_w is defined as:

$$f_w = w_1 w_2 \frac{\alpha^2}{2\pi^4} \frac{E_1' E_2'}{E^2} \frac{\sin^2\frac{1}{2}\theta_1 \sin^2\frac{1}{2}\theta_2}{q_1^2 q_2^2} \sqrt{X} \rho_1^{++} \rho_1^{++}. \tag{B.2}$$

By doing so, the luminosity function is factorised into a part which can be integrated analytically and therefore generated exactly, and a weight function f_w. The distributions are thus generated as $1/w_i$ for the photon energies and as $\cot\frac{1}{2}\theta_i$ for the scattering angles. The two ϕ's are generated over a flat distribution from 0 to 2π. The total weight F_w, which is given to each event after all 6 variables are generated is given by:

$$F_w = (2\pi)^2 \left[2\log\left(\frac{\sin\frac{1}{2}\theta_{\max}}{\sin\frac{1}{2}\theta_{\min}}\right)\right]^2 \left[\log\left(\frac{w_{\max}}{w_{\min}}\right)\right]^2 w_1 w_2 \tan\frac{1}{2}\theta_1 \tan\frac{1}{2}\theta_2 f_w. \tag{B.3}$$

Here, $(2\pi)^2$ is the volume element for the integrating over both ϕ's, $\left[2\log\left(\frac{\sin\frac{1}{2}\theta_{\max}}{\sin\frac{1}{2}\theta_{\min}}\right)\right]^2$ the integrating over both $\cot\frac{1}{2}\theta$ and $\left[\log\left(\frac{w_{\max}}{w_{\min}}\right)\right]^2$ integration over both w's. The luminosity function is given $w_1 w_2 \tan\frac{1}{2}\theta_1 \tan\frac{1}{2}\theta_2 f_w$. The total weight F_w is transported to the PYTHIA main programme and is taken into account in the total cross-section calculation and in the hit/miss method for sampling the events.

B.2 Q^2 dependence

As no Q^2 dependence is included in the PYTHIA two-photon cross sections, the number of tagged events is overestimated. Only for the direct part this dependence is known. For the VDM part two different models exist. For the other four different contributions this dependence is not known and has to be taken from the measurements.

Because the Q^2 dependence is known for two contributions, it is logical to include these dependences in PYTHIA. Thus the two-photon cross section as calculated by PYTHIA is multiplied with a factor which includes this dependence.

The direct contribution is multiplied with:

$$F(Q^2) = \frac{1}{(1+\frac{Q^2}{W^2_{\gamma\gamma}})^2}. \tag{B.4}$$

For the VDM contribution a choice between two different form factors can be made with which the cross section has to be multiplied. An extra variable is included in PYTHIA to choose between these two options, the GVDM factor (1.24) and the TPC/2γ VDM factor as explained in section 1.4.1.

To check these form factors, PYTHIA is compared with other generators. The Feynman diagrams for the direct contribution are known. So the factor for this contribution can be checked with a generator which is based on these diagrams, DIAG36 [62]. For the comparison the production of a $d\bar{d}$ quark pair was taken, with a minimum two-photon mass of 2 GeV. The level of agreement between these two generators improved when the form factor was introduced in PYTHIA. In table B.1 the cross sections are given. Also all event variables were described better with the inclusion of the from factor. In figure B.1 the mass of the photon, Q^2, emitted by the electron is plotted. In the left plot, no form factor is included. In the right plot the factor is included and now a nice agreement between PYTHIA and DIAG36 is obtained.

	DIAG36	PYTHIA	PYTHIA+form factor	TWOGEN
direct (pb)	110.7±0.3	126.6±0.1	112.2±0.2	
VMD (nb)		9.6±0.1	5.85±0.04	5.8±0.1

Table B.1: *The total cross section for the different generators.*

For the VMD contribution PYTHIA was compared with TWOGEN. TWOGEN also applies a factorisation of the total cross section into a two-photon luminosity part and

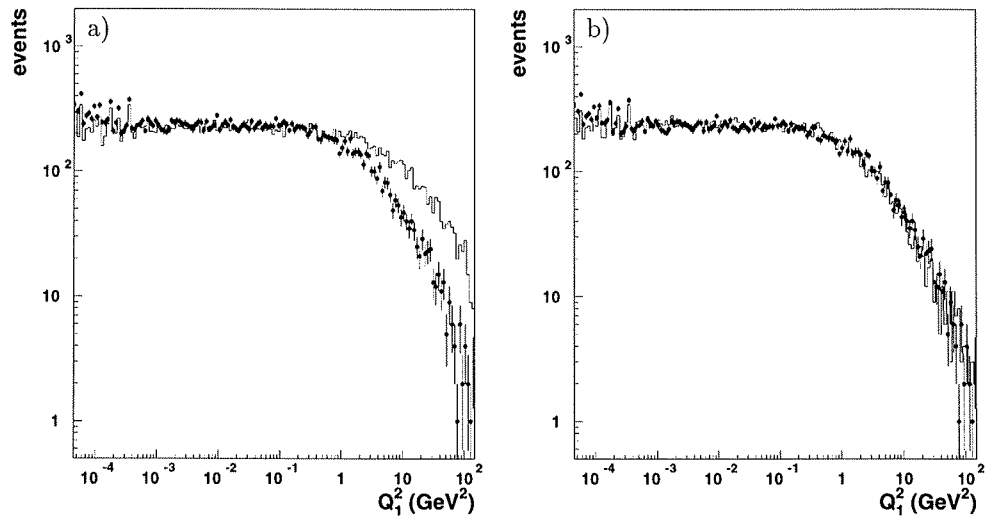

Figure B.1: *The mass of the photon emitted by the electron in the direct contribution: (a) no form factor is included in PYTHIA, and (b) with the factor implemented. In both plots the points come from DIAG36, and the lines come from PYTHIA.*

a two-photon cross section. The two-photon cross section for the VMD contribution is again factorised into a mass dependent part and a Q^2 dependent part. The mass dependent part of TWOGEN was changed so that the dependence was the same as in PYTHIA. In table B.1 the cross section is given for the VMD contribution with a minimum mass of 3 GeV. The cross section for TWOGEN was calculated with the GVDM form factor included. In figure B.2 again the mass of the photon emitted by the electron is plotted and both generators are compared. In the left plot the Q^2 dependence is removed from TWOGEN. And in the right plot the GVDM form factors are implemented both in PYTHIA and TWOGEN.

From the large difference between the left and right plot in figure B.2 it is clear that omission of the form factor gives a large overestimate of the total cross section and of the number of tagged events ($Q^2 > 1$ GeV^2). Because other experiments have measured that a form factor has to be included to describe the tagged data, it is better to start with the model which is closest to the data, a model which has the form factors implemented.

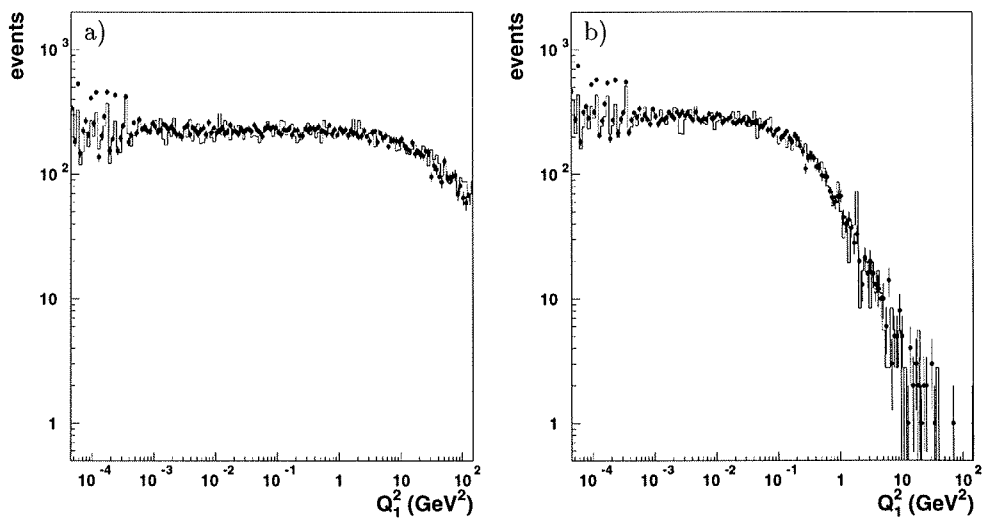

Figure B.2: *The mass of the photon emitted by the electron for the VDM contribution: (a) no form factor is included in PYTHIA and TWOGEN and (b) with the GVDM factor implemented. In both plots the points come from TWOGEN, and the lines come from PYTHIA.*

References

[1] D. Griffiths, Introduction to elementary particles, John Wiley and Sons, 1987.

[2] V.M. Budnev, I.F. Ginzburg, G.V. Meledin and V.G. Serbo, The two-photon particle production mechanism. Physical Problems. Applications. Equivalent photon approximation, Phys. Rep. **15** (1975) 181.

[3] H. Kolanoski, Two-Photon Physics at e^+e^- Storage Rings, Springer-Verlag 1984.

[4] J.L. Rosner, Brookhaven report CRISP 71 26 (1971).

[5] P.D.B. Collins, An introduction to Regge theory & high energy physics, Cambridge University Press 1977.

[6] E. Gotsman, A. Levy and U. Maor, A comprehensive description of the photon structure function and photon-photon total cross section data, Z. Phys. **C 40** (1988) 117.

[7] G.Alexander, U. Maor and C. Milstene, Estimates of the photon structure function derived from factorization, Phys. Lett. **131 B** (1983) 224.

[8] A. Levy, Estimate of the pointlike contribution $\sigma_T(\gamma\gamma)$, Phys. Lett. **B 181** (1986) 401.

[9] I.F. Ginzburg and V.G. Serbo, Some comments on the total $\gamma\gamma \to$ Hadron cross section at high energies, Phys. Lett. **109 B** (1982) 231.

[10] U. Maor and E. Gotsman, $\gamma\gamma$ scattering and extended vector dominance, Phys. Rev. **D 28** (1983) 2149.

[11] A. Donnachie and P.V. Landshoff, Total cross sections, Phys. Lett. **B 296** (1992) 227.

[12] G.A. Schuler and T. Sjöstrand, $\gamma\gamma$ and γp Events at High Energies. CERN-TH/7193/94, 1994.

[13] G.A. Schuler and T. Sjöstrand, A scenario for high-energy $\gamma\gamma$ interactions, Z. Phys. **C 73** (1997) 677.

[14] J. J. Sakurai and D. Schildknecht, Generalized vector dominance and inelastic electron-proton scattering, Phys. Lett. **40 B** (1972) 121.

[15] S. Brodsky, T. Kinoshita and H. Terazawa, Two-Photon Mechanism of Particle Production by High-Energy Colliding Beams, Phys. Rev. **D 4** (1971) 1532.

[16] G. Altarelli and G. Parisi, Asymptotic freedom in parton language, Nucl.Phys. **B 126** (1977) 298.

[17] E. Witten, Anomalous cross section for photon-photon scattering in gauge theories, Nucl. Phys. **B 120** (1977) 189.

[18] D. W. Duke and J. F. Owens, Quantum-chromodynamic corrections to deep-inelastic Compton scattering, Phys. Rev. **D 26** (1982) 1600.

[19] H. Abramowicz, K. Charchula and A. Levy, Parametrization of parton distributions in the photon, Phys. Lett. **B 269** (1991) 458.

[20] H. Abramowicz, K. Charchula, M. Krawczyk, A. Levy and U. Maor, Parton distributions in the photon, Int. J. of Mod. Physics **A 8** (1993) 1005.

[21] M. Drees and K. Grassie, Parametrizations of the Photon Structure and Applications to Supersymmetric Particle Production at HERA, Z. Phys. **C 28** (1985) 451.

[22] M. Glück, E. Reya and A. Vogt, Photonic parton distributions, Phys. Rev. **D 46** (1992) 1973.

[23] G.A. Schuler and T. Sjöstrand, Low- and high-mass components of the photon distribution functions, Z.Phys. **C 68** (1995) 607.

[24] G.A. Schuler and T. Sjöstrand, Parton Distributions of the Virtual Photon, Phys.Lett. **B 376** (1996) 193.

[25] A. Capella, et. al., Dual Parton Model, Phys. Rep. 236 (1994) 227.

[26] R. Engel, Hadronic photon-photon interactions at high energies, Phys. Rev. **D 54** (1996) 4244.

[27] R. Engel, Photoproduction within the two component dual parton model. 1. Amplitudes and cross-sections, Z. Phys. **C 66** (1995) 203.

[28] A.Capella, et. al., Hadron-nucleus interactions and the leading particle effect in a dual parton model, Z. Phys. **C 10** (1981) 249.

[29] T. Sjöstrand, High-energy physics event generation with PYTHIA 5.7 and JETSET 7.4, Computer Physics Communications **82** (1994) 74.

[30] T.H. Bauer et.al., The hadronic properties of the photon in high-energy interactions, Rev. Mod. Phys. **50** (1978) 261.

[31] G.A. Schuler and T. Sjöstrand, Towards a complete description of high-energy photoproduction, Nucl. Phys. **B 407** (1993) 539.

[32] G.A. Schuler and T. Sjöstrand, Hadronic diffractive cross sections and the rise of the total cross section, Phys. Rev. **D 49** (1994) 2257.

[33] D. Bintinger *et. al.*, Measurement of the Total Hadronic Cross Section in Virtual Photon-Photon Interactions, Phys. Rev. Lett. **54** (1985) 763.

[34] S.E. Baru *et. al.*, Total cross section of two-photon production of hadrons, Z. Phys. **C 53** (1992) 219.

[35] PLUTO Collaboration, A Measurement of the Q^2 and W Dependence of the $\gamma\gamma$ Total Cross Section for Hadron Production, Z. Phys. **C 26** (1984) 353.

[36] PLUTO Collaboration, Measurement of the total photon-photon cross section for the production of hadrons at small Q^2, Phys. Lett. **149B** (1984) 421.

[37] TPC/Two-Gamma Collaboration, Measurement of the total hadronic cross section in tagged $\gamma\gamma$ reactions, Phys. Rev. **D 41** (1990) 2667.

[38] M. Feindt, Recent PLUTO Results On Photon Photon Reactions, VIIth International Workshop on Photon-Photon Collisions, 388, 1986.

[39] CELLO Collaboration, Studies of multihadronic final states in photon-photon interactions, Z. Phys. **C 51** (1991) 365.

[40] L3 Collaboration, The Construction of the L3 Experiment, Nucl. Instr. and Meth. **A 289** (1989) 35.

[41] L3 SMD Collaboration (M. Acciarri, et al.), The L3 silicon microvertex detector, Nucl. Instrum. Methods **A 360** (1995) 103.

[42] E. Koffeman, Ph. D. thesis, University of Nijmegen, 1996.

[43] L3 F/B Muon Group (A. Adam, et al.), The forward muon detector of L3, Nucl. Instrum. and Methods **A 383** (1996) 342.

[44] J. Wenninger, Mesure de paramètres électro-faibles du Z avec la réaction $e^+e^- \rightarrow e^+e^-(\gamma)$, Ph. D. Thesis, University of Geneva (1992).

[45] Yu. Galaktionov et. al.,The performance of a uranium gas sampling calorimeter, Nucl. Instr. and Meth. **A251** (1986) 258.

[46] R. Brun et.al., GEANT 3, CERN DD/EE/84-1 (Revised), September 1987.

[47] H. Fesefeldt, The GHEISHA program, RWTH Aachen Report PITHA 85/02 (1985).

[48] F. Filthaut, Hadronic Cross Section Measurements on the Z Resonance with the L3 Detector, Ph. D. thesis, Univ. of Nijmegen 1993.

[49] H. Kuijten, Measurement of Hadronic Cross Sections and Asymmetries on the Z-Resonance, Ph. D. thesis, Univ. of Nijmegen 1996.

[50] X. Leijtens, Production of tau pairs at the Z resonance. Ph. D. thesis, Univ. of Amsterdam 1993.

[51] M.P. IJzerman, Study of Neutral Current Coupling Constants from Tau Pair Production, Ph. D. thesis, Univ. of Nijmegen 1996.

[52] The L3 Collaboration, Production of e, μ and τ Pairs in untagged Two-Photon Collisions at LEP, Phys. Lett. **B 407** (1997) 341.

[53] G.A. Schuler, Improving the equivalent-photon approximation in electron-positron collisions, CERN-TH/96-297,1996.

[54] H1 Collaboration, Scale Influence on the Energy Dependence of Photon-Proton cross sections, Phys.Lett. **B 392** (1997) 234.

[55] H1 Collaboration, A Measurement and QCD Analysis of the Proton Structure Function $F_2(x, Q^2)$ at HERA, Nucl. Phys. **B 470** (1996) 3.

[56] ZEUS Collaboration, Measurement of the Proton Structure Function F_2 at low x and low Q^2 at HERA, Z. Phys. **C 69** (1996) 607.

[57] G.A. Schuler and T. Sjöstrand, The hadronic properties of the photon in γp interactions, Phys. Lett. **B 300** (1993) 169.

[58] V. Blobel, Unfolding methods in high energy physics experiments, 1984 CERN school of Computing, CERN **85-09** (1985).

[59] A. Höcker and V. Karvelishvili, SVD Approach to Data Unolding, Nucl.Instrum. and Meth. **A 372** (1996) 469.

[60] G. D'Agostini, A Multidimensional Unfolding Method Based on Bayes' Theorem, Nucl. Instr. and Meth. **A 362** (1995) 487.

[61] L3 Collab. (M. Acciarri *et al.*), Cross section of hadron production in gamma gamma collisions at LEP, Phys. Lett. **B 408** (1997) 450.

[62] F. Berends, P. Daverveldt and R. Kleiss, Complete lowest order calculations for four lepton final states in electron-positron collisions, Nucl. Phys. **B 186** (1985) 441.

[63] A. Buijs, W.G.J. Langeveld, M.H. Lehto and D.J. Miller, TWOGEN, a Simple Monte Carlo Generator for Two-Photon Reactions, Comp. Phys. **79** (1994) 523.

Summary

In Quantum Electro-Dynamics the photon is the mediator of the electromagnetic field. In this theory the photon couples to charged particles. When a photon couples to a vector meson or a quark-antiquark pair it can interact with another photon. This is called a photon-photon interaction and is not predicted in classical electrodynamics.

Inside the LEP accelerator the two interacting photons are produced by two high-energetic particles, the electron and positron. The interactions are investigated with the L3 detector, one of the four large experiments at LEP. The production of the photons by these particles is described by QED. The process studied here is thus a two step process. First the two photons are produced, then these two photons interact. The first part can be calculated while the investigation of the second part is the subject of this thesis.

When the two photons couple directly to each other by exchanging a quark, and the transverse energy of the quarks is high enough, the process can be calculated using QED and is known as the direct or Quark-Parton Model contribution. Higher order diagrams give rise to the anomalous processes in which a constituent of the photon (either a quark, antiquark or a gluon) couples directly to the other photon or with a constituent of the other photon. These higher order diagrams can be calculated using particle density functions which describe the momentum distributions of the constituents in the photon, Quantum Chromo Dynamics which describes the interaction between two constituents (quark-quark and quark-gluon interactions) and QED which describes the interation between a quark and a photon.

When both photons couple to a vector meson, the two vector mesons can interact opening the whole range of (soft) hadon-hadron physics in photon-photon interactions. This is known as the Vector-meson Dominance Model contribution. These interactions have low energy transfers. The processes involved are elastic scattering, single and double diffractive and non-diffractive processes. They can not be calculated using field theory due to the fact that the results with higher order diagrams do not converge and QCD then does not give a good description. The Regge model is used to describe these kinds of soft processes. This model describes the behaviour of the cross section for hadron-hadron interactions and can also be applied for soft photon-photon interactions.

The two Monte-Carlo generators which were used have both the full range of interactions included, although this was only done for real photons. These generators were PYTHIA and PHOJET. Both generators predict that the two-photon cross section increases with increasing two-photon masses above 20 GeV. The tagged cross section was obtained from the real photon-photon cross section by multiplying this cross section with

the GVDM form factor. If the photon interacts mainly like a hadron then the cross section as function of the two-photon mass is expected to rise more steeply for higher values of the virtuality of the photon.

The measurement of the total cross section was done for energies around the Z pole (around 91 GeV) and around 133 GeV. The selected events had no final-state electron or positron inside the detector, socalled untagged events. The two-photon mass had to be reconstructed from the hadronic activity in the detector. The reconstructed mass distribution was distorted due to particles which were not inside the detector or were not used. In order to obtain the true mass distribution which is needed if the cross section is to be measured, the reconstructed visible mass distribution was unfolded with the use of two different programmes. These unfolding programmes use the MC input to relate the visible mass distribution to the true mass distribution.

The results for the cross section were compared with previous results. This showed that the results from this thesis agree with those of the previous experiments. The highest mass bin is in a region of the two-photon mass which has not been measured before. The cross section showed no distinctive rise above 20 GeV. Due to the large error bars (coming mainly from the differences between the different years and the differences between the two models used) it is not clear if the cross section remains flat or if it rises with increasing mass.

The tagged cross section was measured as well. Here, the final state electron or positron was measured in the luminosity monitor and the virtuality of one the two photons was measured. Because either the electron or positron was measured the mass of the two-photon system needed to be reconstructed again from the final state particles from the hadron system. This gave again a distorted mass distribution and unfolding was needed.

The cross sections obtained did not show a rise which increases for more virtual photons. The cross section as function of the mass for the three vituality bins could be described by a flat distribution.

The cross section as function of the virtuality showed a behaviour in all four mass bins which was best described by a sum of the direct contribution and a part scaled with the GVDM form factors. Other models like omitting the direct part or using only the ρ pole gave fits which were much worse.